Angular analysis of the $B^0 \to K^{*0}\mu^+\mu^-$ decay using $3\,\mathrm{fb}^{-1}$ of integrated luminosity

The LHCb collaboration

E-mail: christoph.langenbruch@cern.ch

ABSTRACT: An angular analysis of the $B^0 \to K^{*0}(\to K^+\pi^-)\mu^+\mu^-$ decay is presented. The dataset corresponds to an integrated luminosity of $3.0\,\mathrm{fb}^{-1}$ of pp collision data collected at the LHCb experiment. The complete angular information from the decay is used to determine CP-averaged observables and CP asymmetries, taking account of possible contamination from decays with the $K^+\pi^-$ system in an S-wave configuration. The angular observables and their correlations are reported in bins of q^2, the invariant mass squared of the dimuon system. The observables are determined both from an unbinned maximum likelihood fit and by using the principal moments of the angular distribution. In addition, by fitting for q^2-dependent decay amplitudes in the region $1.1 < q^2 < 6.0\,\mathrm{GeV}^2/c^4$, the zero-crossing points of several angular observables are computed. A global fit is performed to the complete set of CP-averaged observables obtained from the maximum likelihood fit. This fit indicates differences with predictions based on the Standard Model at the level of 3.4 standard deviations. These differences could be explained by contributions from physics beyond the Standard Model, or by an unexpectedly large hadronic effect that is not accounted for in the Standard Model predictions.

Contents

1 Introduction

The decay $B^0 \to K^{*0}\mu^+\mu^-$ proceeds via a $b \to s$ quark flavour-changing neutral current (FCNC) transition. In the Standard Model (SM) the decay is therefore forbidden at tree level and occurs, at lowest order, via electroweak penguin and box processes. In extensions of the SM, new particles may enter in competing processes and can significantly change the branching fraction of the decay and the angular distribution of the final-state particles. Angular observables are of particular interest, since theoretical predictions of such observables tend to be less affected by the hadronic uncertainties associated with the $B^0 \to K^{*0}$ transition. Throughout this paper K^{*0} is used to refer to the $K^*(892)^0$ resonance.

The LHCb collaboration previously determined a set of angular observables in the $B^0 \to K^{*0}\mu^+\mu^-$ decay,[1] using data collected during 2011, corresponding to an integrated luminosity of $1.0\,\mathrm{fb}^{-1}$ [1]. Different subsets of these angular observables have also been measured by the BaBar, Belle, CDF and CMS collaborations [2–7] and all of these measurements are in good agreement with SM predictions. The LHCb collaboration has also used the 2011 dataset to determine an alternative set of angular observables that have reduced theoretical uncertainties [8]. In contrast to the previous analyses, these observables cannot be extracted from single angle distributions. This second LHCb analysis found a local deviation with respect to the SM prediction in one observable, P_5', with a significance corresponding to 3.7 standard deviations. Possible interpretations of this discrepancy and the consistency of all of the measurements of $b \to s$ transitions have been widely discussed in the literature [9–21].

The present paper describes an updated angular analysis of the $B^0 \to K^{*0}\mu^+\mu^-$ decay, using the LHCb Run 1 data sample, corresponding to an integrated luminosity of $3.0\,\mathrm{fb}^{-1}$. The data were recorded in pp collisions at centre-of-mass energies of 7 and 8 TeV during 2011 and 2012, respectively. All previous analyses of the $B^0 \to K^{*0}\mu^+\mu^-$ decay have extracted only part of the information available, by fitting simplified forms of the angular distribution. This paper presents a complete set of observables for the first time, based on the full angular distribution. The simultaneous determination of these observables allows correlations between the measured quantities to be computed, enabling the use of the results in global fits to theoretical models. This is critical to understand whether SM dynamics are sufficient to explain the above discrepancy, or if extensions to the SM are necessary.

The structure of this paper is as follows. In section 2, the angular distribution and observables for the $B^0 \to K^{*0}\mu^+\mu^-$ decay are presented. Section 3 describes the experimental setup. The reconstruction and selection of the $B^0 \to K^{*0}\mu^+\mu^-$ candidates and sources of background are presented in section 4. The method used to correct the angular

---

[1] The inclusion of charge conjugate processes is implied throughout this paper, unless otherwise noted.

distribution for experimental effects is detailed in section 5 and the parameterisation of the mass distribution is described in section 6. The determination of the angular observables is detailed in section 7, and section 8 discusses sources of systematic uncertainty. Results are given in section 9 and the compatibility with predictions based on the Standard Model is discussed in section 10. Finally, conclusions are presented in section 11.

2 Angular distribution and observables

The final state of the decay $B^0 \to K^{*0}\mu^+\mu^-$ can be described by q^2, the invariant mass squared of the dimuon system, and three decay angles $\vec{\Omega} = (\cos\theta_l, \cos\theta_K, \phi)$. The angle between the μ^+ (μ^-) and the direction opposite to that of the B^0 ($\overline{B}^0$) in the rest frame of the dimuon system is denoted θ_l. In this analysis, the K^{*0} meson is reconstructed through the decay $K^{*0} \to K^+\pi^-$. The angle between the direction of the K^+ (K^-) and the B^0 ($\overline{B}^0$) in the rest frame of the K^{*0} ($\overline{K}^{*0}$) system is denoted θ_K. The angle between the plane defined by the dimuon pair and the plane defined by the kaon and pion in the B^0 ($\overline{B}^0$) rest frame is denoted ϕ. More details of the angular basis adopted in this analysis are given in appendix A of ref. [1].

The differential decay rates of $\overline{B}^0 \to \overline{K}^{*0}\mu^+\mu^-$ and $B^0 \to K^{*0}\mu^+\mu^-$ decays, in terms of q^2 and the three angles, are given by

$$\frac{\mathrm{d}^4\Gamma[\overline{B}^0 \to \overline{K}^{*0}\mu^+\mu^-]}{\mathrm{d}q^2\,\mathrm{d}\vec{\Omega}} = \frac{9}{32\pi}\sum_i I_i(q^2)f_i(\vec{\Omega}) \;\; \text{and}$$

$$\frac{\mathrm{d}^4\bar{\Gamma}[B^0 \to K^{*0}\mu^+\mu^-]}{\mathrm{d}q^2\,\mathrm{d}\vec{\Omega}} = \frac{9}{32\pi}\sum_i \bar{I}_i(q^2)f_i(\vec{\Omega}),$$

(2.1)

where Γ ($\bar{\Gamma}$) refers to decays involving a b ($\bar{b}$) quark and hence a $\overline{B}^0$ (B^0) meson, the terms $f_i(\vec{\Omega})$ are formed from combinations of spherical harmonics and the I_i ($\bar{I}_i$) are q^2-dependent angular observables. The I_i can be expressed as bilinear combinations of six complex decay amplitudes, $\mathcal{A}_{0,\|,\perp}^{\mathrm{L,R}}$, which correspond to the different transversity states of the K^{*0} meson and the different (left- and right-handed) chiralities of the dimuon system. An additional suffix s or c is conventionally added to some of the I_i terms to indicate that they have a $\sin^2\theta_K$ or $\cos^2\theta_K$ dependence. When q^2 is sufficiently large ($q^2 \gtrsim 1\,\mathrm{GeV}^2/c^4$), the muons can be considered massless. The list of the angular terms and observables that remain in this massless limit is given in table 1.

Following the notation of ref. [22], q^2-dependent CP averages, S_i, and CP asymmetries, A_i, can be defined as

$$S_i = \left(I_i + \bar{I}_i\right) \Big/ \left(\frac{\mathrm{d}\Gamma}{\mathrm{d}q^2} + \frac{\mathrm{d}\bar{\Gamma}}{\mathrm{d}q^2}\right) \;\; \text{and}$$

$$A_i = \left(I_i - \bar{I}_i\right) \Big/ \left(\frac{\mathrm{d}\Gamma}{\mathrm{d}q^2} + \frac{\mathrm{d}\bar{\Gamma}}{\mathrm{d}q^2}\right).$$

(2.2)

In the massless limit, the CP-averaged observables $S_{1(s,c)}$ and $S_{2(s,c)}$ obey the relations $S_{1s} = 3S_{2s}$, $S_{1c} = -S_{2c}$ and $\frac{3}{4}(2S_{1s} + S_{1c}) - \frac{1}{4}(2S_{2s} + S_{2c}) = 1$ (see for example ref. [22]).

These relationships reduce the number of independent CP-averaged observables from eleven to eight. The relations between the observables also hold to a good approximation for $q^2 < 1\,\mathrm{GeV}^2/c^4$ and are therefore adopted for the full q^2 range. The S_{1c} observable corresponds to the fraction of longitudinal polarisation of the K^{*0} meson and is therefore more commonly referred to as F_L, with

$$F_\mathrm{L} = S_{1c} = \frac{|\mathcal{A}_0^\mathrm{L}|^2 + |\mathcal{A}_0^\mathrm{R}|^2}{|\mathcal{A}_0^\mathrm{L}|^2 + |\mathcal{A}_0^\mathrm{R}|^2 + |\mathcal{A}_\parallel^\mathrm{L}|^2 + |\mathcal{A}_\parallel^\mathrm{R}|^2 + |\mathcal{A}_\perp^\mathrm{L}|^2 + |\mathcal{A}_\perp^\mathrm{R}|^2}\,. \tag{2.3}$$

It is also conventional to replace S_{6s} by the forward-backward asymmetry of the dimuon system A_FB, with $A_\mathrm{FB} = \frac{3}{4}S_{6s}$. The CP-averaged angular distribution of the $B^0 \to K^{*0}\mu^+\mu^-$ decay can then be written as

$$\begin{aligned}
\frac{1}{\mathrm{d}(\Gamma + \bar{\Gamma})/\mathrm{d}q^2}\frac{\mathrm{d}^4(\Gamma + \bar{\Gamma})}{\mathrm{d}q^2\,\mathrm{d}\vec{\Omega}} = \frac{9}{32\pi}\bigg[&\frac{3}{4}(1 - F_\mathrm{L})\sin^2\theta_K + F_\mathrm{L}\cos^2\theta_K \\
&+ \frac{1}{4}(1 - F_\mathrm{L})\sin^2\theta_K\cos 2\theta_l \\
&- F_\mathrm{L}\cos^2\theta_K\cos 2\theta_l + S_3\sin^2\theta_K\sin^2\theta_l\cos 2\phi \\
&+ S_4\sin 2\theta_K\sin 2\theta_l\cos\phi + S_5\sin 2\theta_K\sin\theta_l\cos\phi \\
&+ \frac{4}{3}A_\mathrm{FB}\sin^2\theta_K\cos\theta_l + S_7\sin 2\theta_K\sin\theta_l\sin\phi \\
&+ S_8\sin 2\theta_K\sin 2\theta_l\sin\phi + S_9\sin^2\theta_K\sin^2\theta_l\sin 2\phi\bigg]\,.
\end{aligned} \tag{2.4}$$

Additional sets of observables, for which the leading $B^0 \to K^{*0}$ form-factor uncertainties cancel, can be built from F_L and S_3–S_9. Examples of such *optimised* observables include the transverse asymmetry $A_\mathrm{T}^{(2)}$ [23], where $A_\mathrm{T}^{(2)} = 2S_3/(1 - F_\mathrm{L})$, and the $P_i^{(\prime)}$ series of observables [24]. In this paper the notation used is

$$\begin{aligned}
P_1 &= \frac{2\,S_3}{(1 - F_\mathrm{L})} = A_\mathrm{T}^{(2)}\,, \\
P_2 &= \frac{2}{3}\frac{A_\mathrm{FB}}{(1 - F_\mathrm{L})}\,, \\
P_3 &= \frac{-S_9}{(1 - F_\mathrm{L})}\,, \\
P_{4,5,8}' &= \frac{S_{4,5,8}}{\sqrt{F_\mathrm{L}(1 - F_\mathrm{L})}}\,, \\
P_6' &= \frac{S_7}{\sqrt{F_\mathrm{L}(1 - F_\mathrm{L})}}\,.
\end{aligned} \tag{2.5}$$

The definition of the P_i' observables differs from that of ref. [24], but is consistent with the notation used in the LHCb analysis of ref. [8].

In addition to the resonant P-wave K^{*0} contribution to the $K^+\pi^-\mu^+\mu^-$ final state, the $K^+\pi^-$ system can also be in an S-wave configuration. The addition of an S-wave component introduces two new complex amplitudes, $\mathcal{A}_\mathrm{S}^\mathrm{L,R}$, and results in the six additional

angular terms that are given in the lower part of table 1. In the analyses described in refs. [1, 8] the S-wave contribution, which is expected to be approximately 5%, was treated as a systematic uncertainty. The presence of a $K^+\pi^-$ system in an S-wave configuration modifies the angular distribution to

$$
\frac{1}{\mathrm{d}(\Gamma + \bar{\Gamma})/\mathrm{d}q^2} \frac{\mathrm{d}^4(\Gamma + \bar{\Gamma})}{\mathrm{d}q^2\,\mathrm{d}\vec{\Omega}}\bigg|_{\mathrm{S+P}} = (1 - F_{\mathrm{S}}) \frac{1}{\mathrm{d}(\Gamma + \bar{\Gamma})/\mathrm{d}q^2} \frac{\mathrm{d}^4(\Gamma + \bar{\Gamma})}{\mathrm{d}q^2\,\mathrm{d}\vec{\Omega}}\bigg|_{\mathrm{P}}
$$
$$
+ \frac{3}{16\pi} F_{\mathrm{S}} \sin^2\theta_l
$$
$$
+ \frac{9}{32\pi}(S_{11} + S_{13}\cos 2\theta_l)\cos\theta_K \qquad (2.6)
$$
$$
+ \frac{9}{32\pi}(S_{14}\sin 2\theta_l + S_{15}\sin\theta_l)\sin\theta_K \cos\phi
$$
$$
+ \frac{9}{32\pi}(S_{16}\sin\theta_l + S_{17}\sin 2\theta_l)\sin\theta_K \sin\phi\,,
$$

where F_{S} denotes the S-wave fraction,

$$
F_{\mathrm{S}} = \frac{|\mathcal{A}_{\mathrm{S}}^{\mathrm{L}}|^2 + |\mathcal{A}_{\mathrm{S}}^{\mathrm{R}}|^2}{|\mathcal{A}_{\mathrm{S}}^{\mathrm{L}}|^2 + |\mathcal{A}_{\mathrm{S}}^{\mathrm{R}}|^2 + |\mathcal{A}_{0}^{\mathrm{L}}|^2 + |\mathcal{A}_{0}^{\mathrm{R}}|^2 + |\mathcal{A}_{\parallel}^{\mathrm{L}}|^2 + |\mathcal{A}_{\parallel}^{\mathrm{R}}|^2 + |\mathcal{A}_{\perp}^{\mathrm{L}}|^2 + |\mathcal{A}_{\perp}^{\mathrm{R}}|^2}\,, \qquad (2.7)
$$

and the terms S_{11}, S_{13}–S_{17} arise from interference between the S- and P-wave amplitudes. Note that F_{S} replaces the terms S_{10} and S_{12}, with $F_{\mathrm{S}} = 3S_{10} = -3S_{12}$. Throughout this paper, F_{S} and the interference terms between the S- and P-wave are treated as nuisance parameters.

Due to the flavour specific final state of the decay, the CP asymmetries A_i can be determined from differences in the angular distributions between B^0 and $\bar{B}^0$ decays.

In this analysis, three separate techniques are used to study the angular distribution:

1. An unbinned maximum likelihood fit is used to determine the CP-averaged observables F_{L}, A_{FB}, and S_3–S_9, as well as the CP asymmetries A_3–A_9, averaged over bins of q^2. In addition, the $P_i^{(\prime)}$ observables are determined by reparameterising the likelihood fit. The data are analysed in q^2 bins of approximately $2\,\mathrm{GeV}^2/c^4$ width and also in wider $1.1 < q^2 < 6.0\,\mathrm{GeV}^2/c^4$ and $15.0 < q^2 < 19.0\,\mathrm{GeV}^2/c^4$ bins for which there are particularly precise theoretical predictions. The unbinned maximum likelihood fit is described in section 7.1.

2. The same observables are also determined using principal angular moments. This so-called *method of moments* gives an approximately 15% less precise determination of the observables than the likelihood fit but is particularly robust for low signal yields and does not require a complex angular fit [25]. This allows the observables to be determined in approximately $1\,\mathrm{GeV}^2/c^4$ wide q^2 bins, which gives additional shape information that is useful in regions where the observables vary rapidly with q^2. The method is described in section 7.2.

3. Finally, the observables S_4, S_5 and A_{FB} vary as a function of q^2 and are known to change sign in the SM. By fitting for the decay amplitudes as a function of q^2, the q^2 values at which these observables cross zero can be determined. At leading

i	I_i	f_i
$1s$	$\frac{3}{4}\left[\lvert\mathcal{A}_\parallel^{\text{L}}\rvert^2 + \lvert\mathcal{A}_\perp^{\text{L}}\rvert^2 + \lvert\mathcal{A}_\parallel^{\text{R}}\rvert^2 + \lvert\mathcal{A}_\perp^{\text{R}}\rvert^2\right]$	$\sin^2\theta_K$
$1c$	$\lvert\mathcal{A}_0^{\text{L}}\rvert^2 + \lvert\mathcal{A}_0^{\text{R}}\rvert^2$	$\cos^2\theta_K$
$2s$	$\frac{1}{4}\left[\lvert\mathcal{A}_\parallel^{\text{L}}\rvert^2 + \lvert\mathcal{A}_\perp^{\text{L}}\rvert^2 + \lvert\mathcal{A}_\parallel^{\text{R}}\rvert^2 + \lvert\mathcal{A}_\perp^{\text{R}}\rvert^2\right]$	$\sin^2\theta_K\cos 2\theta_l$
$2c$	$-\lvert\mathcal{A}_0^{\text{L}}\rvert^2 - \lvert\mathcal{A}_0^{\text{R}}\rvert^2$	$\cos^2\theta_K\cos 2\theta_l$
3	$\frac{1}{2}\left[\lvert\mathcal{A}_\perp^{\text{L}}\rvert^2 - \lvert\mathcal{A}_\parallel^{\text{L}}\rvert^2 + \lvert\mathcal{A}_\perp^{\text{R}}\rvert^2 - \lvert\mathcal{A}_\parallel^{\text{R}}\rvert^2\right]$	$\sin^2\theta_K\sin^2\theta_l\cos 2\phi$
4	$\sqrt{\frac{1}{2}}\text{Re}(\mathcal{A}_0^{\text{L}}\mathcal{A}_\parallel^{\text{L}*} + \mathcal{A}_0^{\text{R}}\mathcal{A}_\parallel^{\text{R}*})$	$\sin 2\theta_K\sin 2\theta_l\cos\phi$
5	$\sqrt{2}\text{Re}(\mathcal{A}_0^{\text{L}}\mathcal{A}_\perp^{\text{L}*} - \mathcal{A}_0^{\text{R}}\mathcal{A}_\perp^{\text{R}*})$	$\sin 2\theta_K\sin\theta_l\cos\phi$
$6s$	$2\text{Re}(\mathcal{A}_\parallel^{\text{L}}\mathcal{A}_\perp^{\text{L}*} - \mathcal{A}_\parallel^{\text{R}}\mathcal{A}_\perp^{\text{R}*})$	$\sin^2\theta_K\cos\theta_l$
7	$\sqrt{2}\text{Im}(\mathcal{A}_0^{\text{L}}\mathcal{A}_\parallel^{\text{L}*} - \mathcal{A}_0^{\text{R}}\mathcal{A}_\parallel^{\text{R}*})$	$\sin 2\theta_K\sin\theta_l\sin\phi$
8	$\sqrt{\frac{1}{2}}\text{Im}(\mathcal{A}_0^{\text{L}}\mathcal{A}_\perp^{\text{L}*} + \mathcal{A}_0^{\text{R}}\mathcal{A}_\perp^{\text{R}*})$	$\sin 2\theta_K\sin 2\theta_l\sin\phi$
9	$\text{Im}(\mathcal{A}_\parallel^{\text{L}*}\mathcal{A}_\perp^{\text{L}} + \mathcal{A}_\parallel^{\text{R}*}\mathcal{A}_\perp^{\text{R}})$	$\sin^2\theta_K\sin^2\theta_l\sin 2\phi$
10	$\frac{1}{3}\left[\lvert\mathcal{A}_{\text{S}}^{\text{L}}\rvert^2 + \lvert\mathcal{A}_{\text{S}}^{\text{R}}\rvert^2\right]$	1
11	$\sqrt{\frac{4}{3}}\text{Re}(\mathcal{A}_{\text{S}}^{\text{L}}\mathcal{A}_0^{\text{L}*} + \mathcal{A}_{\text{S}}^{\text{R}}\mathcal{A}_0^{\text{R}*})$	$\cos\theta_K$
12	$-\frac{1}{3}\left[\lvert\mathcal{A}_{\text{S}}^{\text{L}}\rvert^2 + \lvert\mathcal{A}_{\text{S}}^{\text{R}}\rvert^2\right]$	$\cos 2\theta_l$
13	$-\sqrt{\frac{4}{3}}\text{Re}(\mathcal{A}_{\text{S}}^{\text{L}}\mathcal{A}_0^{\text{L}*} + \mathcal{A}_{\text{S}}^{\text{R}}\mathcal{A}_0^{\text{R}*})$	$\cos\theta_K\cos 2\theta_l$
14	$\sqrt{\frac{2}{3}}\text{Re}(\mathcal{A}_{\text{S}}^{\text{L}}\mathcal{A}_\parallel^{\text{L}*} + \mathcal{A}_{\text{S}}^{\text{R}}\mathcal{A}_\parallel^{\text{R}*})$	$\sin\theta_K\sin 2\theta_l\cos\phi$
15	$\sqrt{\frac{8}{3}}\text{Re}(\mathcal{A}_{\text{S}}^{\text{L}}\mathcal{A}_\perp^{\text{L}*} - \mathcal{A}_{\text{S}}^{\text{R}}\mathcal{A}_\perp^{\text{R}*})$	$\sin\theta_K\sin\theta_l\cos\phi$
16	$\sqrt{\frac{8}{3}}\text{Im}(\mathcal{A}_{\text{S}}^{\text{L}}\mathcal{A}_\parallel^{\text{L}*} - \mathcal{A}_{\text{S}}^{\text{R}}\mathcal{A}_\parallel^{\text{R}*})$	$\sin\theta_K\sin\theta_l\sin\phi$
17	$\sqrt{\frac{2}{3}}\text{Im}(\mathcal{A}_{\text{S}}^{\text{L}}\mathcal{A}_\perp^{\text{L}*} + \mathcal{A}_{\text{S}}^{\text{R}}\mathcal{A}_\perp^{\text{R}*})$	$\sin\theta_K\sin 2\theta_l\sin\phi$

Table 1. Angular observables I_j and their corresponding angular terms for dimuon masses that are much larger than twice the muon mass. The terms in the lower part of the table arise from the $K^+\pi^-$ S-wave contribution to the $K^+\pi^-\mu^+\mu^-$ final state. The $\bar{I}_i$ coefficients are obtained by making the substitution $\mathcal{A}\to\bar{\mathcal{A}}$, $i.e.$ by complex conjugation of the weak phases in the amplitudes.

order these zero-crossing points are free from $B^0\to K^{*0}$ form-factor uncertainties and consequently provide a precision test of the SM [26, 27]. The method is applied in the range $1.1 < q^2 < 6.0\,\text{GeV}^2/c^4$ and is described in section 7.3.

The three methods are complementary, but their results are correlated and cannot be combined. Method 1 is the most precise and is therefore used to compare to the SM predictions. The q^2 bins used for the likelihood fit of the angular observables and the method of moments are given in tables 4 and 7 of appendix A, respectively.

3   Detector and simulation

The LHCb detector [28, 29] is a single-arm forward spectrometer, covering the pseudorapidity range $2 < \eta < 5$, designed for the study of particles containing b or c quarks. The detector includes a high-precision tracking system consisting of a silicon-strip vertex detector surrounding the pp interaction region, a large-area silicon-strip detector located upstream of a dipole magnet with a bending power of about $4\,\mathrm{Tm}$, and three stations of silicon-strip detectors and straw drift tubes placed downstream of the magnet. The tracking system provides a measurement of momentum, p, of charged particles with a relative uncertainty that varies from 0.5% at low momentum to 1.0% at $200\,\mathrm{GeV}/c$. The minimum distance of a track to a primary pp interaction vertex (PV), the impact parameter, is measured with a resolution of $(15 + 29/p_{\mathrm{T}})\,\mathrm{\mu m}$, where p_{T} is the component of the momentum transverse to the beam, in GeV/c. Different types of charged hadrons are distinguished using information from two ring-imaging Cherenkov (RICH) detectors. Photons, electrons and hadrons are identified by a calorimeter system consisting of scintillating-pad and preshower detectors, an electromagnetic calorimeter and a hadronic calorimeter. Muons are identified by a system composed of alternating layers of iron and multiwire proportional chambers. The online event selection is performed by a trigger, which consists of a hardware stage, based on information from the calorimeter and muon systems, followed by a software stage, which applies a full event reconstruction [30].

Simulated signal events are used to determine the impact of the detector geometry, trigger, reconstruction and candidate selection on the angular distribution of the signal. In addition, simulated samples are used to estimate the contribution of possible background processes. In the simulation, pp collisions are generated using PYTHIA [31, 32] with a specific LHCb configuration [33]. Decays of hadronic particles are described by EVTGEN [34], in which final-state radiation is generated using PHOTOS [35]. The interaction of the generated particles with the detector, and its response, are implemented using the GEANT4 toolkit [36, 37] as described in ref. [38]. Data-driven corrections are applied to the simulation to account for a small level of mismodelling of the detector occupancy, B^0 momentum and B^0 vertex quality. Similarly, the simulated particle identification (PID) performance is corrected to match that determined from control samples selected from the data.

4   Selection of signal candidates

The $B^0 \to K^{*0}\mu^+\mu^-$ signal candidates are required to pass a hardware trigger, which selects events containing at least one muon with $p_{\mathrm{T}} > 1.48\,\mathrm{GeV}/c$ in the $7\,\mathrm{TeV}$ data or $p_{\mathrm{T}} > 1.76\,\mathrm{GeV}/c$ in the $8\,\mathrm{TeV}$ data. In the subsequent software trigger, at least one of the final-state particles is required to have both $p_{\mathrm{T}} > 0.8\,\mathrm{GeV}/c$ and impact parameter larger than $100\,\mathrm{\mu m}$ with respect to all PVs in the event. Finally, the tracks of two or more of the final-state particles are required to form a vertex that is significantly displaced from any PV.

Signal candidates are formed from a pair of oppositely charged tracks that are identified as muons, combined with a K^{*0} meson candidate. The K^{*0} candidate is formed from two

charged tracks that are identified as a kaon and a pion, respectively. The four tracks of the final-state particles are required to have a significant impact parameter with respect to all PVs in the event. The tracks are then fitted to a common vertex, which is required to be of good quality. The impact parameter of the B^0 candidate with respect to one of the PVs is required to be small and the vertex of the B^0 candidate is required to be significantly displaced from the same PV. The angle $\theta_{\rm DIRA}$ between the reconstructed B^0 momentum and the vector connecting the PV to the reconstructed B^0 decay vertex is required to be small. Candidates are required to have reconstructed B^0 invariant mass, $m(K^+\pi^-\mu^+\mu^-)$, in the range $5170 < m(K^+\pi^-\mu^+\mu^-) < 5700\,{\rm MeV}/c^2$. Finally, the reconstructed mass of the $K^+\pi^-$ system, $m(K^+\pi^-)$, is required to be in the range $796 < m(K^+\pi^-) < 996\,{\rm MeV}/c^2$.

Background formed by combining particles from different b- and c-hadron decays (referred to as *combinatorial* background) is further reduced using a boosted decision tree (BDT) [39, 40], which is trained using data. As a proxy for the signal decay, $B^0 \to J/\psi K^{*0}$ decays are used to train the BDT, where the J/ψ is reconstructed through its decay into $\mu^+\mu^-$. Candidates from the upper mass sideband $5350 < m(K^+\pi^-\mu^+\mu^-) < 7000\,{\rm MeV}/c^2$ are used as a proxy for the background. As input variables, the BDT uses the reconstructed B^0 lifetime and vertex fit quality, the momentum and transverse momentum of the B^0 candidate, $\cos\theta_{\rm DIRA}$, particle identification information from the RICH detectors and the muon system, as well as variables describing the isolation of the final state tracks [41]. To best exploit the data available for training, the k-folding technique [42] is employed with $k = 10$. At the chosen working point, the BDT has a background rejection of 97% and a signal efficiency of 85%. The signal efficiency and background rejection of the BDT is uniform in $m(K^+\pi^-\mu^+\mu^-)$ and $m(K^+\pi^-)$. The distortion induced in q^2 and the angular distributions is discussed in section 5.

The $K^+\pi^-\mu^+\mu^-$ invariant mass versus q^2 for candidates that pass the full selection is shown in figure 1. The $B^0 \to K^{*0}\mu^+\mu^-$ signal candidates are clearly visible as a vertical band. The contributions from the decays $B^0 \to J/\psi K^{*0}$ and $B^0 \to \psi(2S)K^{*0}$, which proceed through tree-level $b \to c\bar{c}s$ transitions, have a dimuon mass consistent with the known J/ψ or $\psi(2S)$ meson mass and $m(K^+\pi^-\mu^+\mu^-)$ consistent with that of the known B^0 meson mass. The horizontal bands are formed from combinatorial background comprising a genuine J/ψ or $\psi(2S)$ meson and a K^{*0} candidate selected from elsewhere in the event.

4.1 Background composition

In addition to combinatorial background, there are several sources of background that accumulate in $m(K^+\pi^-\mu^+\mu^-)$ and can potentially mimic the signal decay if they are mis-reconstructed in the detector. These are referred to as *peaking* backgrounds. Contamination from peaking backgrounds is estimated using samples of simulated events.

The tree-level decays $B^0 \to J/\psi K^{*0}$ and $B^0 \to \psi(2S)K^{*0}$ dominate in the regions $8.0 < q^2 < 11.0\,{\rm GeV}^2/c^4$ and $12.5 < q^2 < 15.0\,{\rm GeV}^2/c^4$, respectively, and these q^2 regions are therefore excluded from the analysis of the signal decay. However, these decays can still form a source of background if the μ^- (μ^+) is misidentified as a π^- (K^+) and the π^- (K^+) is misidentified as a μ^- (μ^+). To remove this background, candidates are rejected if the π^- (K^+) satisfies the muon identification criteria and the mass of the $\pi^-\mu^+$ ($K^+\mu^-$) system,
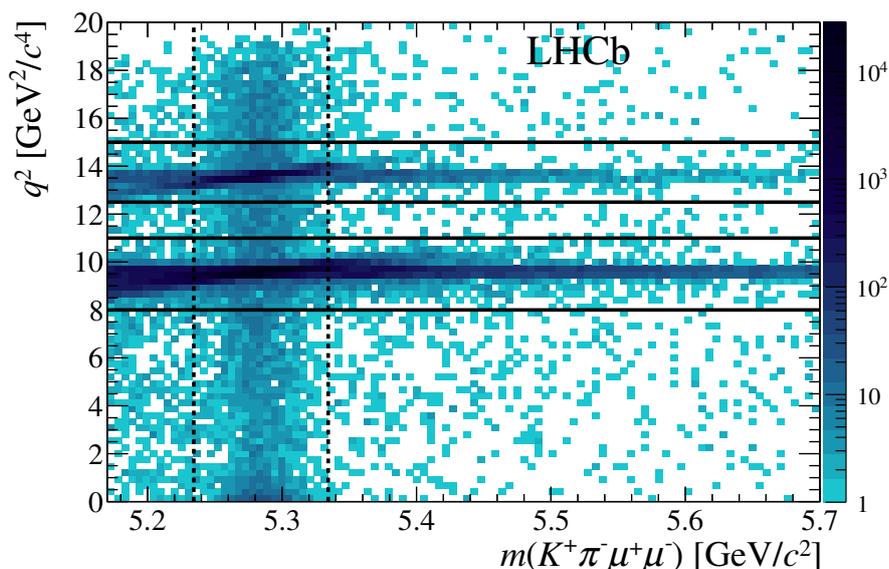
Figure 1. Invariant mass of the $K^+\pi^-\mu^+\mu^-$ system versus q^2. The decay $B^0 \to K^{*0}\mu^+\mu^-$ is clearly visible inside the dashed vertical lines. The horizontal lines denote the charmonium regions, where the tree-level decays $B^0 \to J/\psi K^{*0}$ and $B^0 \to \psi(2S)K^{*0}$ dominate. These candidates are excluded from the analysis.

when the π^- (K^+) is assigned the muon mass, is consistent with that of a J/ψ or $\psi(2S)$ meson. Possible pollution from $B^0 \to K^{*0}\phi(\to \mu^+\mu^-)$ decays is removed by excluding from the analysis the q^2 region $0.98 < q^2 < 1.10\,\mathrm{GeV}^2/c^4$.

The decay $\Lambda_b^0 \to pK^-\mu^+\mu^-$, which can proceed via *e.g.* the $\Lambda(1520)$ resonance, can be a source of peaking background if the proton is misidentified as a pion. This background is suppressed by rejecting candidates where the pion is not unambiguously identified by the RICH detectors and which have a mass close to the known Λ_b^0 mass, when the pion is assigned the proton mass. Similarly, $\Lambda_b^0 \to pK^-\mu^+\mu^-$ backgrounds with double misidentification of the hadrons, *i.e.* where the proton is misidentified as a kaon and the kaon is misidentified as a pion, are suppressed using PID information.

The decay $B_s^0 \to \phi(\to K^+K^-)\mu^+\mu^-$ can mimic the signal decay if one of the kaons is misidentified as a pion. This background is suppressed by requiring stringent PID criteria if, after assigning the kaon mass to the pion candidate, the reconstructed invariant masses of the B^0 and K^{*0} candidates are consistent with the known B_s^0 and ϕ masses.

The decay $B^+ \to K^+\mu^+\mu^-$ can form a background if a low momentum pion from elsewhere in the event is added to form a four-particle final state. The resulting invariant mass $m(K^+\pi^-\mu^+\mu^-)$ will be larger than the known B^0 mass but can contribute to the upper mass-sideband. Such decays can therefore distort the estimate of the angular distribution of the residual background, which is assessed from this sideband. This background is suppressed by removing candidates with $5220 < m(K^+\mu^+\mu^-) < 5340\,\mathrm{MeV}/c^2$. It is also possible to have backgrounds from $B^{0,+} \to K^{*0,+}\mu^+\mu^-$ decays, where the pion from the K^* meson is replaced by another pion from the rest of the event. This background does

not peak in the signal region and is considered as part of the combinatorial background. Finally, $B^0 \to K^{*0}\mu^+\mu^-$ decays can form a background to $\overline{B}^0 \to \overline{K}^{*0}\mu^+\mu^-$ decays (and vice versa) if the K^+ (K^-) is misidentified as the π^+ (π^-) and the π^- (π^+) is misidentified as the K^- (K^+). These misidentified decays are referred to as *signal swaps* and are suppressed using PID information.

After all vetoes are applied, the largest peaking background contribution is from $\Lambda_b^0 \to pK^-\mu^+\mu^-$ decays. The residual background from these decays is expected to be at a level of $(1.0 \pm 0.4)\%$ of the signal yield. The next largest backgrounds are $B^0 \to K^{*0}\mu^+\mu^-$ signal swaps at $(0.64 \pm 0.06)\%$, misidentified $B_s^0 \to \phi\mu^+\mu^-$ events at $(0.33 \pm 0.12)\%$ and $B^0 \to J/\psi K^{*0}$ decays with double misidentification at $(0.05 \pm 0.05)\%$ of the signal yield. All of the sources of peaking background are sufficiently small such that they are neglected in the angular analysis but are considered further as sources of systematic uncertainty. The background from b-hadron decays where two hadrons are misidentified as muons is negligible. The largest residual background is combinatorial in nature and varies smoothly with $m(K^+\pi^-\mu^+\mu^-)$, $m(K^+\pi^-)$ and the decay angles.

5   Angular acceptance

The triggering, reconstruction and selection criteria distort the distributions of the decay angles θ_l, θ_K and ϕ, as well as the q^2 distribution, giving rise to so-called *acceptance effects*. The dominant acceptance effects come from momentum and impact parameter requirements. In particular, the implicit momentum threshold that is required for tracks to traverse the magnetic spectrometer removes low momentum particles. In contrast to the previous LHCb analyses [1, 8], the acceptance is not assumed to factorise in the three decay angles. Instead, the efficiency is parameterised in four dimensions, according to

$$\varepsilon(\cos\theta_l, \cos\theta_K, \phi, q^2) = \sum_{ijmn} c_{ijmn} L_i(\cos\theta_l) L_j(\cos\theta_K) L_m(\phi) L_n(q^2), \quad (5.1)$$

where the terms $L_h(x)$ denote Legendre polynomials of order h and the observables are rescaled to the range $-1 < x < +1$ when evaluating the polynomial. For $\cos\theta_l$, $\cos\theta_K$ and ϕ, the sum in eq. (5.1) encompasses $L_h(x)$ up to fourth, fifth and sixth order, respectively. The q^2 parameterisation comprises $L_h(x)$ up to fifth order. The coefficients c_{ijmn} are determined using a principal moment analysis of simulated three-body $B^0 \to K^{*0}\mu^+\mu^-$ phase-space decays. As the efficiency is parameterised in terms of all of the relevant kinematic variables needed to describe the decay, it does not depend on the model used in the simulation.

The angular acceptance in $\cos\theta_l$, $\cos\theta_K$ and ϕ is shown for $0.10 < q^2 < 0.98\,\text{GeV}^2/c^4$ and $18.0 < q^2 < 19.0\,\text{GeV}^2/c^4$ in figure 2. The acceptance varies smoothly as a function of q^2 between these extremes. The acceptance as a function of q^2, after integrating over the decay angles, is also shown. The description of the angular acceptance is cross-checked, for $q^2 = m^2(J/\psi)$, using the decay $B^0 \to J/\psi K^{*0}$. This decay can be selected in the data with background contamination below 1% and the angular structure has been determined by
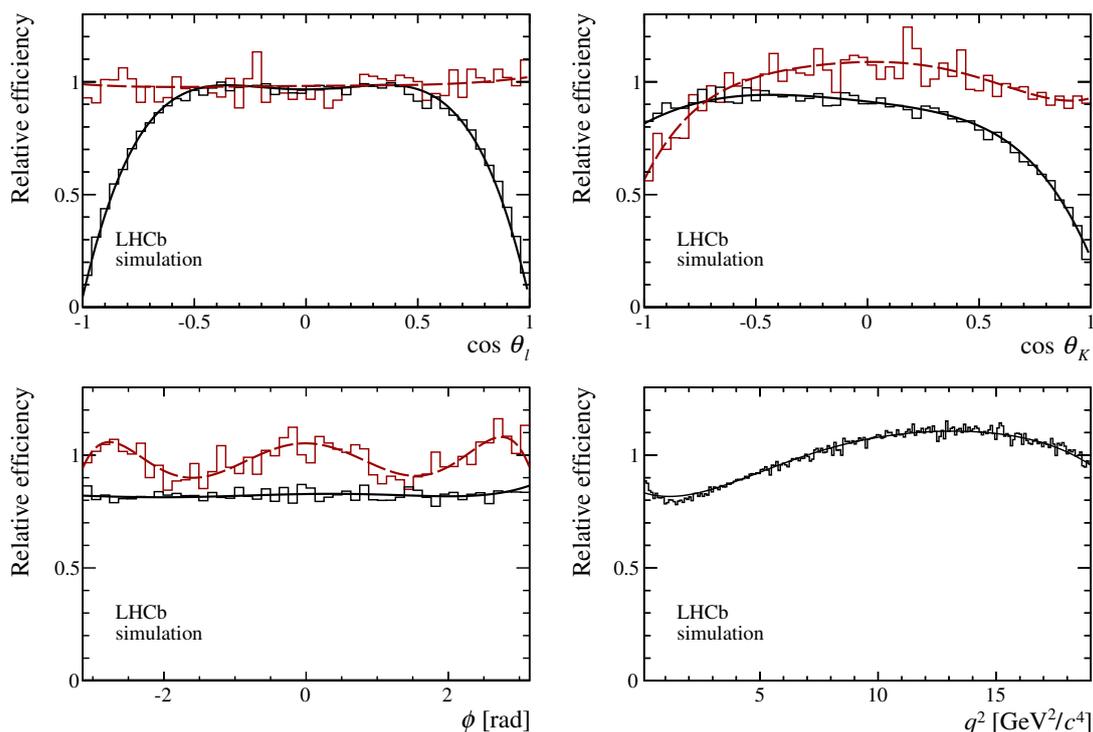
Figure 2. Relative efficiency in $\cos\theta_l$, $\cos\theta_K$, ϕ and q^2, as determined from a principal moment analysis of simulated three-body $B^0 \to K^{*0}\mu^+\mu^-$ phase-space decays. The efficiency as a function of $\cos\theta_l$, $\cos\theta_K$ and ϕ is shown for the regions $0.1 < q^2 < 0.98\,\mathrm{GeV^2}/c^4$ (black solid line) and $18.0 < q^2 < 19.0\,\mathrm{GeV^2}/c^4$ (red dashed line). The efficiency as a function of q^2 is shown after integrating over the decay angles. The histograms indicate the distribution of the simulated three-body $B^0 \to K^{*0}\mu^+\mu^-$ phase-space decays used to determine the acceptance.

measurements made by the BaBar, Belle and LHCb collaborations [43–45]. With the acceptance correction derived using the above method, the $B^0 \to J/\psi K^{*0}$ angular observables obtained from the LHCb data are in good agreement with these previous measurements. The angular fit of the $B^0 \to J/\psi K^{*0}$ data is shown in figure 15 of appendix B.

6 The $K^+\pi^-\mu^+\mu^-$ and $K^+\pi^-$ mass distributions

The $K^+\pi^-\mu^+\mu^-$ invariant mass is used to discriminate between signal and background. The distribution of the signal candidates is modelled using the sum of two Gaussian functions with a common mean, each with a power-law tail on the low-mass side. The parameters describing the signal mass-shape are determined from a fit to the $B^0 \to J/\psi K^{*0}$ decay in the data, as shown in figure 3, and are subsequently fixed when fitting the $B^0 \to K^{*0}\mu^+\mu^-$ candidates. In samples of simulated $B^0 \to K^{*0}\mu^+\mu^-$ decays, the mass resolution is observed to vary with q^2 by 2–8%. A scale factor is therefore taken from the simulation and is used to correct the width of the Gaussian functions in the different q^2 bins. A component is included in the fit to account for $\overline{B}^0_s \to J/\psi K^{*0}$ decays, which are at a level of 0.8% of the $B^0 \to J/\psi K^{*0}$ signal yield [46]. However, the $\overline{B}^0_s \to K^{*0}\mu^+\mu^-$ decay is
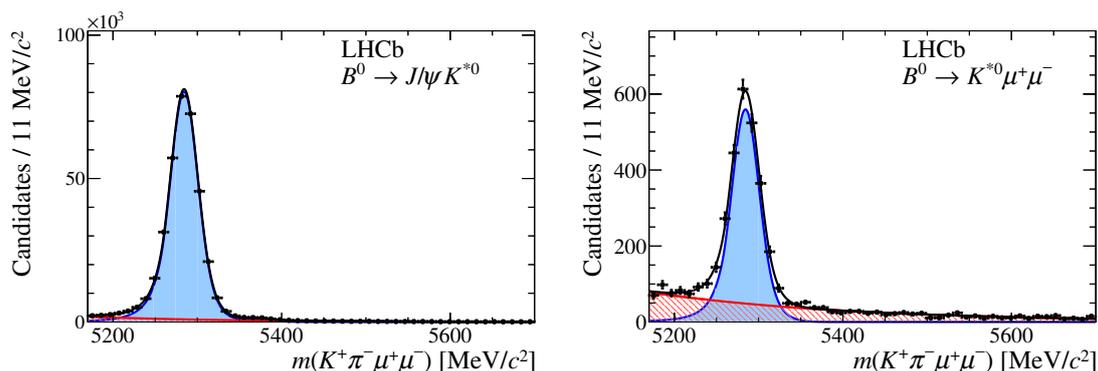
Figure 3. Invariant mass $m(K^+\pi^-\mu^+\mu^-)$ for (left) the control decay $B^0 \to J/\psi\, K^{*0}$ and (right) the signal decay $B^0 \to K^{*0}\mu^+\mu^-$, integrated over the full q^2 range (see text). Overlaid are the projections of the total fitted distribution (black line) and the signal and background components. The signal is shown by the blue shaded area and the background by the red hatched area.

neglected when fitting $B^0 \to K^{*0}\mu^+\mu^-$ candidates. Combinatorial background is described well by a single exponential distribution in $m(K^+\pi^-\mu^+\mu^-)$. The $B^0 \to K^{*0}\mu^+\mu^-$ signal yield integrated over the q^2 ranges $0.1 < q^2 < 8.0\,\mathrm{GeV}^2/c^4$, $11.0 < q^2 < 12.5\,\mathrm{GeV}^2/c^4$ and $15.0 < q^2 < 19.0\,\mathrm{GeV}^2/c^4$ is determined to be 2398 ± 57. The signal yield in the range $1.1 < q^2 < 6.0\,\mathrm{GeV}^2/c^4$ is 624 ± 30.

As detailed in sections 7.1 and 7.2, the likelihood fit and the method of moments use additional information from the $m(K^+\pi^-)$ distribution to constrain the fraction of $K^+\pi^-$ S-wave present in the data. To describe this distribution, the K^{*0} signal component is modelled using a relativistic Breit-Wigner function for the P-wave component and the LASS parameterisation [47] for the S-wave component. The combinatorial background is described by a linear function in $m(K^+\pi^-)$. There is no evidence for a K^{*0} component in the background $m(K^+\pi^-)$ distribution. When fitting for K^{*0} decay amplitudes, $m(K^+\pi^-)$ is integrated over, as detailed in section 7.3.

7 Angular analysis of the decay

The three methods used to determine the *CP*-averaged angular observables, *CP* asymmetries and the zero-crossing points of S_4, S_5 and A_{FB} are detailed below. Section 7.1 describes the determination of the observables in bins of q^2 using a maximum likelihood fit. Section 7.2 discusses the determination of the same set of observables using a principal moment analysis. Finally, section 7.3 describes a fit to the angular and q^2 distribution of the decay, parameterised in terms of the decay amplitudes rather than the observables. This fit is used to determine the zero-crossing points of S_4, S_5 and A_{FB}.

7.1 Determination of angular observables with a likelihood fit

In each q^2 bin, an unbinned maximum likelihood fit to $m(K^+\pi^-\mu^+\mu^-)$ and the three decay angles $\cos\theta_l$, $\cos\theta_K$ and ϕ is used to determine the angular observables introduced in section 2. The angular distribution of the signal is described using eq. (2.6). The

background angular distribution is modelled with second order polynomials in $\cos\theta_l$, $\cos\theta_K$ and ϕ, the parameters of which are left free in the fit. The angular distribution is assumed to factorise in the three decay angles. This assumption has been validated in the upper mass sideband.

In order to describe the signal angular distribution, the angular acceptance discussed in section 5 must be accounted for. The acceptance is treated in one of two ways, depending on the q^2 range being fitted. In the narrow q^2 bins, the acceptance is treated as being constant across each bin and is included in the fit by multiplying eq. (2.6) by the acceptance function evaluated at the bin centre. In the wider $1.1 < q^2 < 6.0\,\mathrm{GeV}^2/c^4$ and $15.0 < q^2 < 19.0\,\mathrm{GeV}^2/c^4$ bins, the shape of the acceptance can vary significantly across the bin. In this case, the candidates are weighted in the likelihood fit by the inverse of their efficiency. The event weights are scaled such that this pseudo-likelihood fit has confidence intervals with the correct coverage.

The $K^+\pi^-\mu^+\mu^-$ invariant mass is included in the fit to separate signal from background. The signal and background mass distributions are parameterised as described in section 6. In order to better constrain the S-wave fraction, a simultaneous fit of the $m(K^+\pi^-)$ distribution is performed using the parameterisation described in section 6. The signal fraction and F_S are common parameters in the simultaneous fits to the $m(K^+\pi^-)$ distribution and to the angular and $m(K^+\pi^-\mu^+\mu^-)$ distributions. Figure 4 shows the projections of the fitted probability density function on the angular and mass distributions for the $1.1 < q^2 < 6.0\,\mathrm{GeV}^2/c^4$ q^2 bin. Good agreement of the fitted function with the data is observed. Projections for the other q^2 bins are provided in appendix B.

The $P_i^{(\prime)}$ observables introduced in section 2 are determined by reparameterising eq. (2.4) using a basis comprising F_L, $P_{1,2,3}$ and $P'_{4,5,6,8}$. The CP asymmetries are determined by modifying the angular convention, introducing a relative sign between the angular terms $f_3(\vec{\Omega})$–$f_9(\vec{\Omega})$ for B^0 and $\overline{B}^0$ decays, such that eq. (2.4) is given in terms of F_L and the CP asymmetries A_3–A_9. The B^0 or $\overline{B}^0$ flavour is determined from the charge of the final-state kaon.

To ensure correct coverage for the uncertainties of the angular observables, the Feldman-Cousins method [48] is used with nuisance parameters treated according to the plug-in method [49]. Angular observables are considered one at a time, with the other angular observables treated as nuisance parameters. The nuisance parameters also include the signal fraction, the background parameters, F_S and the angular terms that arise from interference between the S- and P-wave.

7.2 Determination of angular observables using the method of moments

The angular observables are also determined using a principal moment analysis of the angular distribution, without making any angular fit to the data [25, 50]. As a continuous function of q^2, the moments are given by

$$M_i(q^2) = \int \left(\frac{1}{\mathrm{d}(\Gamma + \bar{\Gamma})/\mathrm{d}q^2} \right) \frac{\mathrm{d}^4(\Gamma + \bar{\Gamma})}{\mathrm{d}q^2\,\mathrm{d}\vec{\Omega}} f_i(\vec{\Omega})\mathrm{d}\vec{\Omega}\,. \tag{7.1}$$
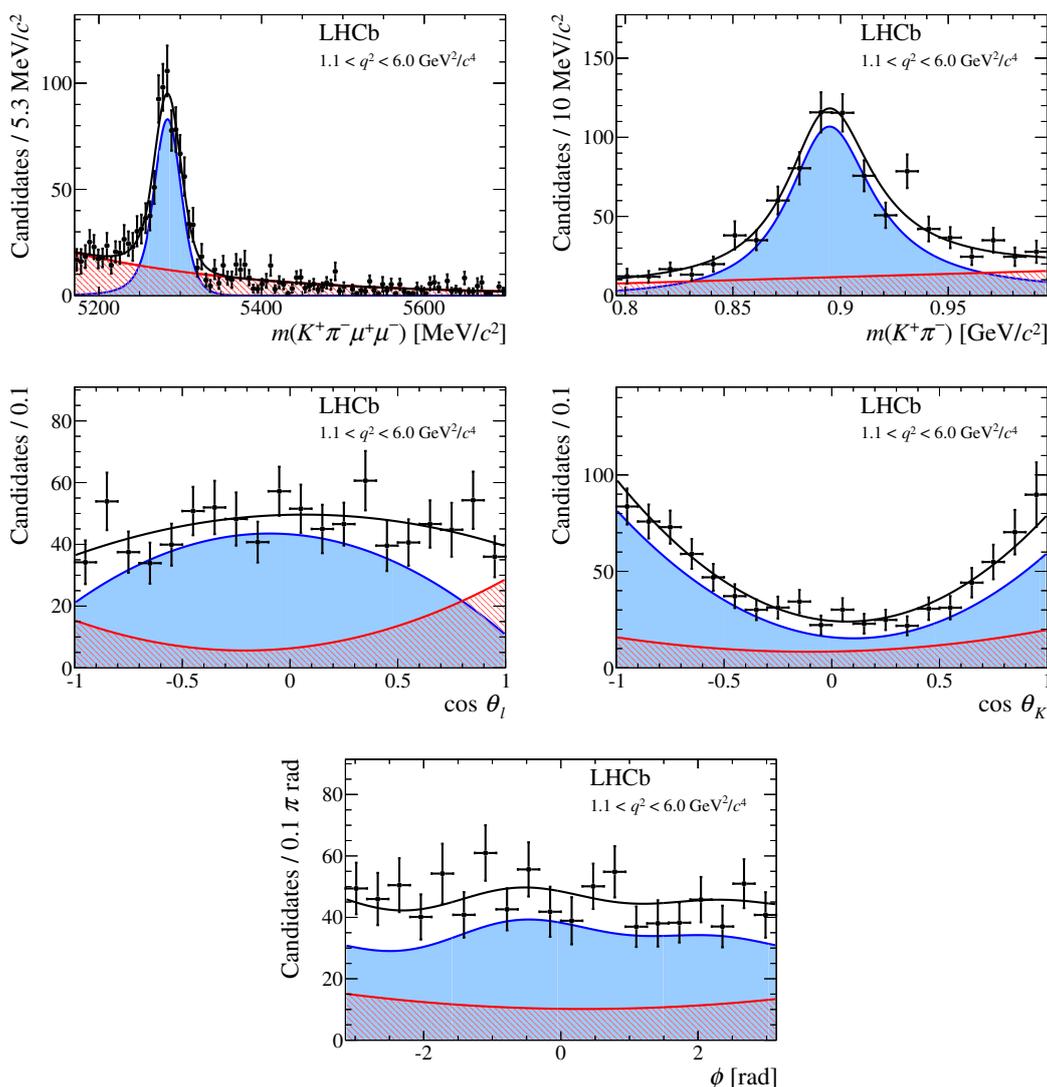
Figure 4. Angular and mass distributions for $1.1 < q^2 < 6.0\,\mathrm{GeV}^2/c^4$. The distributions of $m(K^+\pi^-)$ and the three decay angles are given for candidates in the signal mass window $\pm 50\,\mathrm{MeV}/c^2$ around the known B^0 mass. The candidates have been weighted to account for the acceptance. Overlaid are the projections of the total fitted distribution (black line) and its different components. The signal is shown by the blue shaded area and the background by the red hatched area.

The average $M_i(q^2)$ in a bin of q^2 is estimated by replacing the integral in eq. 7.1 with a sum over the candidates in the dataset. The angular acceptance is accounted for by weighting the candidates in the sum,

$$\widehat{M_i} = \frac{1}{\sum_e w_e} \sum_e w_e f_i(\vec{\Omega}_e)\,. \tag{7.2}$$

The sum is evaluated for candidates within $\pm 50\,\mathrm{MeV}/c^2$ of the B^0 mass. The weight, w_e, is the reciprocal of the candidate's efficiency and is computed as described in section 5. The mass window contains more than 95% of the signal candidates. This sum is also computed

for candidates with $5350 < m(K^+\pi^-\mu^+\mu^-) < 5700\,\mathrm{MeV}/c^2$ and the resulting value of $\widehat{M}_i$ is used to subtract the background contribution from the $\pm 50\,\mathrm{MeV}/c^2$ window. The functions f_i are given in table 1. Due to their dependence on the spherical harmonics, most of the angular terms are orthogonal. For $f_{i=3-9}$,

$$\int f_i(\vec{\Omega})f_j(\vec{\Omega})\mathrm{d}\vec{\Omega} = \lambda_i \delta_{ij}\,, \tag{7.3}$$

such that the moments give the CP-averaged observables S_3 to S_9 with a coefficient, λ_i, that takes into account the normalisation. In the limit of massless muons, the moments are related to the observables by the expressions

$$M_i = \begin{cases} \dfrac{8}{25}(1-F_{\mathrm{S}})S_i & \text{if} \quad i = 3,4,8,9, \\[2mm] \dfrac{2}{5}(1-F_{\mathrm{S}})S_i & \text{if} \quad i = 5,6s,7, \\[2mm] \dfrac{2}{5}(1-F_{\mathrm{S}})(2-F_{\mathrm{L}}) + \dfrac{2}{3}F_{\mathrm{S}} & \text{if} \quad i = 1s, \end{cases} \tag{7.4}$$

where, as noted previously, $A_{\mathrm{FB}} = \frac{3}{4}S_{6s}$. The relevant signal and background yields and the S-wave fraction F_{S} are determined from a two-dimensional extended unbinned maximum likelihood fit to the $m(K^+\pi^-\mu^+\mu^-)$ and $m(K^+\pi^-)$ distributions, using the shapes described in section 6.

The statistical uncertainties of the angular moments are estimated using a bootstrapping technique [51]. Confidence intervals are defined such that they include the 16th–84th percentiles of the bootstrap distribution of the observables. When computing the $P_i^{(\prime)}$ observables, bootstrapped data with unphysical F_{L} ($F_{\mathrm{L}} < 0$ or $F_{\mathrm{L}} > 1$) are added at $\pm\infty$ to ensure that the resulting intervals do not undercover. As in the likelihood method, the CP asymmetries are determined by flipping the sign of the relevant B^0 angular terms. The resulting moments are then used to determine the CP asymmetries by substituting A_i for S_i in eq. (7.4).

In the moment analysis, an additional angular observable that is not present in the massless limit is determined. This observable is sensitive to large new scalar or tensor contributions to the decay and is associated with a new forward-backward asymmetry of the dimuon system, $f_{6c}(\vec{\Omega}) = \cos^2\theta_K \cos\theta_l$ [22, 52]. The corresponding observable is highly correlated to A_{FB} but can be determined from the moments M_{6c} and M_{6s}, using $S_{6c} = 8M_{6c} - 2M_{6s}$.

7.3 Determination of zero-crossing points using the decay amplitudes

In the $1.1 < q^2 < 6.0\,\mathrm{GeV}^2/c^4$ region, it is also possible to determine the amplitudes $\mathcal{A}_{0,\parallel,\perp}^{\mathrm{L,R}}$, appearing in table 1, using a smoothly varying q^2-dependent parameterisation. For $q^2 \gtrsim 6.0\,\mathrm{GeV}^2/c^4$, resonant $c\bar{c}$ states make a simple parameterisation of the q^2-dependence impossible. A similar problem exists below $1.1\,\mathrm{GeV}^2/c^4$ due to the presence of light resonances.

The amplitudes $\mathcal{A}_{0,\parallel,\perp}^{\mathrm{L,R}}$ are complex functions of q^2 and therefore, at each point in q^2, the decay $B^0 \to K^{*0}\mu^+\mu^-$ is described by twelve real degrees of freedom. Several symmetries

leave the angular distribution of the final-state particles unchanged [53]. These symmetries allow four components of the amplitudes to be set to zero. This simplification results in eight independent degrees of freedom which completely describe the $B^0 \to K^{*0}\mu^+\mu^-$ decay. In this paper, the choice

$$\mathrm{Re}(\mathcal{A}_0^{\mathrm{R}}) = \mathrm{Im}(\mathcal{A}_0^{\mathrm{R}}) = \mathrm{Im}(\mathcal{A}_0^{\mathrm{L}}) = \mathrm{Im}(\mathcal{A}_\perp^{\mathrm{R}}) = 0 \qquad (7.5)$$

is made and the P-wave amplitudes are expressed using the form

$$\mathcal{A}_{i=0,\parallel,\perp}^{\mathrm{L,R}}(q^2) = \alpha_i^{\mathrm{L,R}} + \beta_i^{\mathrm{L,R}}q^2 + \frac{\gamma_i^{\mathrm{L,R}}}{q^2} \,, \qquad (7.6)$$

where $\alpha_i^{\mathrm{L,R}}$, $\beta_i^{\mathrm{L,R}}$ and $\gamma_i^{\mathrm{L,R}}$ are complex coefficients. The choice of which amplitude components to fix to zero and the form of the parameterisation are motivated in ref. [54].

In the q^2 range considered, the S-wave amplitudes are expected to vary slowly with q^2 [55]. To simplify the fit, these amplitudes are therefore assumed to be constant in q^2 and are described with a single complex parameter. The systematic uncertainty related to this approximation is negligible. After applying the symmetry constraints, the B^0 and $\overline{B}^0$ decays are each described by 24 real parameters for the P-wave amplitudes and four real parameters for the S-wave amplitudes. With the $3\,\mathrm{fb}^{-1}$ dataset, it is not possible to determine the parameters describing both the B^0 and $\overline{B}^0$ decays separately. It is therefore assumed that CP symmetry holds in the decay such that the amplitudes describing the B^0 and $\overline{B}^0$ decays are identical.

An unbinned maximum likelihood fit to the distributions of $m(K^+\pi^-\mu^+\mu^-)$, $\cos\theta_l$, $\cos\theta_K$, ϕ and q^2 is used to determine the amplitude parameters. The integral of the angular distribution is required to be consistent with the number of signal candidates in the fit. For simplicity, $m(K^+\pi^-)$ is not included in the fit. The variation of the amplitudes with $m(K^+\pi^-)$ is accounted for by replacing products of amplitudes $\mathcal{A}_i^{\mathrm{L,R}}\mathcal{A}_j^{*\,\mathrm{L,R}}$ with

$$\mathcal{A}_i^{\mathrm{L,R}}\mathcal{A}_j^{*\,\mathrm{L,R}} \int g_i(m(K^+\pi^-))g_j^*(m(K^+\pi^-))\mathrm{d}m(K^+\pi^-) \,, \qquad (7.7)$$

where $g_i(m(K^+\pi^-))$ describes the variation of the amplitude $\mathcal{A}_i^{\mathrm{L,R}}$ with $m(K^+\pi^-)$. The same models are used for the S- and P-wave lineshapes as in sections 7.1 and 7.2. The acceptance as a function of $\cos\theta_l$, $\cos\theta_K$, ϕ and q^2 (as described in section 5) is included in the amplitude fit. The combinatorial background is parameterised by a linear function in q^2. The background angular distribution is assumed to be independent of q^2 and is described by the product of three second-order polynomials. The background model and its factorisation in the decay angles and q^2 is checked using candidates in the $m(K^+\pi^-\mu^+\mu^-)$ sideband.

Figure 5 shows the projections of the fitted probability density functions on the angular and q^2 distributions of the candidates. In contrast to figure 4, the effect of the selection efficiency on the angles and q^2 is included in the signal distribution. The figure therefore shows the distribution of the candidates rather than the candidates weighted by the inverse of their selection efficiency. Good agreement of the fitted function and the data is observed.

The amplitude parameters are used to construct observables as continuous functions of q^2. The observables S_4, S_5 and A_{FB} have zero-crossing points and these are determined
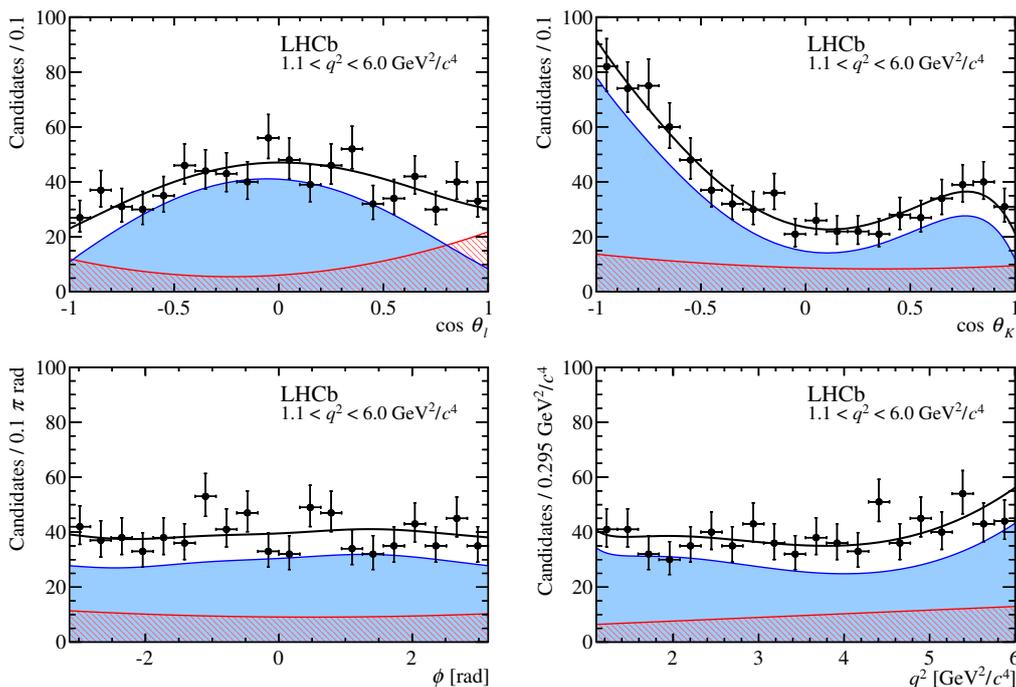
Figure 5. Angular and q^2 distribution of candidates overlaid by the result of the amplitude fit. The distribution of candidates in q^2 and the three decay angles is given in a $\pm 50\,\mathrm{MeV}/c^2$ window around the known B^0 mass. Overlaid are the projections of the total fitted distribution (black line) and its different components. The signal is shown by the blue shaded area and the background by the red hatched area.

by solving a quartic equation. The different solutions of this equation are separable based on the sign of the slope of the observable in the vicinity of the zero-crossing point. Only zero-crossing points in the range $1.1 < q^2 < 6.0\,\mathrm{GeV}^2/c^4$ with a local slope consistent with the data above $6.0\,\mathrm{GeV}^2/c^4$ are retained.

The large number of parameters floating in the fit, coupled with the limited number of signal candidates present in the dataset, results in a non-parabolic likelihood surface. Therefore, as in the determination of the angular moments, the statistical uncertainties of the q^2-dependent observables and their corresponding zero-crossing points are determined using a bootstrapping technique [51]. The statistical coverage of the resulting intervals is checked using simulated events and is found to be correct for the observables S_4, S_5 and A_{FB}. Despite the coverage being correct, approximately 10% of the bootstrapped datasets result in no zero-crossing point with the correct slope in the q^2 range $1.1 < q^2 < 6.0\,\mathrm{GeV}^2/c^4$. In these cases, the zero-crossing point is added to the bootstrap distribution at $\pm\infty$ to ensure that the method does not undercover. The determination of the q^2-dependent amplitudes in principle allows the full observable basis to be determined. However, pseudoexperiments indicate that a larger dataset is required in order to guarantee the correct coverage of the uncertainties on the observables other than S_4, S_5 and A_{FB}.

Source	F_{L}	S_3–S_9	A_3–A_9	P_1–P_8'	q_0^2 GeV$^2/c^4$
Acceptance stat. uncertainty	< 0.01	< 0.01	< 0.01	< 0.01	0.01
Acceptance polynomial order	< 0.01	< 0.02	< 0.02	< 0.04	0.01–0.03
Data-simulation differences	0.01–0.02	< 0.01	< 0.01	< 0.01	< 0.02
Acceptance variation with q^2	< 0.01	< 0.01	< 0.01	< 0.01	—
$m(K^+\pi^-)$ model	< 0.01	< 0.01	< 0.01	< 0.03	< 0.01
Background model	< 0.01	< 0.01	< 0.01	< 0.02	0.01–0.05
Peaking backgrounds	< 0.01	< 0.01	< 0.01	< 0.01	0.01–0.04
$m(K^+\pi^-\mu^+\mu^-)$ model	< 0.01	< 0.01	< 0.01	< 0.02	< 0.01
Det. and prod. asymmetries	—	—	< 0.01	< 0.02	—

Table 2. Summary of the different sources of systematic uncertainty on the angular observables. Upper limits or typical ranges are quoted for the different groups of observables. The column labelled q_0^2 corresponds to the zero-crossing points of S_4, S_5 and A_{FB}.

8   Systematic uncertainties

Effects that can alter the mass or angular distribution of either the signal or background candidates are sources of systematic uncertainty. The various sources of systematic uncertainty are discussed in detail below and are summarised in table 2. In general, the systematic uncertainties are significantly smaller than the statistical uncertainties.

The size of each systematic uncertainty is estimated using pseudoexperiments in which one or more parameters are varied. The angular observables are determined from these pseudoexperiments using the nominal model and the systematically varied model. For each observable, in each q^2 region, the systematic uncertainty is then taken as the average of the difference between the two models. The pseudoexperiments are generated with signal yields many times larger than that of the data, in order to render statistical fluctuations negligible.

The main systematic effects associated with the signal modelling arise from the estimate of the angular acceptance. Four separate sources of systematic uncertainty are considered: the statistical uncertainty on the acceptance correction resulting from the limited size of the simulation sample from which it is determined; an uncertainty associated with the parameterisation that is used to describe the acceptance function; an uncertainty arising from residual data-simulation differences; and, for the likelihood fit of the angular observables in narrow q^2 bins, an uncertainty associated with evaluating the acceptance at a fixed point in q^2.

The statistical uncertainty on the acceptance function is evaluated using pseudoexperiments that are generated by coherently fluctuating the acceptance parameters according to the covariance matrix for the angular moments of the acceptance function. To evaluate the uncertainty associated with the particular choice of order for the polynomials used to

describe the acceptance function, pseudoexperiments are produced in which the polynomial order is simultaneously increased by two in q^2 and in each of the angles.

After the B^0 momentum spectrum, detector occupancy and PID performance of the simulation are corrected to match the data, there is very good agreement between the properties of simulated and genuine $B^0 \to J/\psi K^{*0}$ decays. There are, however, some small remaining differences in the momentum and transverse momentum spectra of the reconstructed pion that can affect the determination of the acceptance correction. A new acceptance correction is derived after re-weighting the simulated phase-space sample to account for the observed differences. A more conservative variation has also been considered in which an acceptance correction is derived without any of the data-simulation corrections applied. The larger of the variations observed is added as a systematic uncertainty.

When determining the angular observables in the narrow q^2 bins with the maximum likelihood fit, the acceptance is evaluated using the q^2 value of the bin centre. Pseudoexperiments are generated to assess the bias generated by this choice, using instead the value of q^2 of the left- or right-hand bin boundary.

Possible contributions from the tails of higher mass K^* states in the $796 < m(K^+\pi^-) < 996\,\mathrm{MeV}/c^2$ window are also considered. Simulation studies indicate that any bias arising from these states is negligible compared to the statistical uncertainty on the angular observables.

For the background modelling, two sources of systematic uncertainty are considered. The first source is associated with the choice of second-order polynomials to model the background angular distribution in the fits of the angular observables and the q^2-dependent decay amplitudes. It is not possible to fit a more complex model to the data because of the small number of background candidates. Therefore, to test the model, the BDT requirement is relaxed and the background candidates are fitted with a fourth-order polynomial in each of the three angles. This shape is used when generating the pseudoexperiments. The second source is associated with the fit to the q^2-dependent decay amplitudes. In this case, the q^2 dependence of the background model is modified from a linear function to a third-order polynomial.

Systematic uncertainties are assessed for the different sources of peaking background that are neglected in the analysis. As detailed in section 4.1, the most important backgrounds are those from $\Lambda_b^0 \to pK^-\mu^+\mu^-$ and $B_s^0 \to \phi\mu^+\mu^-$ decays, where a kaon or proton is misidentified as pion; and $B^0 \to K^{*0}\mu^+\mu^-$ decays, where the kaon and pion are both misidentified. Taking the angular distribution of the background from simulated events, pseudoexperiments are generated with these backgrounds included, and the angular observables determined as if the background were not present. Pseudoexperiments are also generated in which the angular distribution of the $B_s^0 \to \phi\mu^+\mu^-$ and $\Lambda_b^0 \to pK^-\mu^+\mu^-$ decays are taken from data. These decays are selected by removing PID information from the BDT and inverting the background vetoes.

Systematic uncertainties are also assessed for the signal mass-modelling in $m(K^+\pi^-\mu^+\mu^-)$ and $m(K^+\pi^-)$. To assess the model of $m(K^+\pi^-\mu^+\mu^-)$, a fit is performed to $B^0 \to J/\psi K^{*0}$ data using the sum of two Gaussian distributions without the power law tails. To assess the modelling of $m(K^+\pi^-)$, pseudoexperiments are produced by systematically varying the S- and P-wave line-shape parameters. For the S-wave, the

LASS line-shape is also exchanged for the sum of resonant $K_0^*(800)^0$ (sometimes referred to as the κ resonance) and $K_0^*(1430)^0$ contributions.

For the fit to the q^2-dependent decay amplitudes, an additional uncertainty is assigned for the choice of the q^2 parameterisation of the S-wave components. As described in section 7.3, the S-wave amplitudes are taken to be constant in q^2. Motivated by ref. [55], a systematic variation is considered by assuming that the S-wave amplitudes $\mathcal{A}_{\mathrm{S}}^{\mathrm{L,R}}$ have the same q^2 dependence as the longitudinal P-wave amplitudes $\mathcal{A}_0^{\mathrm{L,R}}$.

The measured CP asymmetries can be biased due to detection and production asymmetries. The B^0 production asymmetry is measured to be less than 1% [56, 57]. The effect of this asymmetry is further suppressed due to B^0-$\overline{B}^0$ mixing. The kaon detection asymmetry was measured in ref. [58]. In contrast to the other sources of systematic uncertainty, the shift due to the detection and production asymmetries is calculated directly without generating pseudoexperiments. The systematic uncertainty on the angular observables A_i due to production and detection asymmetries is found to be less than 0.01. The effect of these asymmetries on the CP-averaged observables is negligible.

In the q^2-bin $0.10 < q^2 < 0.98\,\mathrm{GeV}^2/c^4$, the muon mass-squared is comparable to q^2 and the relations between $S_{1(s,c)}$, $S_{2(s,c)}$ and F_{L} (see section 2) are only approximate. The assumption that these relations hold has no impact on the measured values of S_3–S_9 or A_3–A_9 but results in a biased estimate of F_{L} and hence of the $P_i^{(\prime)}$ observables. In pseudoexperiments based on the SM, this bias is typically at the level of 0.02. This can be accounted for in the SM predictions for this q^2-bin and hence is not considered as a source of systematic uncertainty.

For F_{L} and A_{FB}, the largest source of systematic uncertainty comes from the data-simulation comparison of the pion momenta. The systematic uncertainty assigned to this effect is at the level of $0.01 - 0.02$, depending on the q^2 bin. This uncertainty constitutes up to 30% of the statistical uncertainty on F_{L} and 20% of the statistical uncertainty on A_{FB}. For S_5 and A_5, the largest source of systematic uncertainty comes from the choice of polynomial order for the angular acceptance. If polynomials two orders higher are used, a variation of ~ 0.01 is observed. For the remaining CP-averaged and CP-asymmetric observables, the uncertainties arising from the data-simulation comparison and the acceptance are small. However, there are three other non-negligible sources of systematic uncertainty. Throughout the full q^2 range, peaking backgrounds introduce a systematic uncertainty at the level of 0.01 or less. For the likelihood fit of the angular observables, in the first two q^2 bins (where the acceptance changes most rapidly), the uncertainty arising from using the bin centre, as opposed to a bin edge, is at the level of 0.01 or less. Finally, at high q^2, the statistical precision on the acceptance correction leads to a systematic uncertainty at the level of 0.01 or less. For the $P_i^{(\prime)}$ observables, the situation is more complex and the systematic uncertainty is shared more evenly between the different sources (see table 2). The dominant sources of systematic uncertainty can all be reduced in future analyses with larger datasets.

Propagating the above sources of systematic uncertainty to the zero-crossing points yields uncertainties at the level of $0.07\,\mathrm{GeV}^2/c^4$ for S_4, $0.02\,\mathrm{GeV}^2/c^4$ for S_5 and $0.03\,\mathrm{GeV}^2/c^4$ for A_{FB}. These uncertainties are negligible compared to the statistical uncertainties.

9   Results

The *CP*-averaged observables that are obtained from the likelihood fits are shown together with the SM predictions in figure 6. The *CP* asymmetries are shown in figure 7. The SM predictions are based on the prescription of ref. [19]. In contrast to the alternative SM predictions that are available in refs. [20, 59–64], these predictions update the calculations from ref. [65] to account for the known correlation between the different form factors [66]. Light-cone sum rule predictions, which are valid in the low-q^2 region, are also combined with lattice determinations at high q^2 [67, 68] to yield more precise determinations of the form factors over the full q^2 range. The predictions are made in the regions $0.1 < q^2 < 6.0\,\text{GeV}^2/c^4$ and $15.0 < q^2 < 19.0\,\text{GeV}^2/c^4$. No predictions are made for the region close to the narrow $c\bar{c}$ resonances, the J/ψ and $\psi(2S)$, where many of the assumptions that go into the SM predictions are thought to be invalid. Reference [19] does not make predictions for the $S_{7,8,9}$ and the A_i observables. These observables are all expected to be close to zero in the SM.

The results of the fits for the optimised angular observables are shown together with their SM predictions in figure 8. For the $P_i^{(\prime)}$ observables, predictions from ref. [14] are shown using form factors from ref. [69]. The SM predictions are restricted to the q^2 range $q^2 < 8.0\,\text{GeV}^2/c^4$. The variation in the size of the uncertainties on the $P_i^{(\prime)}$ observables arises from their dependence on $F_{\rm L}$. When $F_{\rm L}$ is large, the $(1 - F_{\rm L})$ term in the definition of the observables gives a large uncertainty that can be significantly asymmetric.

The results of the likelihood fit for the angular observables are given in tables 3–6 of appendix A, with the statistical and systematic uncertainties separated. In general, the correlations between the observables are small. The most notable exceptions are the correlations between $A_{\rm FB}$ and $F_{\rm L}$, which can be as large as 60%, and the correlations between the different $P_i^{(\prime)}$ observables in the range $2.5 < q^2 < 4.0\,\text{GeV}^2/c^4$. The correlations between $A_{\rm FB}$ and $F_{\rm L}$ arise from the requirement that the differential decay rate in eq. (2.4) be positive across the entire phase space. The correlations between the $P_i^{(\prime)}$ observables originate from their common dependence on $F_{\rm L}$. The correlation matrices for all of the q^2 bins are available in appendices C, D and E. The values of $F_{\rm S}$ obtained from the fits are consistent with the S-wave contribution of approximately 5% observed in $B^0 \to J/\psi K^{*0}$ data [43–45]. Considering the observables individually, the results appear largely in agreement with the SM predictions. The exception to this is the observable S_5 and the related observable P_5'. Small differences can also be seen in the measured $A_{\rm FB}$ distribution, where the data lie systematically below the SM predictions in the range $1.1 < q^2 < 6.0\,\text{GeV}^2/c^4$. No significant *CP* asymmetry is seen.

The discrepancy in P_5' confirms the result of the previous LHCb analysis [8], where a difference was seen between the data and the SM predictions in the q^2 range $4.30 < q^2 < 8.68\,\text{GeV}^2/c^4$. In the present analysis, a deviation from the SM prediction is observed in each of the $4.0 < q^2 < 6.0\,\text{GeV}^2/c^4$ and $6.0 < q^2 < 8.0\,\text{GeV}^2/c^4$ bins at a level of 2.8 and 3.0 standard deviations, respectively. The SM predictions for the optimised observables that are used in this analysis are taken from ref. [14]. The predictions are an update of the SM calculation from ref. [70], which was used to compare the previous LHCb $P_i^{(\prime)}$ measurements to the SM.
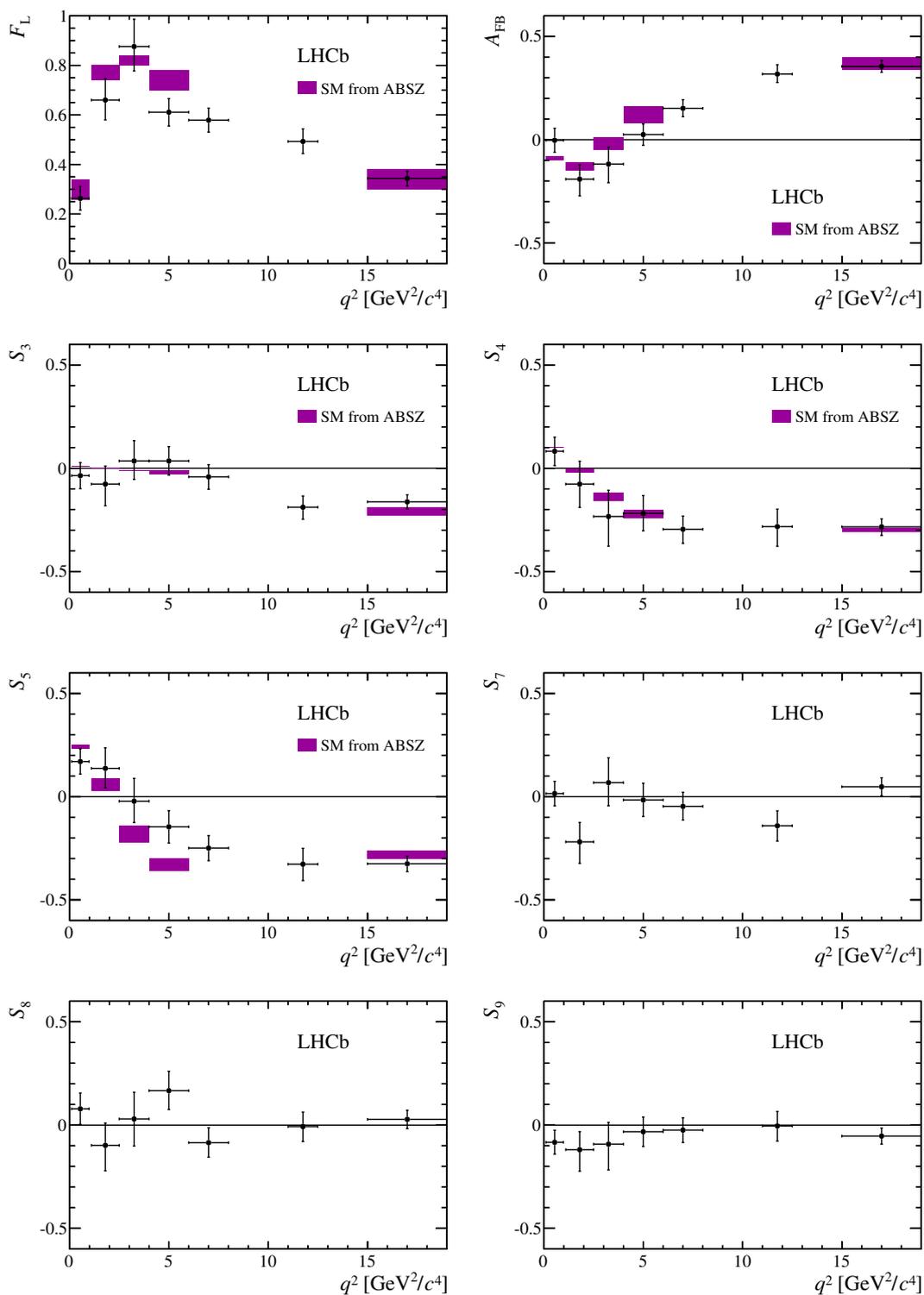
Figure 6. The *CP*-averaged observables in bins of q^2, determined from a maximum likelihood fit to the data. The shaded boxes show the SM predictions based on the prescription of ref. [19].
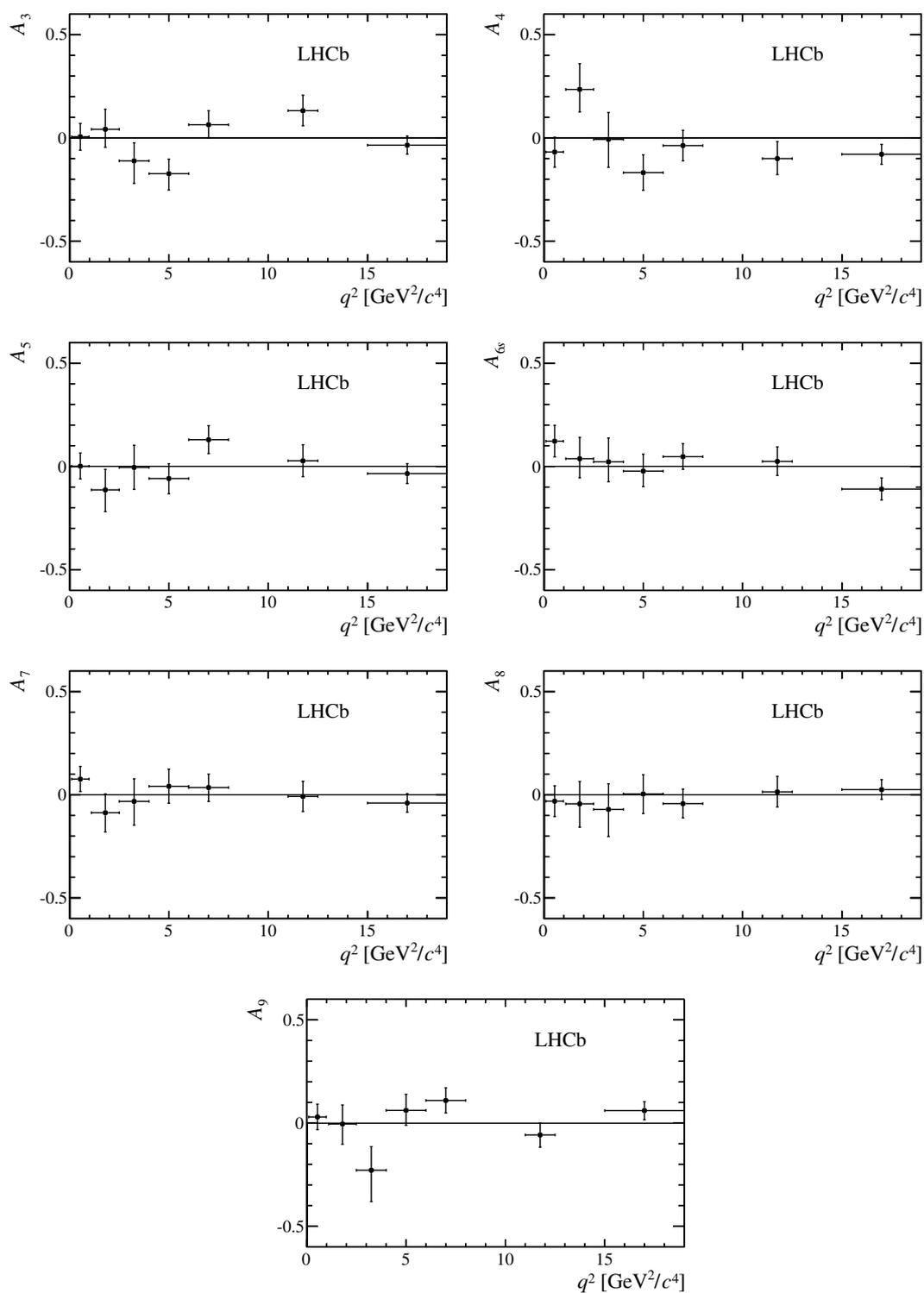
Figure 7. The *CP*-asymmetric observables in bins of q^2, determined from a maximum likelihood fit to the data.
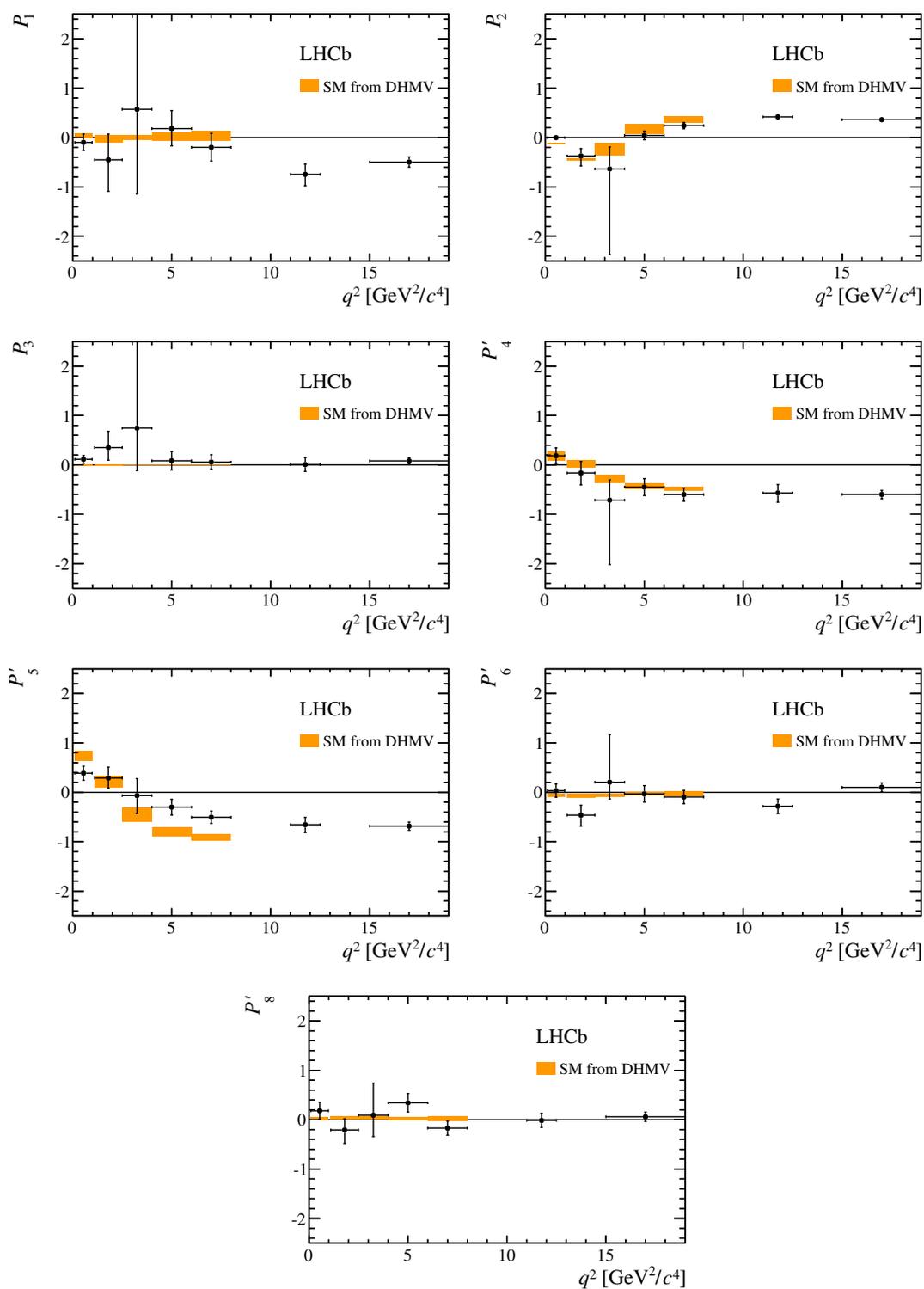
Figure 8. The optimised angular observables in bins of q^2, determined from a maximum likelihood fit to the data. The shaded boxes show the SM prediction taken from ref. [14].
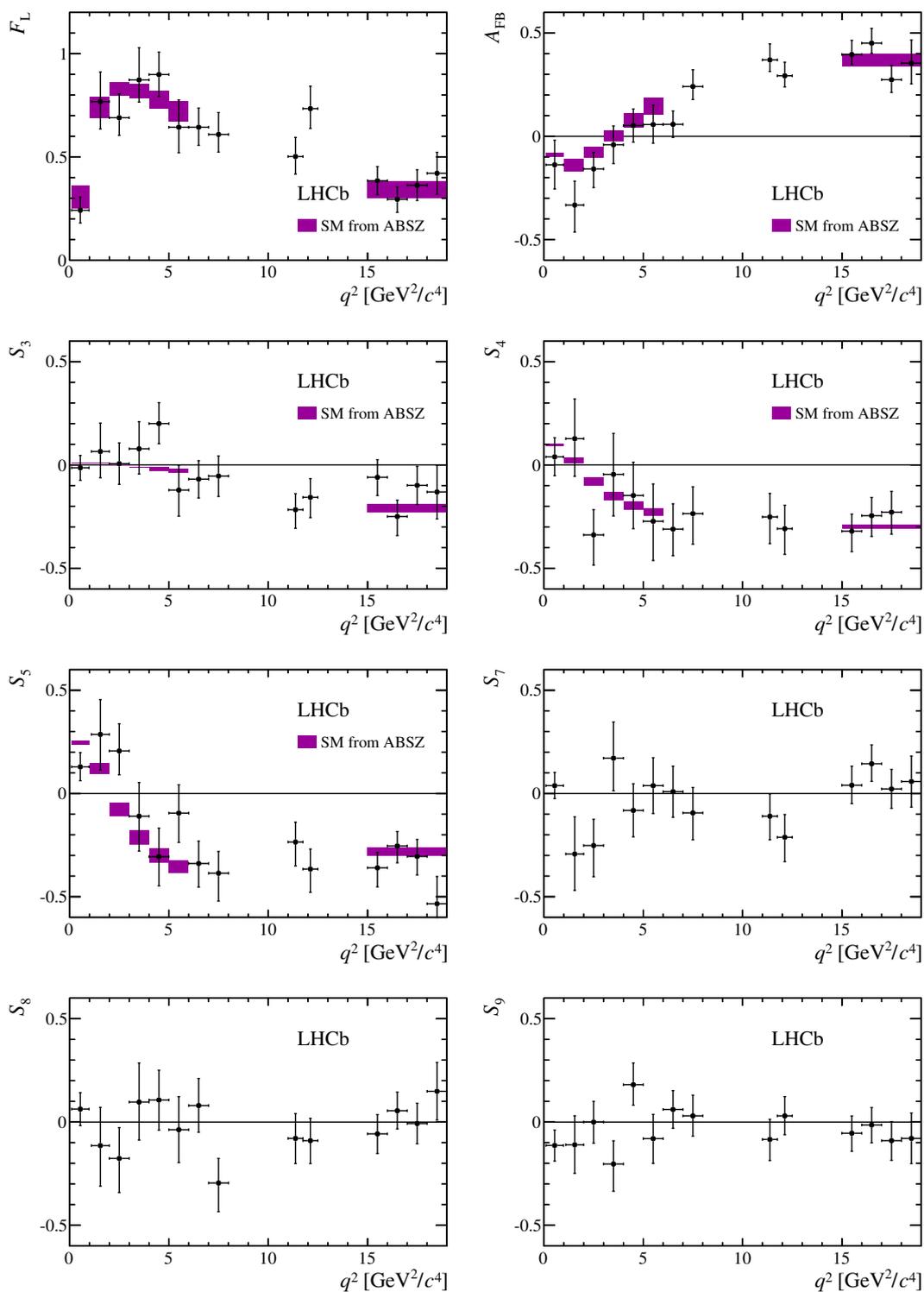
Figure 9. The *CP*-averaged observables in bins of q^2, determined from a moment analysis of the data. The shaded boxes show the SM predictions based on the prescription of ref. [19].
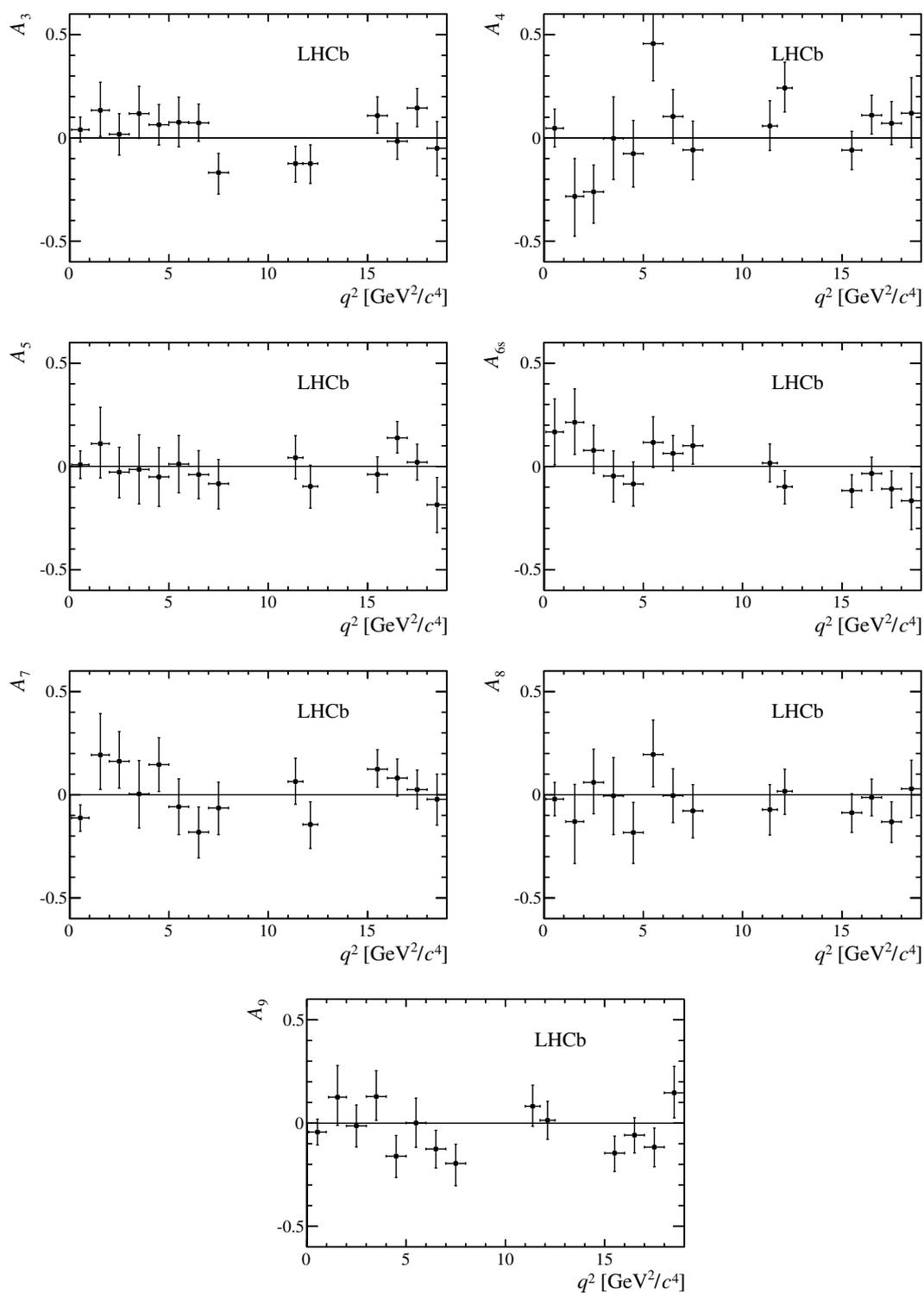
Figure 10. The *CP*-asymmetric observables in bins of q^2, determined from a moment analysis of the data.
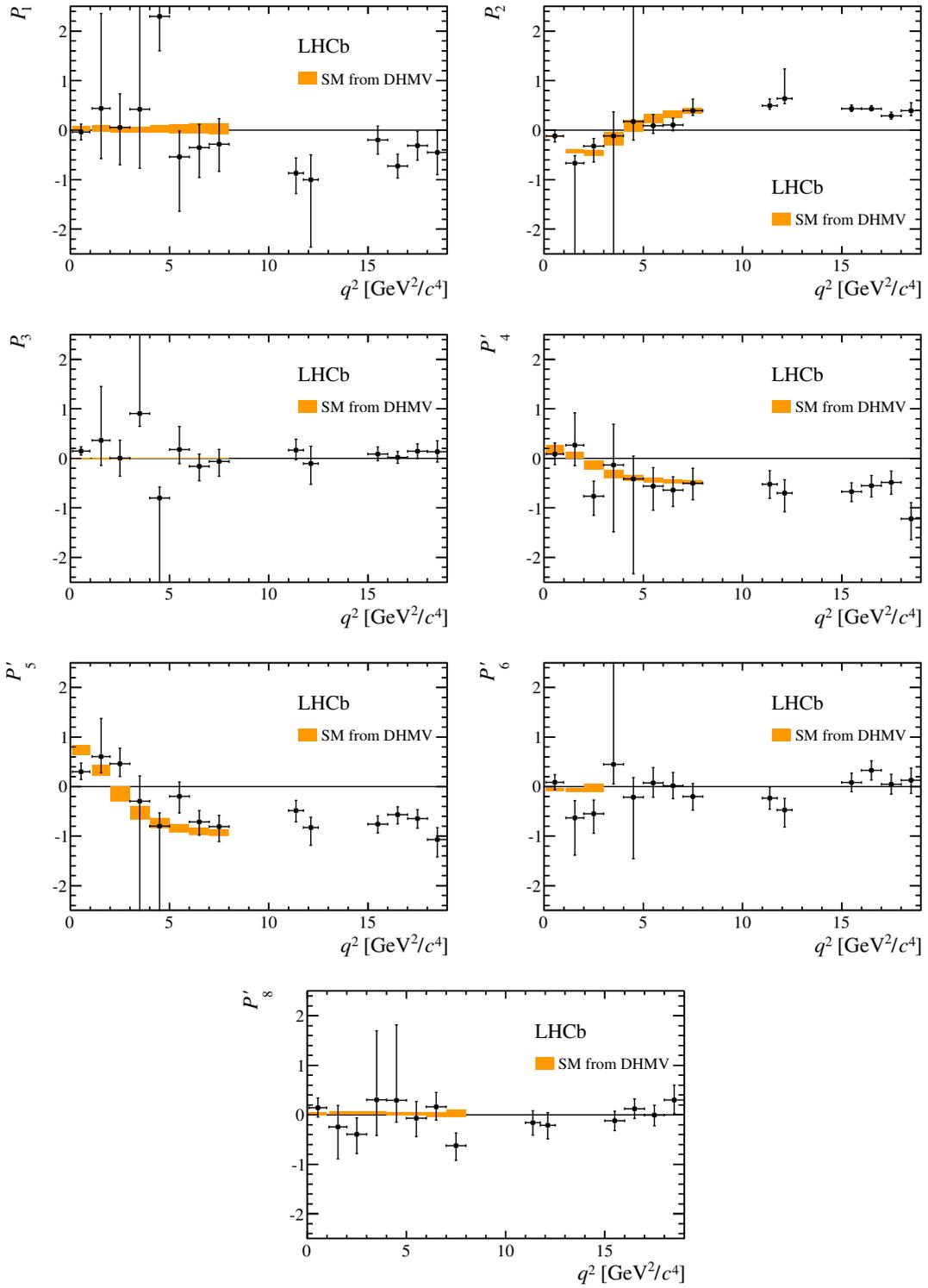
Figure 11. The optimised angular observables in bins of q^2, determined from a moment analysis of the data. The shaded boxes show the SM predictions taken from ref. [14].
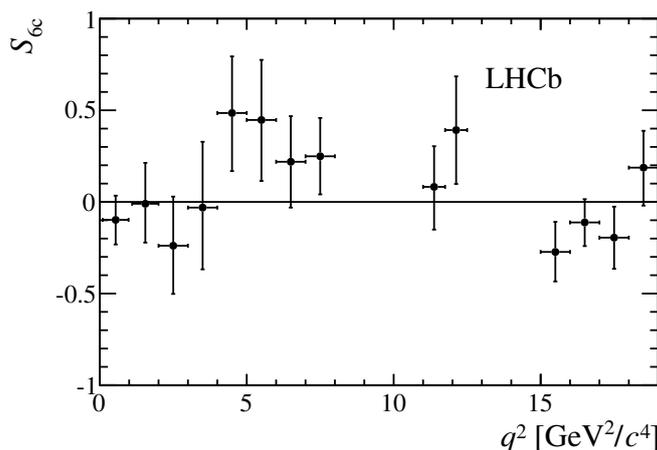
Figure 12. The observable S_{6c} in bins of q^2, as determined from a moment analysis of the data.

The results of the moment analysis are shown in figures 9, 10 and 11 and given in tables 7, 8 and 9 of appendix A. The same behaviour is seen as in the likelihood fit, where some differences are observed between the SM predictions and the data in S_5 (and P_5') at low values of q^2. The observable S_{6c} is also included in table 7 and shown in figure 12.

This observable is consistent with zero, as expected in the SM. As a cross-check, the observables have also been determined by a moment analysis in the approximately $2\,\mathrm{GeV}^2/c^4$ q^2 bins used in the likelihood fit of the angular observables. The differences between the central values of the two methods are compatible with those expected from pseudoexperiments. The correlation matrices for all of the q^2 bins are available in appendices F–H.

Figure 13 shows the observables S_4, S_5 and A_{FB} resulting from the fit to the q^2-dependent decay amplitudes. The results are in agreement with those obtained from the likelihood fit of the angular observables and the moments analysis. For A_{FB}, the best-fit to the data (the line in the figure) has two zero-crossing points in the range $1.1 < q^2 < 6.0\,\mathrm{GeV}^2/c^4$ with different slopes. As discussed in section 7.3, only the solution consistent with the data in the range $q^2 > 6.0\,\mathrm{GeV}^2/c^4$ is cited, *i.e.* the solution with the positive slope (see figures 6 and 9). The zero-crossing points determined from the amplitude fit are

$$q_0^2(S_5) \in [2.49, 3.95]\,\mathrm{GeV}^2/c^4 \text{ at } 68\% \text{ confidence level (C.L.)}\,,$$

$$q_0^2(A_{\mathrm{FB}}) \in [3.40, 4.87]\,\mathrm{GeV}^2/c^4 \text{ at } 68\% \text{ C.L.}\,.$$

It is not possible to determine if S_4 has a zero-crossing point at 68% confidence level. If there is a zero-crossing then

$$q_0^2(S_4) < 2.65\,\mathrm{GeV}^2/c^4 \text{ at } 95\% \text{ C.L.}\,.$$

The correlations between the measured values are less than 10%. The measured zero-crossing points are all consistent with their respective SM expectations. Standard Model predictions for $q_0^2(A_{\mathrm{FB}})$ are typically in the range $3.9-4.4\,\mathrm{GeV}^2/c^4$ [71–73] and have relative uncertainties below the 10% level, for example, $q_0^2(A_{\mathrm{FB}}) = 4.36\,^{+0.33}_{-0.31}\,\mathrm{GeV}^2/c^4$ [72].
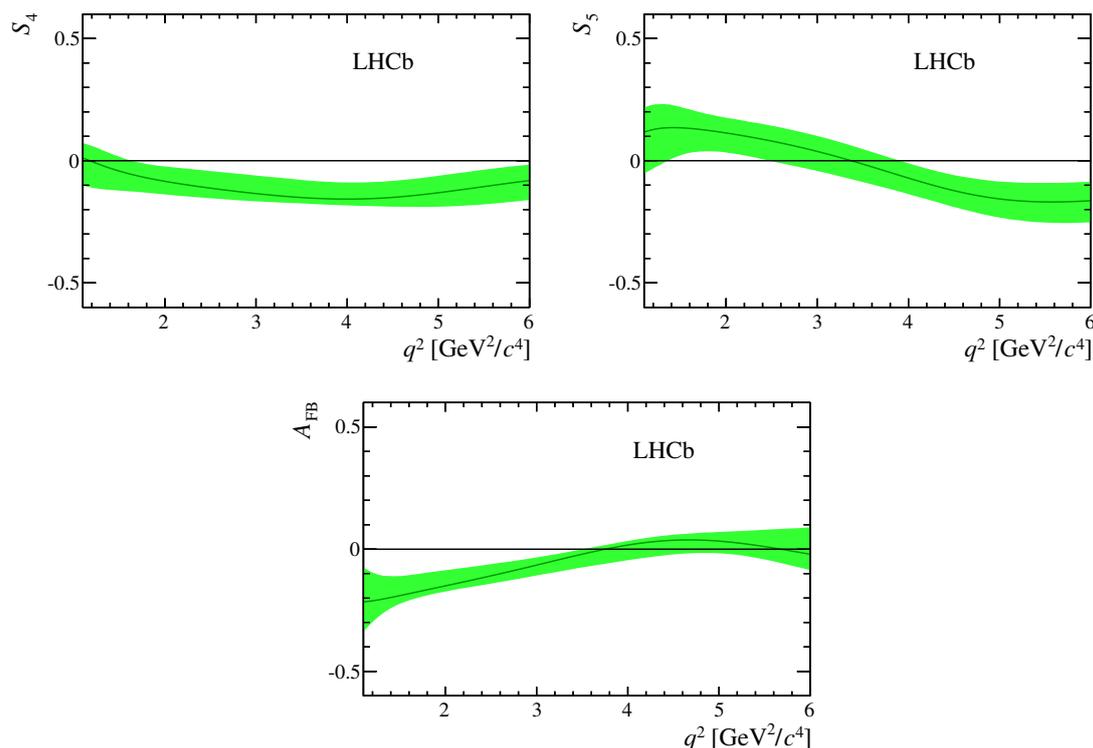
Figure 13. The observables S_4, S_5 and A_{FB} determined by fitting for the q^2 dependent decay amplitudes. The line indicates the best-fit to the dataset. The band indicates the 68% interval on the bootstraps at each point in q^2. Note that, the correlation between points in the bands means it is not possible to extract the uncertainty on the zero-crossing points from these figures.

10 Compatibility with the Standard Model

The EOS software package [59] is used to determine the level of compatibility of the data with the SM. It provides predictions for the observables integrated over the q^2 bins used in the analysis. A χ^2 fit is performed to the CP-averaged angular observables F_L, A_{FB} and S_3–S_9 obtained from the likelihood fit to the data. The χ^2 fit uses observables in the range $q^2 < 8.0\,\mathrm{GeV}^2/c^4$ and a wide q^2 bin covering the range $15.0 < q^2 < 19.0\,\mathrm{GeV}^2/c^4$. Previous analyses [9–12, 19–21] have shown that the existing measurements of decays involving a $b \to s$ quark transition, including the previous LHCb P_5' result from ref. [8], can be accounted for by modifying only the real part of the vector coupling strength of the decays, conventionally denoted $\mathrm{Re}(\mathcal{C}_9)$. An analysis considering additional effective couplings would require a global fit to all of the measurements of $b \to s$ quark transitions and is beyond the scope of this paper. Note that modifying just the axial-vector coupling strength, $\mathcal{C}_{10}$, would lead to a branching fraction for the $B_s^0 \to \mu^+\mu^-$ decay that is excluded by existing measurements [74].

In the χ^2 fit, the correlations between the different observables are taken into account. The floating parameters are $\mathrm{Re}(\mathcal{C}_9)$ and a number of nuisance parameters associated with the form factors, CKM elements and possible sub-leading corrections to the amplitudes.
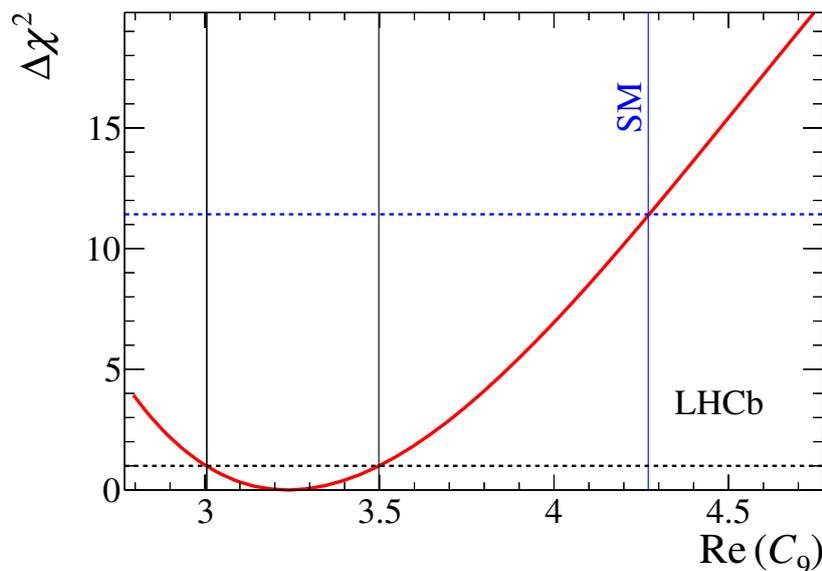
Figure 14. The $\Delta\chi^2$ distribution for the real part of the generalised vector-coupling strength, $\mathcal{C}_9$. This is determined from a fit to the results of the maximum likelihood fit of the *CP*-averaged observables. The SM central value is $\mathrm{Re}(\mathcal{C}_9^{\mathrm{SM}}) = 4.27$ [11]. The best fit point is found to be at $\Delta\mathrm{Re}(\mathcal{C}_9) = -1.04 \pm 0.25$.

The sub-leading corrections to the amplitudes are expected to be suppressed by the size of the *b*-quark mass relative to the typical energy scale of QCD. The nuisance parameters are treated according to the prescription of ref. [11] and are included in the fit with Gaussian constraints. In the χ^2 minimisation procedure, the value of each observable (as derived from a particular choice of the theory parameters) is compared to the measured value. Depending on the sign of the difference between these values, either the lower or upper (asymmetric) uncertainty on the measurement is used to compute the χ^2.

The minimum χ^2 corresponds to a value of $\mathrm{Re}(\mathcal{C}_9)$ shifted by $\Delta\mathrm{Re}(\mathcal{C}_9) = -1.04 \pm 0.25$ from the SM central value of $\mathrm{Re}(\mathcal{C}_9) = 4.27$ [11] (see figure 14). From the difference in χ^2 between the SM point and this best-fit point, the significance of this shift corresponds to 3.4 standard deviations. As discussed in the literature [9–12, 14–21], a shift in $\mathcal{C}_9$ could be caused by a contribution from a new vector particle or could result from an unexpectedly large hadronic effect.

If a fit is instead performed to the *CP*-averaged observables from the moment analysis in the same q^2 ranges, then $\Delta\mathrm{Re}(\mathcal{C}_9) = -0.68 \pm 0.35$ is obtained. As expected, the uncertainty on $\Delta\mathrm{Re}(\mathcal{C}_9)$ is larger than that from the likelihood fit. Taking into account the correlations between the two methods, the values of $\Delta\mathrm{Re}(\mathcal{C}_9)$ are statistically compatible.

11 Conclusions

This paper presents the first analysis of the full angular distribution of the $B^0 \to K^{*0}\mu^+\mu^-$ decay. The analysis uses the complete LHCb Run 1 dataset and supersedes the results

presented in refs. [1, 8]. In addition to *CP*-averaged observables, a complete set of *CP* asymmetries of the angular distribution are measured for the first time. Correlations between the different observables are computed to allow the results to be included in global fits of $b \to s$ data.

Three separate techniques are used to analyse the data. An unbinned maximum likelihood fit to the full angular distribution is made in approximately $2\,\mathrm{GeV}^2/c^4$ wide q^2 bins. Observables are also determined by computing moments of the angular distribution in q^2 bins approximately $1\,\mathrm{GeV}^2/c^4$ wide. In addition, for the first time, a q^2-dependent fit is performed to the angular distribution in order to determine the six complex decay amplitudes that describe the decay. The position in q^2 at which several observables cross zero is determined using these amplitudes.

A global analysis of the *CP*-averaged angular observables determined from the maximum likelihood fit indicates differences with the presently-available SM predictions at the level of 3.4 standard deviations. These differences could be explained by an unexpectedly large hadronic effect that changes the SM predictions [15, 19]. The differences could also be explained by contributions to the decay from non-SM particles [9–12, 14–21].

Acknowledgments

A Tables of results

The results of the likelihood fits described in section 7.1 are given in tables 3–6 below. The results of the method of moments described in section 7.2 are given in tables 7–9 below.

	$1.1 < q^2 < 6.0\,\mathrm{GeV}^2/c^4$	$15.0 < q^2 < 19.0\,\mathrm{GeV}^2/c^4$
F_{L}	$0.690\,^{+0.035}_{-0.036} \pm 0.017$	$0.344\,^{+0.028}_{-0.030} \pm 0.008$
S_3	$0.012\,^{+0.038}_{-0.038} \pm 0.004$	$-0.163\,^{+0.033}_{-0.033} \pm 0.009$
S_4	$-0.155\,^{+0.057}_{-0.056} \pm 0.004$	$-0.284\,^{+0.038}_{-0.041} \pm 0.007$
S_5	$-0.023\,^{+0.050}_{-0.049} \pm 0.005$	$-0.325\,^{+0.036}_{-0.037} \pm 0.009$
A_{FB}	$-0.075\,^{+0.032}_{-0.034} \pm 0.007$	$0.355\,^{+0.027}_{-0.027} \pm 0.009$
S_7	$-0.077\,^{+0.050}_{-0.049} \pm 0.006$	$0.048\,^{+0.043}_{-0.043} \pm 0.006$
S_8	$0.028\,^{+0.058}_{-0.057} \pm 0.008$	$0.028\,^{+0.044}_{-0.045} \pm 0.003$
S_9	$-0.064\,^{+0.042}_{-0.041} \pm 0.004$	$-0.053\,^{+0.039}_{-0.039} \pm 0.002$
P_1	$0.080\,^{+0.248}_{-0.245} \pm 0.044$	$-0.497\,^{+0.102}_{-0.099} \pm 0.027$
P_2	$-0.162\,^{+0.072}_{-0.073} \pm 0.010$	$0.361\,^{+0.025}_{-0.026} \pm 0.010$
P_3	$0.205\,^{+0.135}_{-0.134} \pm 0.017$	$0.081\,^{+0.060}_{-0.059} \pm 0.005$
P_4'	$-0.336\,^{+0.124}_{-0.122} \pm 0.012$	$-0.597\,^{+0.080}_{-0.085} \pm 0.015$
P_5'	$-0.049\,^{+0.107}_{-0.108} \pm 0.014$	$-0.684\,^{+0.078}_{-0.081} \pm 0.020$
P_6'	$-0.166\,^{+0.108}_{-0.108} \pm 0.021$	$0.101\,^{+0.090}_{-0.092} \pm 0.011$
P_8'	$0.060\,^{+0.122}_{-0.124} \pm 0.009$	$0.059\,^{+0.094}_{-0.093} \pm 0.008$
A_3	$-0.072\,^{+0.038}_{-0.038} \pm 0.004$	$-0.035\,^{+0.043}_{-0.042} \pm 0.010$
A_4	$0.012\,^{+0.057}_{-0.056} \pm 0.005$	$-0.079\,^{+0.047}_{-0.048} \pm 0.008$
A_5	$-0.044\,^{+0.049}_{-0.047} \pm 0.005$	$-0.035\,^{+0.047}_{-0.047} \pm 0.010$
A_6	$0.020\,^{+0.061}_{-0.060} \pm 0.009$	$-0.110\,^{+0.052}_{-0.051} \pm 0.013$
A_7	$-0.045\,^{+0.050}_{-0.050} \pm 0.006$	$-0.040\,^{+0.045}_{-0.044} \pm 0.006$
A_8	$-0.047\,^{+0.058}_{-0.057} \pm 0.008$	$0.025\,^{+0.048}_{-0.047} \pm 0.003$
A_9	$-0.033\,^{+0.040}_{-0.042} \pm 0.004$	$0.061\,^{+0.043}_{-0.044} \pm 0.002$

Table 3. CP-averaged angular observables evaluated by the unbinned maximum likelihood fit, in the range $1.1 < q^2 < 6.0\,\mathrm{GeV}^2/c^4$ and $15.0 < q^2 < 19.0\,\mathrm{GeV}^2/c^4$. The first uncertainties are statistical and the second systematic.

	$0.10 < q^2 < 0.98 \, \text{GeV}^2/c^4$	$1.1 < q^2 < 2.5 \, \text{GeV}^2/c^4$	$2.5 < q^2 < 4.0 \, \text{GeV}^2/c^4$
F_{L}	$0.263 \, ^{+0.045}_{-0.044} \pm 0.017$	$0.660 \, ^{+0.083}_{-0.077} \pm 0.022$	$0.876 \, ^{+0.109}_{-0.097} \pm 0.017$
S_3	$-0.036 \, ^{+0.063}_{-0.063} \pm 0.005$	$-0.077 \, ^{+0.087}_{-0.105} \pm 0.005$	$0.035 \, ^{+0.098}_{-0.089} \pm 0.007$
S_4	$0.082 \, ^{+0.068}_{-0.069} \pm 0.009$	$-0.077 \, ^{+0.111}_{-0.113} \pm 0.005$	$-0.234 \, ^{+0.127}_{-0.144} \pm 0.006$
S_5	$0.170 \, ^{+0.059}_{-0.058} \pm 0.018$	$0.137 \, ^{+0.099}_{-0.094} \pm 0.009$	$-0.022 \, ^{+0.110}_{-0.103} \pm 0.008$
A_{FB}	$-0.003 \, ^{+0.058}_{-0.057} \pm 0.009$	$-0.191 \, ^{+0.068}_{-0.080} \pm 0.012$	$-0.118 \, ^{+0.082}_{-0.090} \pm 0.007$
S_7	$0.015 \, ^{+0.059}_{-0.059} \pm 0.006$	$-0.219 \, ^{+0.094}_{-0.104} \pm 0.004$	$0.068 \, ^{+0.120}_{-0.112} \pm 0.005$
S_8	$0.079 \, ^{+0.076}_{-0.075} \pm 0.007$	$-0.098 \, ^{+0.108}_{-0.123} \pm 0.005$	$0.030 \, ^{+0.129}_{-0.131} \pm 0.006$
S_9	$-0.083 \, ^{+0.058}_{-0.057} \pm 0.004$	$-0.119 \, ^{+0.087}_{-0.104} \pm 0.005$	$-0.092 \, ^{+0.105}_{-0.125} \pm 0.007$

	$4.0 < q^2 < 6.0 \, \text{GeV}^2/c^4$	$6.0 < q^2 < 8.0 \, \text{GeV}^2/c^4$	$11.0 < q^2 < 12.5 \, \text{GeV}^2/c^4$
F_{L}	$0.611 \, ^{+0.052}_{-0.053} \pm 0.017$	$0.579 \, ^{+0.046}_{-0.046} \pm 0.015$	$0.493 \, ^{+0.049}_{-0.047} \pm 0.013$
S_3	$0.035 \, ^{+0.069}_{-0.068} \pm 0.007$	$-0.042 \, ^{+0.058}_{-0.059} \pm 0.011$	$-0.189 \, ^{+0.054}_{-0.058} \pm 0.005$
S_4	$-0.219 \, ^{+0.086}_{-0.084} \pm 0.008$	$-0.296 \, ^{+0.063}_{-0.067} \pm 0.011$	$-0.283 \, ^{+0.084}_{-0.095} \pm 0.009$
S_5	$-0.146 \, ^{+0.077}_{-0.078} \pm 0.011$	$-0.249 \, ^{+0.059}_{-0.060} \pm 0.012$	$-0.327 \, ^{+0.076}_{-0.079} \pm 0.009$
A_{FB}	$0.025 \, ^{+0.051}_{-0.052} \pm 0.004$	$0.152 \, ^{+0.041}_{-0.040} \pm 0.008$	$0.318 \, ^{+0.044}_{-0.040} \pm 0.009$
S_7	$-0.016 \, ^{+0.081}_{-0.080} \pm 0.004$	$-0.047 \, ^{+0.068}_{-0.066} \pm 0.003$	$-0.141 \, ^{+0.072}_{-0.074} \pm 0.005$
S_8	$0.167 \, ^{+0.094}_{-0.091} \pm 0.004$	$-0.085 \, ^{+0.072}_{-0.070} \pm 0.006$	$-0.007 \, ^{+0.070}_{-0.072} \pm 0.005$
S_9	$-0.032 \, ^{+0.071}_{-0.071} \pm 0.004$	$-0.024 \, ^{+0.059}_{-0.060} \pm 0.005$	$-0.004 \, ^{+0.070}_{-0.073} \pm 0.006$

	$15.0 < q^2 < 17.0 \, \text{GeV}^2/c^4$	$17.0 < q^2 < 19.0 \, \text{GeV}^2/c^4$
F_{L}	$0.349 \, ^{+0.039}_{-0.039} \pm 0.009$	$0.354 \, ^{+0.049}_{-0.048} \pm 0.025$
S_3	$-0.142 \, ^{+0.044}_{-0.049} \pm 0.007$	$-0.188 \, ^{+0.074}_{-0.084} \pm 0.017$
S_4	$-0.321 \, ^{+0.055}_{-0.074} \pm 0.007$	$-0.266 \, ^{+0.063}_{-0.072} \pm 0.010$
S_5	$-0.316 \, ^{+0.051}_{-0.057} \pm 0.009$	$-0.323 \, ^{+0.063}_{-0.072} \pm 0.009$
A_{FB}	$0.411 \, ^{+0.041}_{-0.037} \pm 0.008$	$0.305 \, ^{+0.049}_{-0.048} \pm 0.013$
S_7	$0.061 \, ^{+0.058}_{-0.058} \pm 0.005$	$0.044 \, ^{+0.073}_{-0.072} \pm 0.013$
S_8	$0.003 \, ^{+0.061}_{-0.061} \pm 0.003$	$0.013 \, ^{+0.071}_{-0.070} \pm 0.005$
S_9	$-0.019 \, ^{+0.054}_{-0.056} \pm 0.004$	$-0.094 \, ^{+0.065}_{-0.067} \pm 0.004$

Table 4. *CP*-averaged angular observables evaluated by the unbinned maximum likelihood fit. The first uncertainties are statistical and the second systematic.

	$0.10 < q^2 < 0.98\,\mathrm{GeV}^2/c^4$	$1.1 < q^2 < 2.5\,\mathrm{GeV}^2/c^4$	$2.5 < q^2 < 4.0\,\mathrm{GeV}^2/c^4$
A_3	$0.006\,^{+0.064}_{-0.065} \pm 0.005$	$0.042\,^{+0.097}_{-0.087} \pm 0.005$	$-0.111\,^{+0.087}_{-0.109} \pm 0.006$
A_4	$-0.068\,^{+0.071}_{-0.073} \pm 0.009$	$0.235\,^{+0.125}_{-0.109} \pm 0.005$	$-0.007\,^{+0.130}_{-0.135} \pm 0.007$
A_5	$0.001\,^{+0.061}_{-0.059} \pm 0.018$	$-0.114\,^{+0.099}_{-0.105} \pm 0.009$	$-0.005\,^{+0.107}_{-0.106} \pm 0.008$
A_{6s}	$0.122\,^{+0.076}_{-0.075} \pm 0.011$	$0.037\,^{+0.102}_{-0.091} \pm 0.016$	$0.022\,^{+0.115}_{-0.096} \pm 0.010$
A_7	$0.076\,^{+0.061}_{-0.060} \pm 0.006$	$-0.087\,^{+0.091}_{-0.093} \pm 0.004$	$-0.032\,^{+0.109}_{-0.115} \pm 0.005$
A_8	$-0.031\,^{+0.074}_{-0.074} \pm 0.007$	$-0.044\,^{+0.108}_{-0.113} \pm 0.005$	$-0.071\,^{+0.124}_{-0.131} \pm 0.006$
A_9	$0.030\,^{+0.062}_{-0.061} \pm 0.004$	$-0.004\,^{+0.092}_{-0.098} \pm 0.005$	$-0.228\,^{+0.114}_{-0.152} \pm 0.007$

	$4.0 < q^2 < 6.0\,\mathrm{GeV}^2/c^4$	$6.0 < q^2 < 8.0\,\mathrm{GeV}^2/c^4$	$11.0 < q^2 < 12.5\,\mathrm{GeV}^2/c^4$
A_3	$-0.173\,^{+0.070}_{-0.079} \pm 0.006$	$0.064\,^{+0.067}_{-0.064} \pm 0.011$	$0.132\,^{+0.075}_{-0.073} \pm 0.005$
A_4	$-0.168\,^{+0.086}_{-0.085} \pm 0.008$	$-0.037\,^{+0.073}_{-0.073} \pm 0.011$	$-0.100\,^{+0.082}_{-0.077} \pm 0.009$
A_5	$-0.059\,^{+0.071}_{-0.073} \pm 0.011$	$0.129\,^{+0.067}_{-0.066} \pm 0.012$	$0.027\,^{+0.077}_{-0.076} \pm 0.010$
A_{6s}	$-0.023\,^{+0.082}_{-0.075} \pm 0.005$	$0.047\,^{+0.062}_{-0.060} \pm 0.011$	$0.024\,^{+0.069}_{-0.067} \pm 0.013$
A_7	$0.041\,^{+0.083}_{-0.082} \pm 0.004$	$0.035\,^{+0.065}_{-0.067} \pm 0.003$	$-0.008\,^{+0.073}_{-0.073} \pm 0.005$
A_8	$0.004\,^{+0.093}_{-0.095} \pm 0.005$	$-0.043\,^{+0.070}_{-0.069} \pm 0.006$	$0.014\,^{+0.075}_{-0.073} \pm 0.005$
A_9	$0.062\,^{+0.078}_{-0.072} \pm 0.004$	$0.110\,^{+0.061}_{-0.060} \pm 0.005$	$-0.057\,^{+0.057}_{-0.059} \pm 0.006$

	$15.0 < q^2 < 17.0\,\mathrm{GeV}^2/c^4$	$17.0 < q^2 < 19.0\,\mathrm{GeV}^2/c^4$
A_3	$-0.034\,^{+0.056}_{-0.055} \pm 0.007$	$-0.056\,^{+0.075}_{-0.073} \pm 0.017$
A_4	$-0.071\,^{+0.064}_{-0.064} \pm 0.008$	$-0.071\,^{+0.073}_{-0.073} \pm 0.011$
A_5	$-0.076\,^{+0.065}_{-0.063} \pm 0.010$	$0.008\,^{+0.073}_{-0.075} \pm 0.010$
A_{6s}	$-0.085\,^{+0.062}_{-0.060} \pm 0.012$	$-0.127\,^{+0.080}_{-0.076} \pm 0.018$
A_7	$-0.105\,^{+0.058}_{-0.059} \pm 0.005$	$0.047\,^{+0.070}_{-0.069} \pm 0.013$
A_8	$0.048\,^{+0.063}_{-0.063} \pm 0.003$	$0.022\,^{+0.072}_{-0.073} \pm 0.005$
A_9	$0.091\,^{+0.059}_{-0.059} \pm 0.004$	$0.043\,^{+0.066}_{-0.067} \pm 0.005$

Table 5. *CP*-asymmetric angular observables evaluated by the unbinned maximum likelihood fit. The first uncertainties are statistical and the second systematic.

	$0.10 < q^2 < 0.98\,\mathrm{GeV}^2/c^4$	$1.1 < q^2 < 2.5\,\mathrm{GeV}^2/c^4$	$2.5 < q^2 < 4.0\,\mathrm{GeV}^2/c^4$
P_1	$-0.099\,^{+0.168}_{-0.163} \pm 0.014$	$-0.451\,^{+0.519}_{-0.636} \pm 0.038$	$0.571\,^{+2.404}_{-1.714} \pm 0.045$
P_2	$-0.003\,^{+0.051}_{-0.052} \pm 0.007$	$-0.373\,^{+0.146}_{-0.199} \pm 0.027$	$-0.636\,^{+0.444}_{-1.735} \pm 0.015$
P_3	$0.113\,^{+0.079}_{-0.079} \pm 0.006$	$0.350\,^{+0.330}_{-0.254} \pm 0.015$	$0.745\,^{+2.587}_{-0.861} \pm 0.030$
P_4'	$0.185\,^{+0.158}_{-0.154} \pm 0.023$	$-0.163\,^{+0.232}_{-0.240} \pm 0.021$	$-0.713\,^{+0.410}_{-1.305} \pm 0.024$
P_5'	$0.387\,^{+0.132}_{-0.133} \pm 0.052$	$0.289\,^{+0.220}_{-0.202} \pm 0.023$	$-0.066\,^{+0.343}_{-0.364} \pm 0.023$
P_6'	$0.034\,^{+0.134}_{-0.135} \pm 0.015$	$-0.463\,^{+0.202}_{-0.221} \pm 0.012$	$0.205\,^{+0.962}_{-0.341} \pm 0.013$
P_8'	$0.180\,^{+0.174}_{-0.169} \pm 0.007$	$-0.208\,^{+0.224}_{-0.270} \pm 0.024$	$0.091\,^{+0.650}_{-0.432} \pm 0.025$

	$4.0 < q^2 < 6.0\,\mathrm{GeV}^2/c^4$	$6.0 < q^2 < 8.0\,\mathrm{GeV}^2/c^4$	$11.0 < q^2 < 12.5\,\mathrm{GeV}^2/c^4$
P_1	$0.180\,^{+0.364}_{-0.348} \pm 0.027$	$-0.199\,^{+0.281}_{-0.275} \pm 0.025$	$-0.745\,^{+0.207}_{-0.230} \pm 0.015$
P_2	$0.042\,^{+0.088}_{-0.087} \pm 0.011$	$0.241\,^{+0.061}_{-0.062} \pm 0.013$	$0.418\,^{+0.053}_{-0.046} \pm 0.005$
P_3	$0.083\,^{+0.187}_{-0.184} \pm 0.023$	$0.057\,^{+0.148}_{-0.139} \pm 0.013$	$0.007\,^{+0.141}_{-0.138} \pm 0.010$
P_4'	$-0.448\,^{+0.169}_{-0.172} \pm 0.020$	$-0.599\,^{+0.131}_{-0.135} \pm 0.010$	$-0.567\,^{+0.169}_{-0.187} \pm 0.014$
P_5'	$-0.300\,^{+0.158}_{-0.159} \pm 0.023$	$-0.505\,^{+0.122}_{-0.122} \pm 0.024$	$-0.655\,^{+0.147}_{-0.160} \pm 0.015$
P_6'	$-0.032\,^{+0.167}_{-0.166} \pm 0.007$	$-0.095\,^{+0.135}_{-0.135} \pm 0.011$	$-0.282\,^{+0.146}_{-0.151} \pm 0.007$
P_8'	$0.342\,^{+0.188}_{-0.185} \pm 0.009$	$-0.171\,^{+0.142}_{-0.143} \pm 0.006$	$-0.015\,^{+0.145}_{-0.142} \pm 0.005$

	$15.0 < q^2 < 17.0\,\mathrm{GeV}^2/c^4$	$17.0 < q^2 < 19.0\,\mathrm{GeV}^2/c^4$
P_1	$-0.436\,^{+0.134}_{-0.147} \pm 0.018$	$-0.581\,^{+0.225}_{-0.263} \pm 0.037$
P_2	$0.421\,^{+0.042}_{-0.035} \pm 0.005$	$0.314\,^{+0.046}_{-0.048} \pm 0.007$
P_3	$0.029\,^{+0.082}_{-0.084} \pm 0.006$	$0.145\,^{+0.107}_{-0.102} \pm 0.008$
P_4'	$-0.672\,^{+0.113}_{-0.151} \pm 0.016$	$-0.556\,^{+0.133}_{-0.156} \pm 0.016$
P_5'	$-0.662\,^{+0.109}_{-0.127} \pm 0.017$	$-0.676\,^{+0.133}_{-0.152} \pm 0.017$
P_6'	$0.127\,^{+0.119}_{-0.122} \pm 0.006$	$0.092\,^{+0.148}_{-0.152} \pm 0.025$
P_8'	$0.007\,^{+0.125}_{-0.129} \pm 0.005$	$0.027\,^{+0.147}_{-0.147} \pm 0.009$

Table 6. Optimised angular observables evaluated by the unbinned maximum likelihood fit. The first uncertainties are statistical and the second systematic.

	$0.10 < q^2 < 0.98\,\mathrm{GeV^2/c^4}$	$1.1 < q^2 < 2.0\,\mathrm{GeV^2/c^4}$	$2.0 < q^2 < 3.0\,\mathrm{GeV^2/c^4}$	$3.0 < q^2 < 4.0\,\mathrm{GeV^2/c^4}$
F_L	$0.242^{+0.058}_{-0.056} \pm 0.026$	$0.768^{+0.141}_{-0.130} \pm 0.025$	$0.690^{+0.113}_{-0.082} \pm 0.023$	$0.873^{+0.154}_{-0.105} \pm 0.023$
S_3	$-0.014^{+0.059}_{-0.060} \pm 0.008$	$0.065^{+0.137}_{-0.127} \pm 0.007$	$0.006^{+0.100}_{-0.100} \pm 0.007$	$0.078^{+0.131}_{-0.122} \pm 0.008$
S_4	$0.039^{+0.091}_{-0.090} \pm 0.015$	$0.127^{+0.190}_{-0.180} \pm 0.027$	$-0.339^{+0.115}_{-0.140} \pm 0.041$	$-0.046^{+0.193}_{-0.196} \pm 0.046$
S_5	$0.129^{+0.068}_{-0.066} \pm 0.011$	$0.286^{+0.168}_{-0.172} \pm 0.009$	$0.206^{+0.131}_{-0.115} \pm 0.009$	$-0.110^{+0.163}_{-0.169} \pm 0.004$
A_FB	$-0.138^{+0.095}_{-0.092} \pm 0.072$	$-0.333^{+0.115}_{-0.130} \pm 0.012$	$-0.158^{+0.080}_{-0.090} \pm 0.008$	$-0.041^{+0.091}_{-0.091} \pm 0.002$
S_7	$0.038^{+0.063}_{-0.062} \pm 0.009$	$-0.293^{+0.180}_{-0.176} \pm 0.005$	$-0.252^{+0.127}_{-0.151} \pm 0.002$	$0.171^{+0.175}_{-0.158} \pm 0.002$
S_8	$0.063^{+0.079}_{-0.080} \pm 0.009$	$-0.114^{+0.185}_{-0.196} \pm 0.006$	$-0.176^{+0.149}_{-0.165} \pm 0.006$	$0.097^{+0.189}_{-0.184} \pm 0.002$
S_9	$-0.113^{+0.061}_{-0.063} \pm 0.004$	$-0.110^{+0.140}_{-0.138} \pm 0.001$	$-0.000^{+0.100}_{-0.102} \pm 0.003$	$-0.203^{+0.112}_{-0.132} \pm 0.002$
S_{6c}	$-0.098^{+0.132}_{-0.134} \pm 0.005$	$-0.010^{+0.223}_{-0.212} \pm 0.003$	$-0.239^{+0.268}_{-0.263} \pm 0.001$	$-0.031^{+0.359}_{-0.337} \pm 0.000$

	$4.0 < q^2 < 5.0\,\mathrm{GeV^2/c^4}$	$5.0 < q^2 < 6.0\,\mathrm{GeV^2/c^4}$	$6.0 < q^2 < 7.0\,\mathrm{GeV^2/c^4}$	$7.0 < q^2 < 8.0\,\mathrm{GeV^2/c^4}$
F_L	$0.899^{+0.106}_{-0.104} \pm 0.023$	$0.644^{+0.130}_{-0.121} \pm 0.025$	$0.644^{+0.089}_{-0.084} \pm 0.025$	$0.609^{+0.103}_{-0.082} \pm 0.025$
S_3	$0.200^{+0.101}_{-0.097} \pm 0.007$	$-0.122^{+0.119}_{-0.126} \pm 0.009$	$-0.069^{+0.089}_{-0.091} \pm 0.004$	$-0.054^{+0.097}_{-0.099} \pm 0.005$
S_4	$-0.148^{+0.154}_{-0.154} \pm 0.047$	$-0.273^{+0.174}_{-0.184} \pm 0.048$	$-0.311^{+0.111}_{-0.118} \pm 0.052$	$-0.236^{+0.116}_{-0.136} \pm 0.058$
S_5	$-0.306^{+0.138}_{-0.141} \pm 0.004$	$-0.095^{+0.137}_{-0.142} \pm 0.004$	$-0.339^{+0.108}_{-0.114} \pm 0.008$	$-0.386^{+0.105}_{-0.135} \pm 0.007$
A_FB	$0.052^{+0.080}_{-0.080} \pm 0.004$	$0.057^{+0.094}_{-0.090} \pm 0.006$	$0.058^{+0.064}_{-0.063} \pm 0.009$	$0.241^{+0.080}_{-0.062} \pm 0.012$
S_7	$-0.082^{+0.129}_{-0.128} \pm 0.001$	$0.038^{+0.135}_{-0.135} \pm 0.002$	$0.009^{+0.123}_{-0.124} \pm 0.004$	$-0.094^{+0.123}_{-0.130} \pm 0.003$
S_8	$0.107^{+0.144}_{-0.146} \pm 0.003$	$-0.037^{+0.160}_{-0.159} \pm 0.003$	$0.080^{+0.131}_{-0.129} \pm 0.002$	$-0.295^{+0.119}_{-0.139} \pm 0.002$
S_9	$0.181^{+0.105}_{-0.099} \pm 0.001$	$-0.080^{+0.117}_{-0.120} \pm 0.001$	$0.061^{+0.091}_{-0.091} \pm 0.001$	$0.030^{+0.100}_{-0.098} \pm 0.001$
S_{6c}	$0.485^{+0.309}_{-0.317} \pm 0.001$	$0.447^{+0.328}_{-0.333} \pm 0.001$	$0.219^{+0.249}_{-0.250} \pm 0.002$	$0.249^{+0.209}_{-0.208} \pm 0.002$

	$11.0 < q^2 < 11.75\,\mathrm{GeV^2/c^4}$	$11.75 < q^2 < 12.5\,\mathrm{GeV^2/c^4}$	$15.0 < q^2 < 16.0\,\mathrm{GeV^2/c^4}$	$16.0 < q^2 < 17.0\,\mathrm{GeV^2/c^4}$
F_L	$0.502^{+0.090}_{-0.082} \pm 0.022$	$0.734^{+0.107}_{-0.094} \pm 0.018$	$0.385^{+0.067}_{-0.066} \pm 0.013$	$0.295^{+0.058}_{-0.062} \pm 0.013$
S_3	$-0.217^{+0.077}_{-0.090} \pm 0.008$	$-0.157^{+0.090}_{-0.098} \pm 0.008$	$-0.060^{+0.085}_{-0.088} \pm 0.006$	$-0.250^{+0.079}_{-0.092} \pm 0.007$
S_4	$-0.252^{+0.095}_{-0.113} \pm 0.063$	$-0.309^{+0.099}_{-0.111} \pm 0.056$	$-0.321^{+0.082}_{-0.099} \pm 0.007$	$-0.246^{+0.083}_{-0.096} \pm 0.029$
S_5	$-0.235^{+0.095}_{-0.115} \pm 0.013$	$-0.366^{+0.096}_{-0.112} \pm 0.012$	$-0.360^{+0.074}_{-0.092} \pm 0.006$	$-0.254^{+0.069}_{-0.081} \pm 0.010$
A_FB	$0.370^{+0.076}_{-0.054} \pm 0.015$	$0.293^{+0.064}_{-0.052} \pm 0.014$	$0.396^{+0.068}_{-0.047} \pm 0.009$	$0.451^{+0.071}_{-0.048} \pm 0.007$
S_7	$-0.110^{+0.108}_{-0.114} \pm 0.002$	$-0.212^{+0.110}_{-0.118} \pm 0.002$	$0.040^{+0.092}_{-0.089} \pm 0.002$	$0.144^{+0.091}_{-0.085} \pm 0.005$
S_8	$-0.079^{+0.120}_{-0.122} \pm 0.003$	$-0.090^{+0.108}_{-0.111} \pm 0.003$	$-0.057^{+0.093}_{-0.095} \pm 0.005$	$0.055^{+0.090}_{-0.088} \pm 0.005$
S_9	$-0.084^{+0.097}_{-0.102} \pm 0.003$	$0.030^{+0.093}_{-0.091} \pm 0.002$	$-0.054^{+0.083}_{-0.087} \pm 0.005$	$-0.014^{+0.084}_{-0.086} \pm 0.004$
S_{6c}	$0.082^{+0.220}_{-0.223} \pm 0.003$	$0.392^{+0.293}_{-0.294} \pm 0.004$	$-0.273^{+0.164}_{-0.161} \pm 0.004$	$-0.112^{+0.127}_{-0.129} \pm 0.003$

	$17.0 < q^2 < 18.0\,\mathrm{GeV^2/c^4}$	$18.0 < q^2 < 19.0\,\mathrm{GeV^2/c^4}$	$15.0 < q^2 < 19.0\,\mathrm{GeV^2/c^4}$
F_L	$0.363^{+0.073}_{-0.072} \pm 0.017$	$0.421^{+0.100}_{-0.100} \pm 0.013$	$0.357^{+0.035}_{-0.035} \pm 0.011$
S_3	$-0.099^{+0.091}_{-0.092} \pm 0.011$	$-0.131^{+0.128}_{-0.130} \pm 0.012$	$-0.135^{+0.046}_{-0.050} \pm 0.012$
S_4	$-0.229^{+0.090}_{-0.096} \pm 0.045$	$-0.607^{+0.153}_{-0.170} \pm 0.059$	$-0.314^{+0.046}_{-0.054} \pm 0.027$
S_5	$-0.305^{+0.081}_{-0.088} \pm 0.015$	$-0.534^{+0.131}_{-0.150} \pm 0.015$	$-0.335^{+0.041}_{-0.047} \pm 0.007$
A_FB	$0.274^{+0.069}_{-0.061} \pm 0.008$	$0.354^{+0.111}_{-0.099} \pm 0.012$	$0.367^{+0.037}_{-0.029} \pm 0.007$
S_7	$0.022^{+0.094}_{-0.093} \pm 0.011$	$0.058^{+0.123}_{-0.124} \pm 0.006$	$0.066^{+0.049}_{-0.046} \pm 0.014$
S_8	$-0.007^{+0.098}_{-0.098} \pm 0.001$	$0.149^{+0.139}_{-0.138} \pm 0.010$	$0.024^{+0.040}_{-0.048} \pm 0.009$
S_9	$-0.090^{+0.092}_{-0.095} \pm 0.002$	$-0.079^{+0.122}_{-0.121} \pm 0.007$	$-0.056^{+0.046}_{-0.047} \pm 0.014$
S_{6c}	$-0.195^{+0.169}_{-0.170} \pm 0.003$	$0.187^{+0.201}_{-0.207} \pm 0.001$	$-0.125^{+0.082}_{-0.084} \pm 0.032$

Table 7. *CP*-averaged angular observables evaluated using the method of moments. The first uncertainties are statistical and the second systematic.

	$0.10 < q^2 < 0.98\,\mathrm{GeV}^2/c^4$	$1.1 < q^2 < 2.0\,\mathrm{GeV}^2/c^4$	$2.0 < q^2 < 3.0\,\mathrm{GeV}^2/c^4$	$3.0 < q^2 < 4.0\,\mathrm{GeV}^2/c^4$
A_3	$-0.040\,^{+0.059}_{-0.061} \pm 0.007$	$-0.134\,^{+0.126}_{-0.136} \pm 0.003$	$-0.018\,^{+0.101}_{-0.100} \pm 0.001$	$-0.118\,^{+0.120}_{-0.132} \pm 0.007$
A_4	$-0.047\,^{+0.090}_{-0.092} \pm 0.013$	$0.283\,^{+0.191}_{-0.181} \pm 0.028$	$0.261\,^{+0.146}_{-0.123} \pm 0.042$	$0.002\,^{+0.194}_{-0.196} \pm 0.045$
A_5	$-0.008\,^{+0.066}_{-0.066} \pm 0.011$	$-0.110\,^{+0.166}_{-0.176} \pm 0.008$	$0.028\,^{+0.124}_{-0.120} \pm 0.008$	$0.015\,^{+0.167}_{-0.168} \pm 0.005$
A_{6s}	$0.167\,^{+0.128}_{-0.127} \pm 0.016$	$0.213\,^{+0.161}_{-0.155} \pm 0.005$	$0.077\,^{+0.121}_{-0.111} \pm 0.004$	$-0.047\,^{+0.121}_{-0.125} \pm 0.001$
A_7	$0.112\,^{+0.064}_{-0.062} \pm 0.010$	$-0.193\,^{+0.167}_{-0.200} \pm 0.006$	$-0.162\,^{+0.130}_{-0.144} \pm 0.003$	$-0.004\,^{+0.165}_{-0.162} \pm 0.003$
A_8	$0.021\,^{+0.080}_{-0.080} \pm 0.012$	$0.130\,^{+0.203}_{-0.180} \pm 0.008$	$-0.060\,^{+0.152}_{-0.161} \pm 0.006$	$0.005\,^{+0.188}_{-0.185} \pm 0.003$
A_9	$0.043\,^{+0.062}_{-0.062} \pm 0.009$	$-0.126\,^{+0.136}_{-0.153} \pm 0.010$	$0.013\,^{+0.102}_{-0.101} \pm 0.007$	$-0.129\,^{+0.115}_{-0.125} \pm 0.003$

	$4.0 < q^2 < 5.0\,\mathrm{GeV}^2/c^4$	$5.0 < q^2 < 6.0\,\mathrm{GeV}^2/c^4$	$6.0 < q^2 < 7.0\,\mathrm{GeV}^2/c^4$	$7.0 < q^2 < 8.0\,\mathrm{GeV}^2/c^4$
A_3	$-0.064\,^{+0.098}_{-0.098} \pm 0.005$	$-0.076\,^{+0.119}_{-0.122} \pm 0.004$	$-0.073\,^{+0.089}_{-0.091} \pm 0.007$	$0.168\,^{+0.104}_{-0.093} \pm 0.005$
A_4	$0.076\,^{+0.155}_{-0.154} \pm 0.047$	$-0.457\,^{+0.174}_{-0.187} \pm 0.048$	$-0.104\,^{+0.121}_{-0.120} \pm 0.052$	$0.058\,^{+0.132}_{-0.127} \pm 0.058$
A_5	$0.051\,^{+0.143}_{-0.142} \pm 0.005$	$-0.011\,^{+0.139}_{-0.139} \pm 0.006$	$0.040\,^{+0.117}_{-0.116} \pm 0.006$	$0.084\,^{+0.122}_{-0.117} \pm 0.007$
A_{6s}	$-0.085\,^{+0.107}_{-0.107} \pm 0.009$	$0.116\,^{+0.124}_{-0.121} \pm 0.003$	$0.063\,^{+0.087}_{-0.083} \pm 0.005$	$0.100\,^{+0.096}_{-0.088} \pm 0.006$
A_7	$-0.146\,^{+0.13}_{-0.13} \pm 0.003$	$0.058\,^{+0.135}_{-0.135} \pm 0.003$	$0.181\,^{+0.125}_{-0.122} \pm 0.005$	$0.064\,^{+0.129}_{-0.125} \pm 0.004$
A_8	$0.183\,^{+0.150}_{-0.146} \pm 0.001$	$-0.195\,^{+0.156}_{-0.167} \pm 0.007$	$0.004\,^{+0.131}_{-0.130} \pm 0.003$	$0.078\,^{+0.131}_{-0.127} \pm 0.002$
A_9	$0.160\,^{+0.103}_{-0.100} \pm 0.008$	$-0.001\,^{+0.118}_{-0.120} \pm 0.002$	$0.125\,^{+0.092}_{-0.090} \pm 0.005$	$0.195\,^{+0.108}_{-0.093} \pm 0.003$

	$11.0 < q^2 < 11.75\,\mathrm{GeV}^2/c^4$	$11.75 < q^2 < 12.5\,\mathrm{GeV}^2/c^4$	$15.0 < q^2 < 16.0\,\mathrm{GeV}^2/c^4$	$16.0 < q^2 < 17.0\,\mathrm{GeV}^2/c^4$
A_3	$0.124\,^{+0.090}_{-0.083} \pm 0.008$	$0.124\,^{+0.096}_{-0.090} \pm 0.008$	$-0.108\,^{+0.085}_{-0.091} \pm 0.005$	$0.016\,^{+0.087}_{-0.087} \pm 0.006$
A_4	$-0.058\,^{+0.101}_{-0.105} \pm 0.063$	$-0.242\,^{+0.102}_{-0.112} \pm 0.056$	$0.059\,^{+0.094}_{-0.091} \pm 0.007$	$-0.110\,^{+0.087}_{-0.093} \pm 0.028$
A_5	$-0.042\,^{+0.102}_{-0.106} \pm 0.013$	$0.097\,^{+0.105}_{-0.102} \pm 0.012$	$0.039\,^{+0.087}_{-0.085} \pm 0.007$	$-0.138\,^{+0.073}_{-0.079} \pm 0.008$
A_{6s}	$0.016\,^{+0.091}_{-0.089} \pm 0.003$	$-0.099\,^{+0.076}_{-0.081} \pm 0.003$	$-0.117\,^{+0.076}_{-0.081} \pm 0.010$	$-0.035\,^{+0.079}_{-0.081} \pm 0.010$
A_7	$-0.064\,^{+0.110}_{-0.113} \pm 0.002$	$0.144\,^{+0.116}_{-0.110} \pm 0.002$	$-0.124\,^{+0.087}_{-0.094} \pm 0.004$	$-0.081\,^{+0.087}_{-0.092} \pm 0.006$
A_8	$0.072\,^{+0.123}_{-0.121} \pm 0.003$	$-0.017\,^{+0.112}_{-0.107} \pm 0.003$	$0.087\,^{+0.095}_{-0.092} \pm 0.005$	$0.013\,^{+0.089}_{-0.089} \pm 0.005$
A_9	$-0.082\,^{+0.097}_{-0.102} \pm 0.003$	$-0.014\,^{+0.092}_{-0.092} \pm 0.002$	$0.145\,^{+0.089}_{-0.082} \pm 0.007$	$0.058\,^{+0.086}_{-0.084} \pm 0.004$

	$17.0 < q^2 < 18.0\,\mathrm{GeV}^2/c^4$	$18.0 < q^2 < 19.0\,\mathrm{GeV}^2/c^4$	$15.0 < q^2 < 19.0\,\mathrm{GeV}^2/c^4$
A_3	$-0.145\,^{+0.090}_{-0.094} \pm 0.010$	$0.050\,^{+0.133}_{-0.129} \pm 0.011$	$-0.053\,^{+0.047}_{-0.048} \pm 0.011$
A_4	$-0.071\,^{+0.093}_{-0.095} \pm 0.045$	$-0.120\,^{+0.155}_{-0.162} \pm 0.059$	$-0.049\,^{+0.049}_{-0.052} \pm 0.027$
A_5	$-0.020\,^{+0.085}_{-0.086} \pm 0.015$	$0.186\,^{+0.134}_{-0.131} \pm 0.015$	$-0.010\,^{+0.044}_{-0.044} \pm 0.008$
A_{6s}	$-0.109\,^{+0.087}_{-0.091} \pm 0.009$	$-0.167\,^{+0.132}_{-0.139} \pm 0.007$	$-0.096\,^{+0.045}_{-0.044} \pm 0.008$
A_7	$-0.025\,^{+0.093}_{-0.094} \pm 0.011$	$0.022\,^{+0.125}_{-0.122} \pm 0.006$	$-0.062\,^{+0.048}_{-0.049} \pm 0.014$
A_8	$0.131\,^{+0.100}_{-0.097} \pm 0.004$	$-0.029\,^{+0.140}_{-0.138} \pm 0.010$	$0.059\,^{+0.050}_{-0.049} \pm 0.010$
A_9	$0.116\,^{+0.095}_{-0.092} \pm 0.006$	$-0.147\,^{+0.121}_{-0.128} \pm 0.007$	$0.065\,^{+0.048}_{-0.045} \pm 0.016$

Table 8. *CP*-asymmetries evaluated using the method of moments. The first uncertainties are statistical and the second systematic.

	$0.10 < q^2 < 0.98\,\mathrm{GeV}^2/c^4$	$1.1 < q^2 < 2.0\,\mathrm{GeV}^2/c^4$	$2.0 < q^2 < 3.0\,\mathrm{GeV}^2/c^4$	$3.0 < q^2 < 4.0\,\mathrm{GeV}^2/c^4$
P_1	$-0.038\,^{+0.157}_{-0.158} \pm 0.020$	$0.439\,^{+1.916}_{-1.013} \pm 0.012$	$0.055\,^{+0.677}_{-0.756} \pm 0.007$	$0.421\,^{+18.35}_{-1.190} \pm 0.018$
P_2	$-0.119\,^{+0.080}_{-0.081} \pm 0.063$	$-0.667\,^{+0.149}_{-1.939} \pm 0.017$	$-0.323\,^{+0.147}_{-0.316} \pm 0.033$	$-0.117\,^{+0.485}_{-4.435} \pm 0.015$
P_3	$0.147\,^{+0.086}_{-0.080} \pm 0.005$	$0.363\,^{+1.088}_{-0.506} \pm 0.001$	$0.005\,^{+0.362}_{-0.364} \pm 0.012$	$0.905\,^{+17.51}_{-0.258} \pm 0.009$
P_4'	$0.086\,^{+0.221}_{-0.209} \pm 0.026$	$0.266\,^{+0.648}_{-0.406} \pm 0.057$	$-0.765\,^{+0.271}_{-0.359} \pm 0.099$	$-0.134\,^{+0.810}_{-1.343} \pm 0.108$
P_5'	$0.300\,^{+0.171}_{-0.152} \pm 0.023$	$0.606\,^{+0.769}_{-0.326} \pm 0.017$	$0.461\,^{+0.313}_{-0.256} \pm 0.019$	$-0.295\,^{+0.508}_{-7.112} \pm 0.023$
P_6'	$0.086\,^{+0.152}_{-0.145} \pm 0.024$	$-0.632\,^{+0.347}_{-0.753} \pm 0.009$	$-0.549\,^{+0.276}_{-0.393} \pm 0.005$	$0.449\,^{+19.04}_{-0.397} \pm 0.007$
P_8'	$0.143\,^{+0.195}_{-0.184} \pm 0.022$	$-0.244\,^{+0.433}_{-0.645} \pm 0.012$	$-0.393\,^{+0.332}_{-0.388} \pm 0.002$	$0.303\,^{+1.394}_{-0.719} \pm 0.006$

	$4.0 < q^2 < 5.0\,\mathrm{GeV}^2/c^4$	$5.0 < q^2 < 6.0\,\mathrm{GeV}^2/c^4$	$6.0 < q^2 < 7.0\,\mathrm{GeV}^2/c^4$	$7.0 < q^2 < 8.0\,\mathrm{GeV}^2/c^4$
P_1	$2.296\,^{+17.71}_{-0.694} \pm 0.024$	$-0.540\,^{+0.521}_{-1.100} \pm 0.025$	$-0.353\,^{+0.469}_{-0.602} \pm 0.026$	$-0.284\,^{+0.513}_{-0.548} \pm 0.025$
P_2	$0.174\,^{+3.034}_{-0.376} \pm 0.010$	$0.089\,^{+0.227}_{-0.155} \pm 0.012$	$0.104\,^{+0.136}_{-0.155} \pm 0.013$	$0.393\,^{+0.231}_{-0.093} \pm 0.013$
P_3	$-0.801\,^{+0.221}_{-17.42} \pm 0.007$	$0.178\,^{+0.465}_{-0.286} \pm 0.007$	$-0.161\,^{+0.246}_{-0.291} \pm 0.001$	$-0.063\,^{+0.244}_{-0.298} \pm 0.002$
P_4'	$-0.415\,^{+0.438}_{-1.911} \pm 0.104$	$-0.561\,^{+0.345}_{-0.465} \pm 0.101$	$-0.641\,^{+0.222}_{-0.294} \pm 0.106$	$-0.503\,^{+0.253}_{-0.288} \pm 0.118$
P_5'	$-0.799\,^{+0.266}_{-18.19} \pm 0.022$	$-0.197\,^{+0.287}_{-0.334} \pm 0.018$	$-0.713\,^{+0.228}_{-0.268} \pm 0.015$	$-0.808\,^{+0.226}_{-0.303} \pm 0.010$
P_6'	$-0.215\,^{+0.397}_{-1.243} \pm 0.006$	$0.074\,^{+0.309}_{-0.288} \pm 0.005$	$0.017\,^{+0.267}_{-0.261} \pm 0.007$	$-0.201\,^{+0.261}_{-0.274} \pm 0.007$
P_8'	$0.293\,^{+1.522}_{-0.441} \pm 0.006$	$-0.068\,^{+0.338}_{-0.372} \pm 0.006$	$0.162\,^{+0.289}_{-0.267} \pm 0.005$	$-0.623\,^{+0.255}_{-0.295} \pm 0.005$

	$11.0 < q^2 < 11.75\,\mathrm{GeV}^2/c^4$	$11.75 < q^2 < 12.5\,\mathrm{GeV}^2/c^4$	$15.0 < q^2 < 16.0\,\mathrm{GeV}^2/c^4$	$16.0 < q^2 < 17.0\,\mathrm{GeV}^2/c^4$
P_1	$-0.869\,^{+0.304}_{-0.408} \pm 0.030$	$-1.002\,^{+0.502}_{-1.360} \pm 0.030$	$-0.199\,^{+0.280}_{-0.285} \pm 0.014$	$-0.726\,^{+0.239}_{-0.241} \pm 0.014$
P_2	$0.494\,^{+0.134}_{-0.071} \pm 0.013$	$0.637\,^{+0.599}_{-0.100} \pm 0.008$	$0.433\,^{+0.074}_{-0.054} \pm 0.005$	$0.430\,^{+0.063}_{-0.049} \pm 0.007$
P_3	$0.166\,^{+0.221}_{-0.192} \pm 0.005$	$-0.105\,^{+0.349}_{-0.42} \pm 0.004$	$0.087\,^{+0.144}_{-0.135} \pm 0.007$	$0.019\,^{+0.122}_{-0.119} \pm 0.006$
P_4'	$-0.522\,^{+0.203}_{-0.222} \pm 0.128$	$-0.701\,^{+0.215}_{-0.342} \pm 0.114$	$-0.673\,^{+0.178}_{-0.199} \pm 0.013$	$-0.552\,^{+0.191}_{-0.213} \pm 0.055$
P_5'	$-0.485\,^{+0.203}_{-0.224} \pm 0.028$	$-0.827\,^{+0.205}_{-0.357} \pm 0.026$	$-0.758\,^{+0.165}_{-0.179} \pm 0.013$	$-0.567\,^{+0.157}_{-0.186} \pm 0.014$
P_6'	$-0.233\,^{+0.227}_{-0.224} \pm 0.004$	$-0.473\,^{+0.233}_{-0.344} \pm 0.004$	$0.083\,^{+0.189}_{-0.187} \pm 0.004$	$0.328\,^{+0.192}_{-0.195} \pm 0.012$
P_8'	$-0.159\,^{+0.241}_{-0.250} \pm 0.007$	$-0.211\,^{+0.255}_{-0.274} \pm 0.007$	$-0.120\,^{+0.192}_{-0.198} \pm 0.010$	$0.122\,^{+0.199}_{-0.196} \pm 0.010$

	$17.0 < q^2 < 18.0\,\mathrm{GeV}^2/c^4$	$18.0 < q^2 < 19.0\,\mathrm{GeV}^2/c^4$	$15.0 < q^2 < 19.0\,\mathrm{GeV}^2/c^4$
P_1	$-0.313\,^{+0.286}_{-0.293} \pm 0.019$	$-0.450\,^{+0.440}_{-0.447} \pm 0.022$	$-0.424\,^{+0.139}_{-0.150} \pm 0.028$
P_2	$0.288\,^{+0.075}_{-0.064} \pm 0.006$	$0.393\,^{+0.159}_{-0.100} \pm 0.011$	$0.385\,^{+0.035}_{-0.036} \pm 0.010$
P_3	$0.144\,^{+0.149}_{-0.147} \pm 0.002$	$0.134\,^{+0.219}_{-0.208} \pm 0.010$	$0.089\,^{+0.071}_{-0.072} \pm 0.019$
P_4'	$-0.486\,^{+0.190}_{-0.200} \pm 0.092$	$-1.221\,^{+0.280}_{-0.388} \pm 0.119$	$-0.663\,^{+0.102}_{-0.105} \pm 0.055$
P_5'	$-0.646\,^{+0.176}_{-0.190} \pm 0.027$	$-1.070\,^{+0.237}_{-0.349} \pm 0.029$	$-0.709\,^{+0.093}_{-0.090} \pm 0.016$
P_6'	$0.047\,^{+0.198}_{-0.197} \pm 0.023$	$0.128\,^{+0.246}_{-0.265} \pm 0.012$	$0.140\,^{+0.101}_{-0.100} \pm 0.032$
P_8'	$-0.006\,^{+0.199}_{-0.215} \pm 0.001$	$0.300\,^{+0.297}_{-0.276} \pm 0.022$	$0.049\,^{+0.106}_{-0.102} \pm 0.021$

Table 9. Optimised observables evaluated using the method of moments. The first uncertainties are statistical and the second systematic.

B   Likelihood fit projections

Figure 15 shows the projection of the fitted probability density function on the angular and mass distributions for the $B^0 \to J/\psi K^{*0}$ control sample. Similarly, figures 16–24 show the projections for the $B^0 \to K^{*0}\mu^+\mu^-$ data in the different q^2 bins. The candidates in figure 24 have been weighted to correct for the detector acceptance according to section 5. In the other figures, the acceptance is included in the shape of the signal distribution.
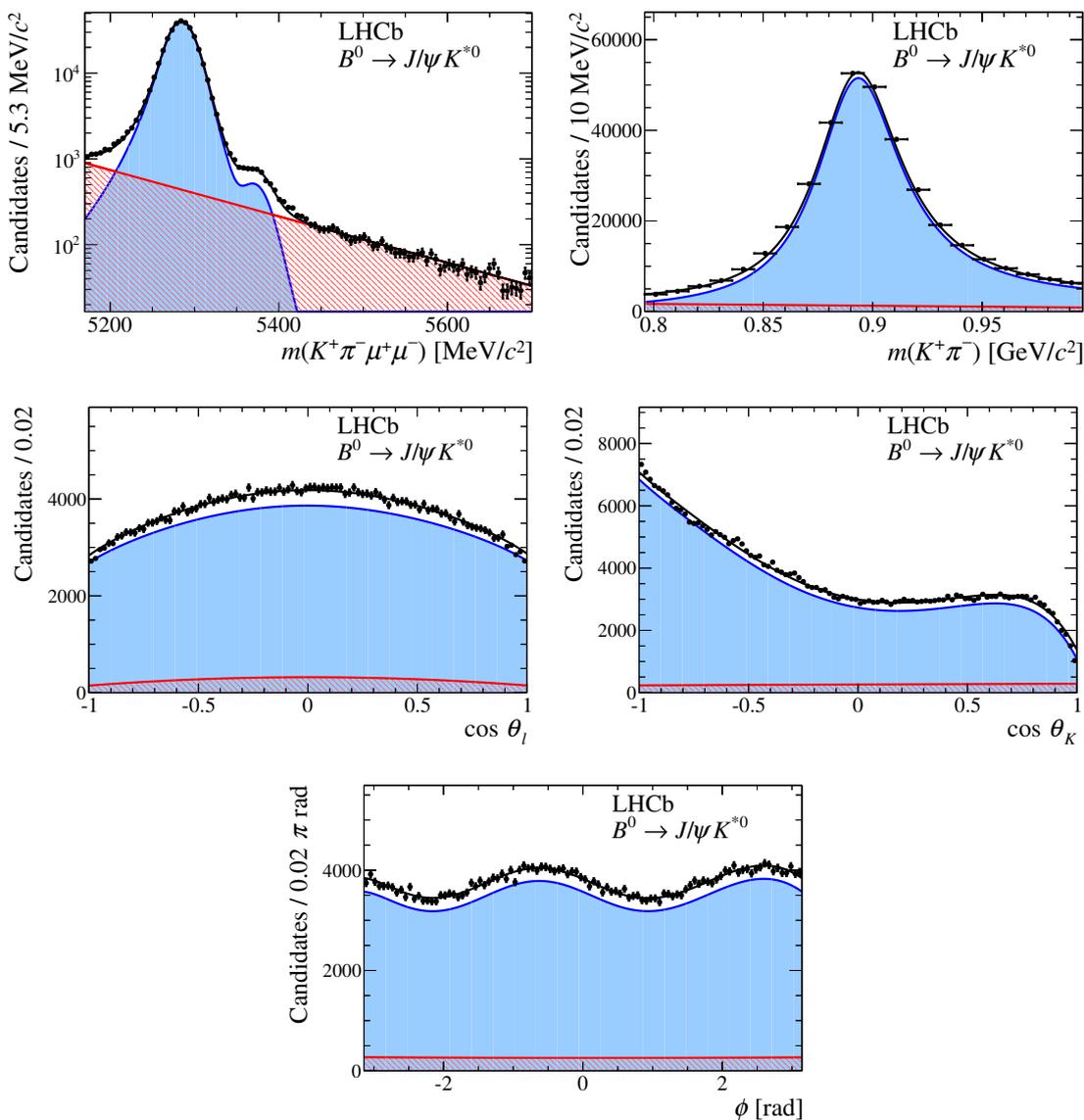
Figure 15. Angular and mass distribution of $B^0 \to J/\psi K^{*0}$ candidates in data. A small signal component is also included in the fit to account for $\overline{B}^0_s \to J/\psi K^{*0}$ decays. Overlaid are the projections of the total fitted distribution (black line) and its different components. The signal is shown by the solid blue component and the background by the red hatched component.

– 38 –
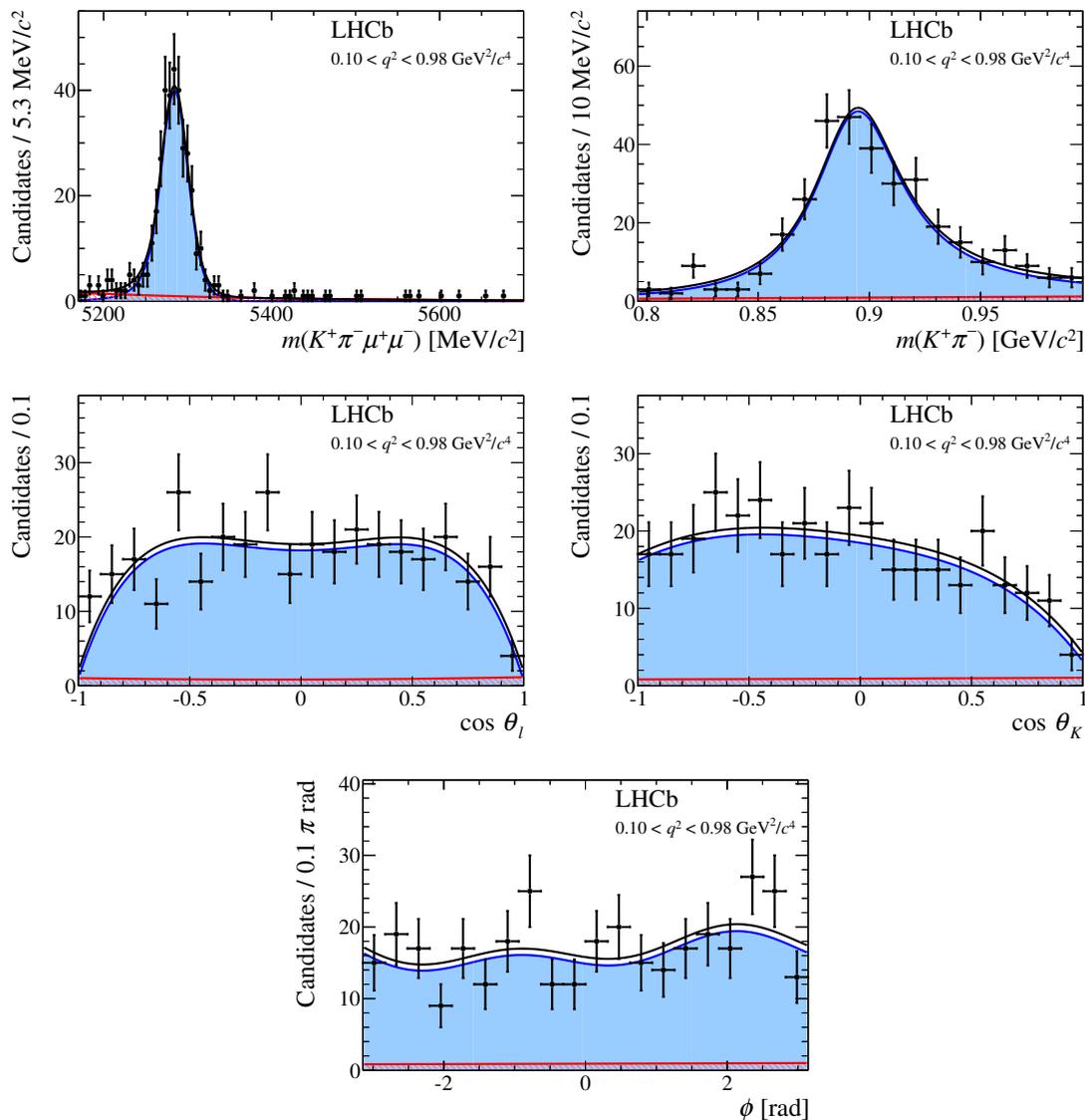
Figure 16. Angular and mass distributions for $0.10 < q^2 < 0.98 \, \text{GeV}^2/c^4$. The distributions of $m(K^+\pi^-)$ and the three decay angles are given for candidates in the signal mass window $\pm 50 \, \text{MeV}/c^2$ around the known B^0 mass. Overlaid are the projections of the total fitted distribution (black line) and its different components. The signal is shown by the solid blue component and the background by the red hatched component.
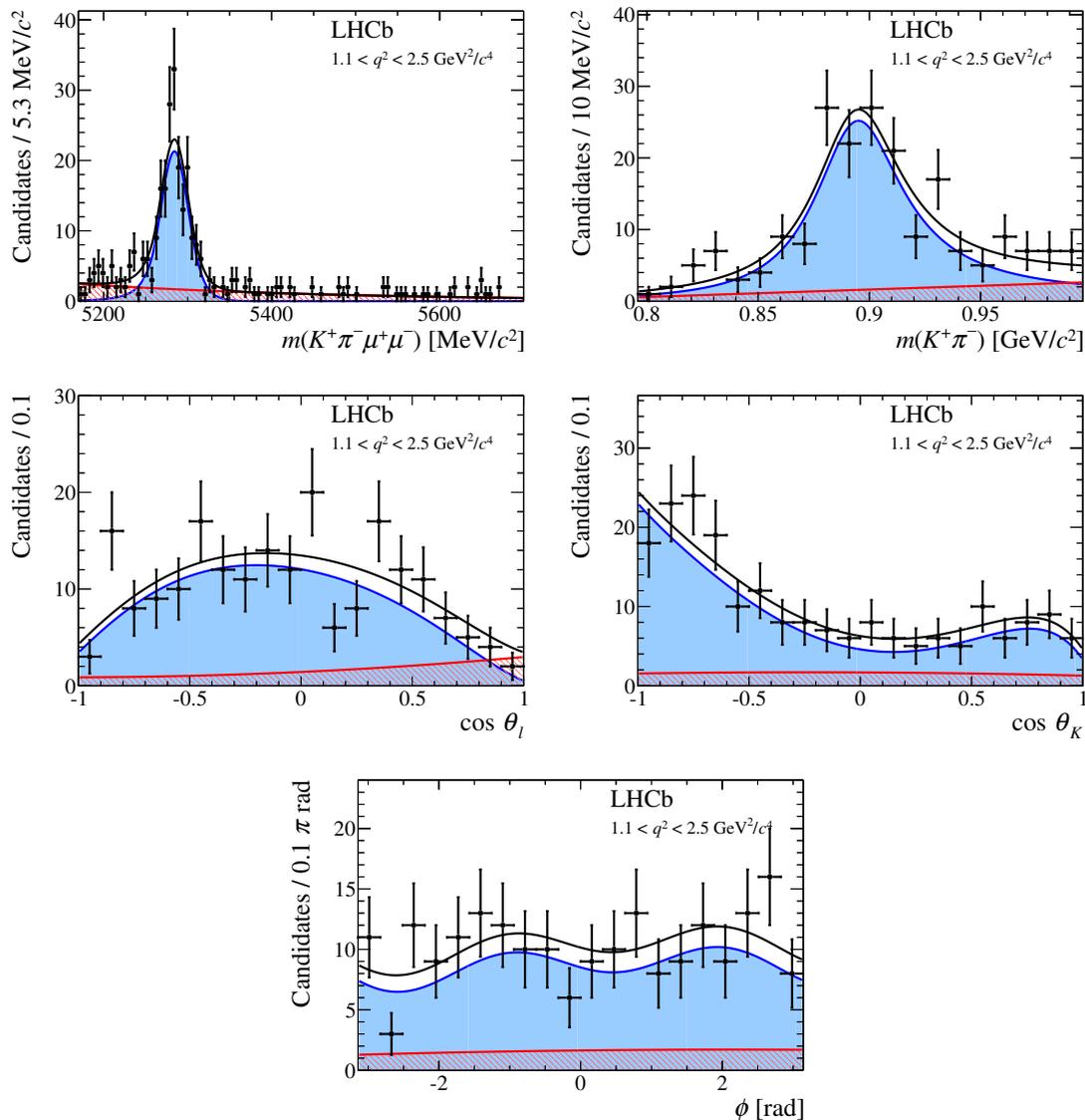
Figure 17. Angular and mass distributions for $1.1 < q^2 < 2.5\,\mathrm{GeV}^2/c^4$. The distributions of $m(K^+\pi^-)$ and the three decay angles are given for candidates in the signal mass window $\pm 50\,\mathrm{MeV}/c^2$ around the known B^0 mass. Overlaid are the projections of the total fitted distribution (black line) and its different components. The signal is shown by the solid blue component and the background by the red hatched component.
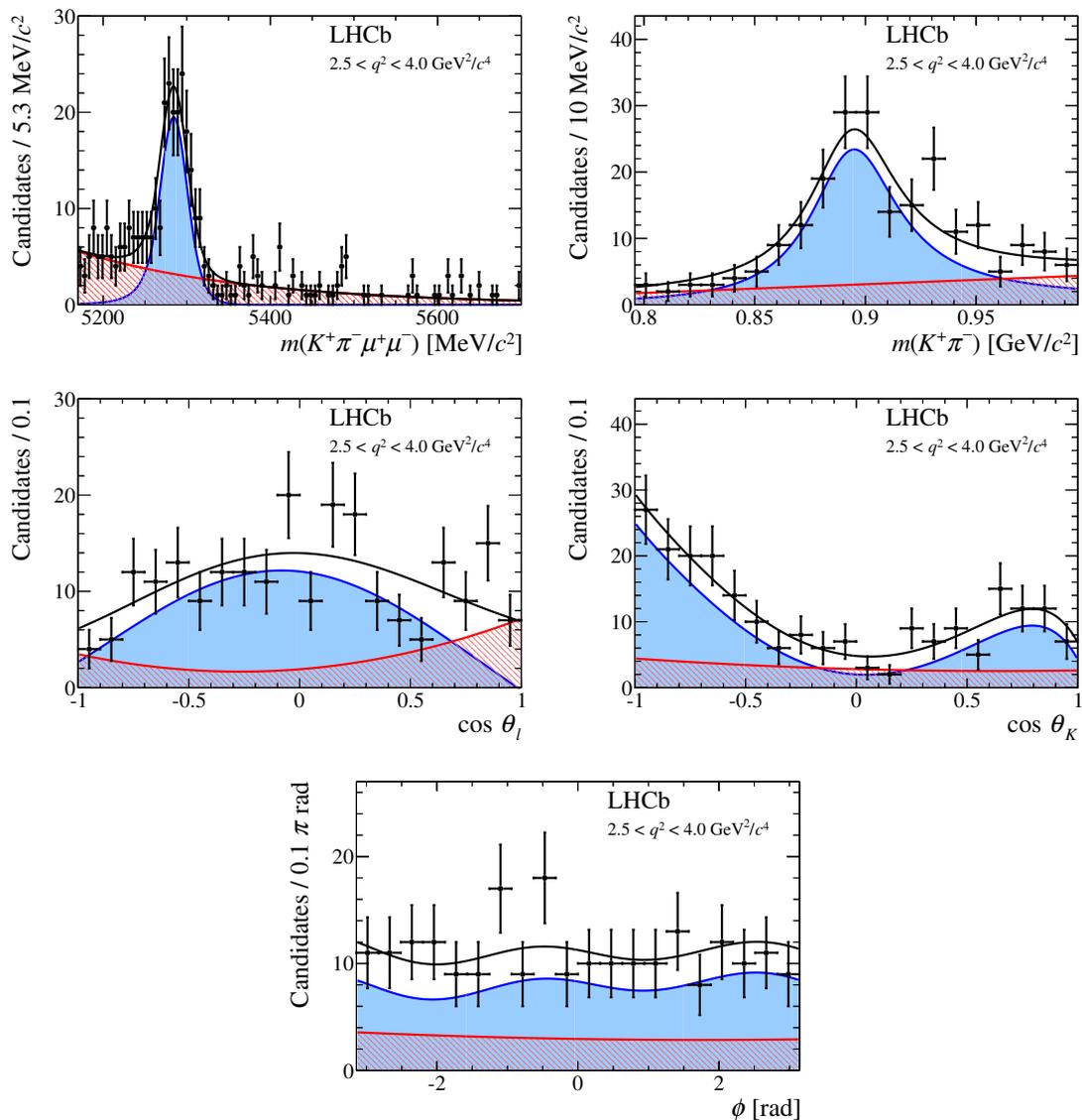
Figure 18. Angular and mass distributions for $2.5 < q^2 < 4.0\,\mathrm{GeV}^2/c^4$. The distributions of $m(K^+\pi^-)$ and the three decay angles are given for candidates in the signal mass window $\pm 50\,\mathrm{MeV}/c^2$ around the known B^0 mass. Overlaid are the projections of the total fitted distribution (black line) and its different components. The signal is shown by the solid blue component and the background by the red hatched component.
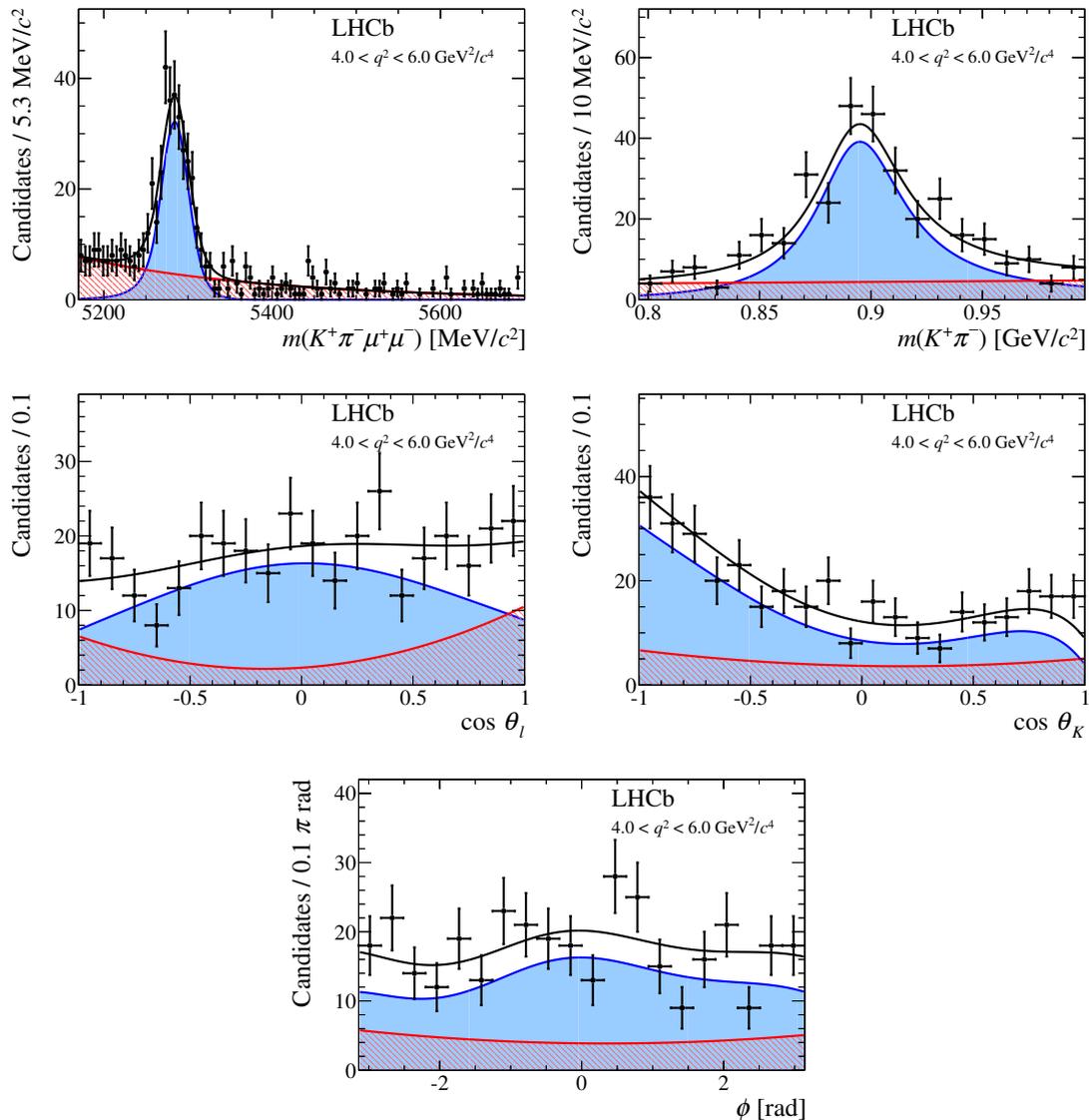
Figure 19. Angular and mass distributions for $4.0 < q^2 < 6.0\,\mathrm{GeV}^2/c^4$. The distributions of $m(K^+\pi^-)$ and the three decay angles are given for candidates in the signal mass window $\pm 50\,\mathrm{MeV}/c^2$ around the known B^0 mass. Overlaid are the projections of the total fitted distribution (black line) and its different components. The signal is shown by the solid blue component and the background by the red hatched component.
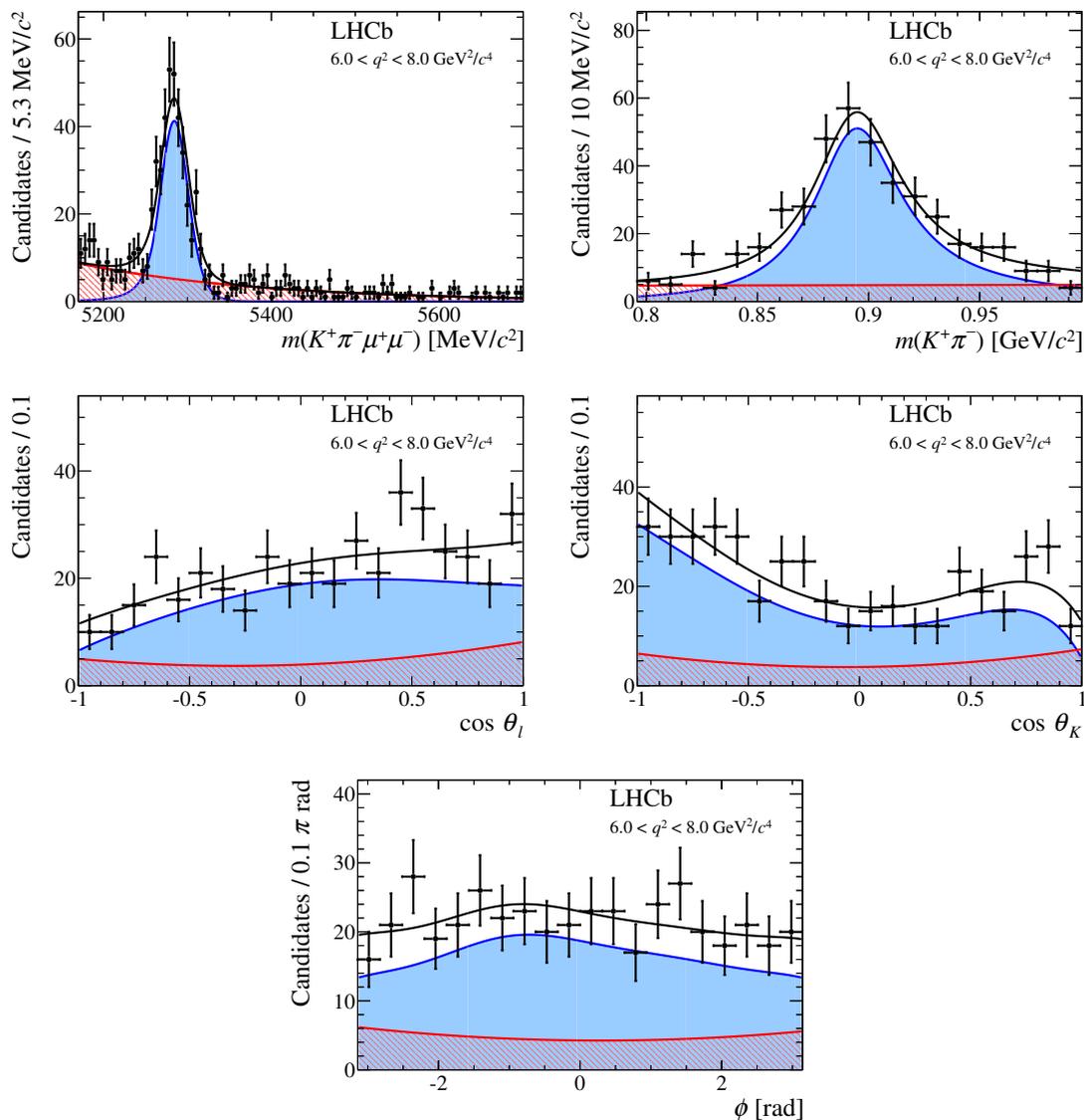
Figure 20. Angular and mass distributions for $6.0 < q^2 < 8.0\,\mathrm{GeV}^2/c^4$. The distributions of $m(K^+\pi^-)$ and the three decay angles are given for candidates in the signal mass window $\pm 50\,\mathrm{MeV}/c^2$ around the known B^0 mass. Overlaid are the projections of the total fitted distribution (black line) and its different components. The signal is shown by the blue shaded area and the background by the red hatched area.
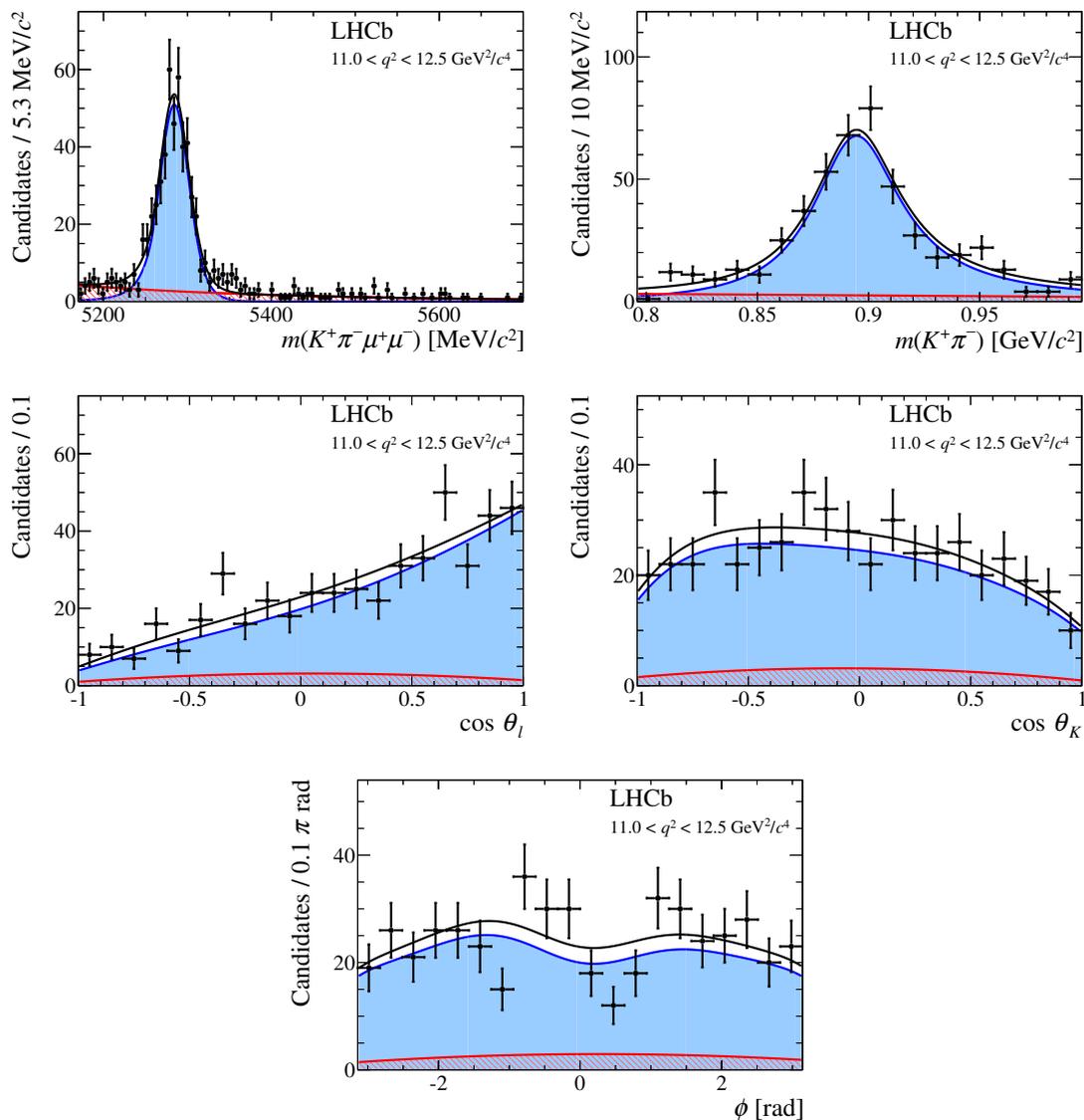
Figure 21. Angular and mass distributions for $11.0 < q^2 < 12.5\,\mathrm{GeV^2}/c^4$. The distributions of $m(K^+\pi^-)$ and the three decay angles are given for candidates in the signal mass window $\pm 50\,\mathrm{MeV}/c^2$ around the known B^0 mass. Overlaid are the projections of the total fitted distribution (black line) and its different components. The signal is shown by the blue shaded area and the background by the red hatched area.
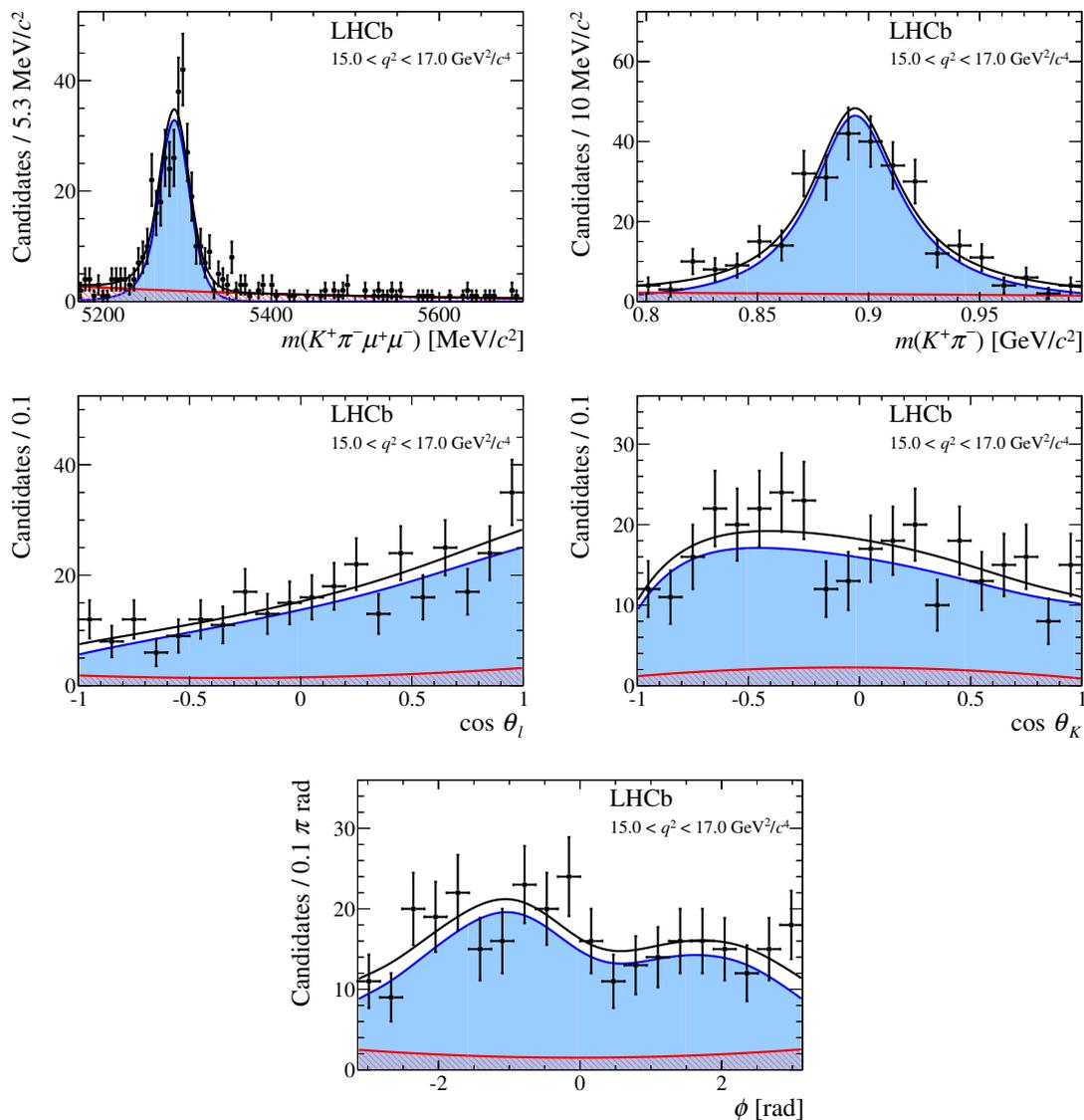
Figure 22. Angular and mass distributions for $15.0 < q^2 < 17.0\,\mathrm{GeV}^2/c^4$. The distributions of $m(K^+\pi^-)$ and the three decay angles are given for candidates in the signal mass window $\pm 50\,\mathrm{MeV}/c^2$ around the known B^0 mass. Overlaid are the projections of the total fitted distribution (black line) and its different components. The signal is shown by the blue shaded area and the background by the red hatched area.
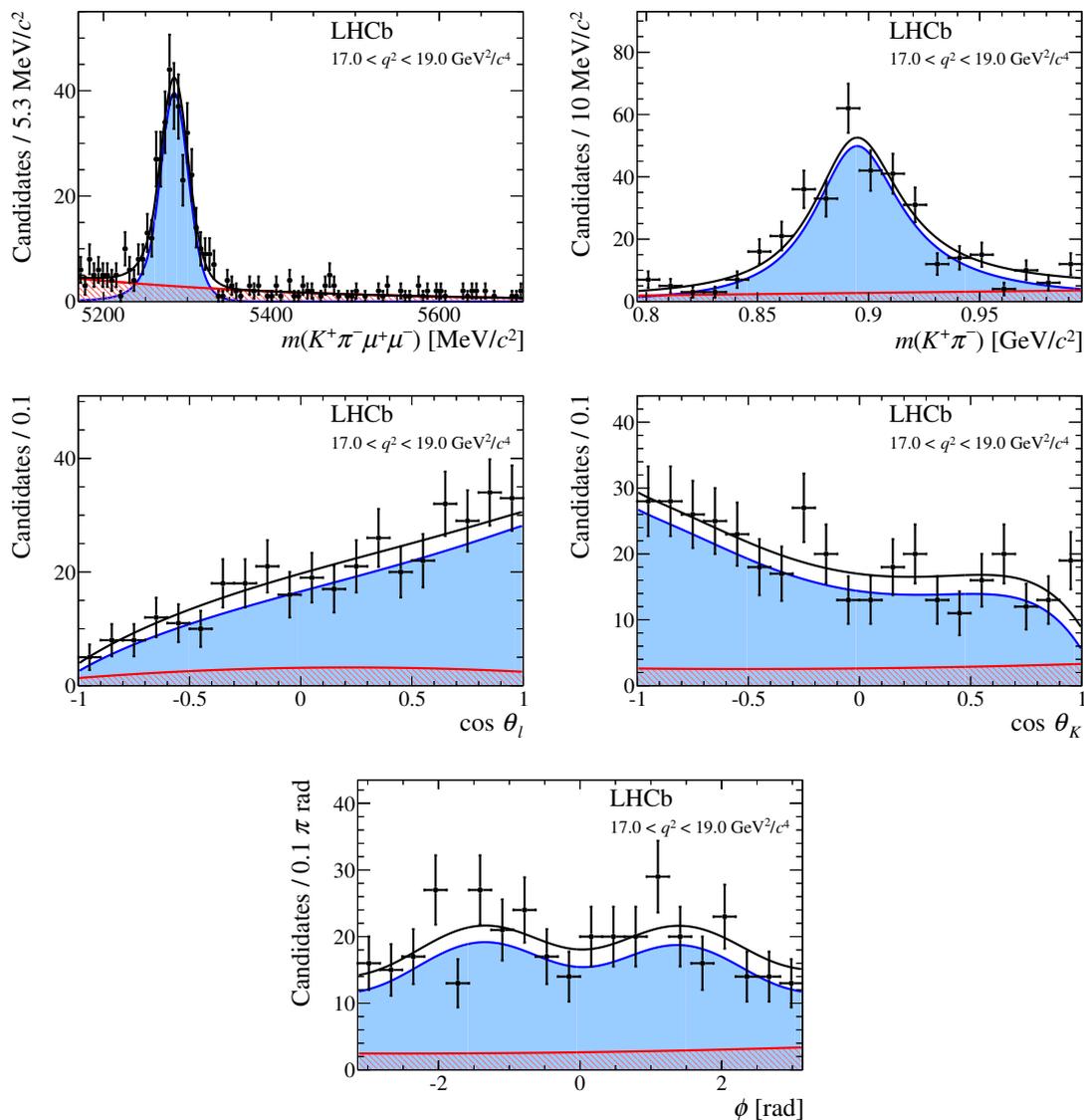
Figure 23. Angular and mass distributions for $17.0 < q^2 < 19.0 \, \text{GeV}^2/c^4$. The distributions of $m(K^+\pi^-)$ and the three decay angles are given for candidates in the signal mass window $\pm 50 \, \text{MeV}/c^2$ around the known B^0 mass. Overlaid are the projections of the total fitted distribution (black line) and its different components. The signal is shown by the blue shaded area and the background by the red hatched area.
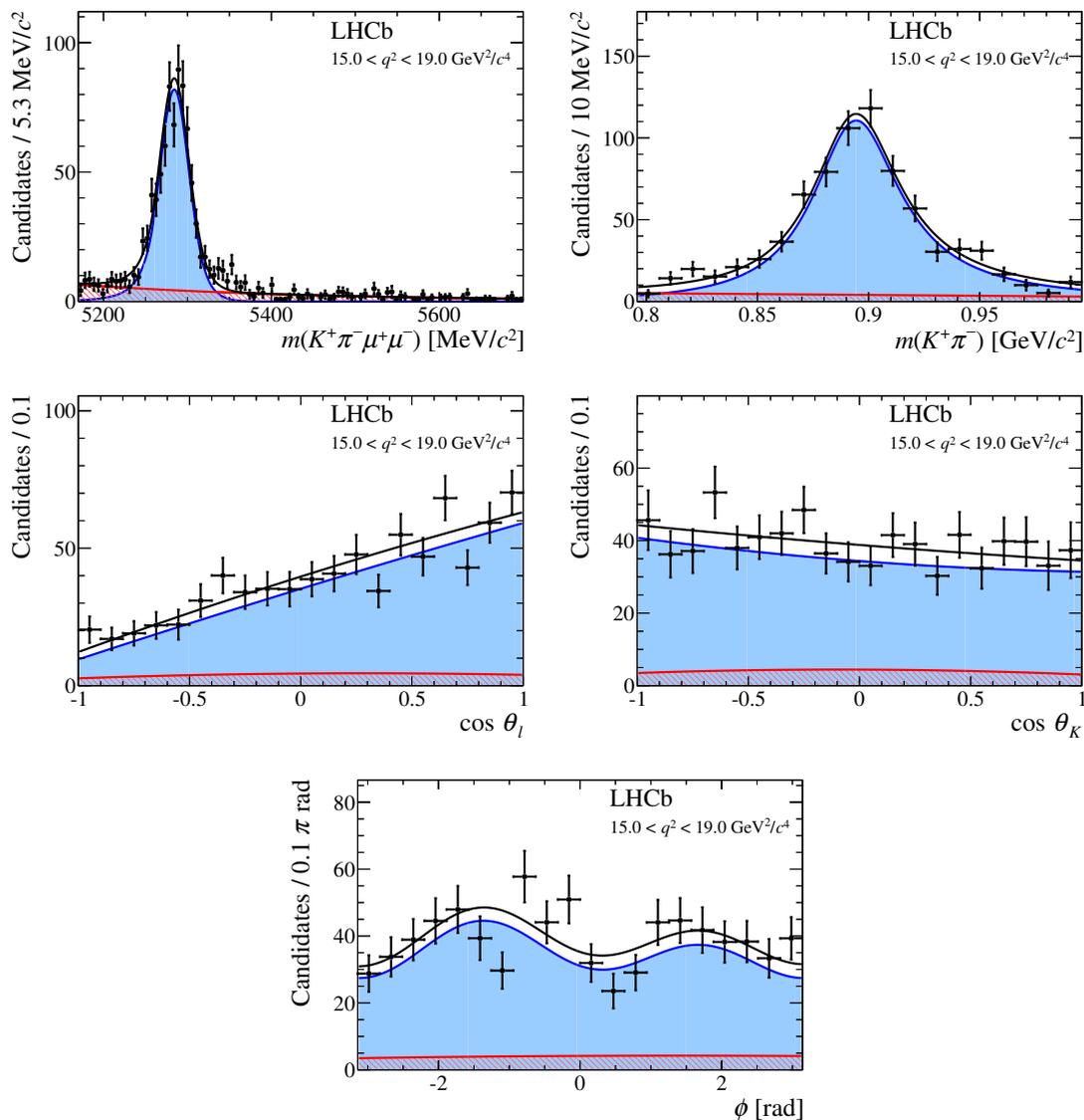
Figure 24. Angular and mass distributions for $15.0 < q^2 < 19.0 \, \text{GeV}^2/c^4$. The distributions of $m(K^+\pi^-)$ and the three decay angles are given for candidates in the signal mass window $\pm 50 \, \text{MeV}/c^2$ around the known B^0 mass. Overlaid are the projections of the total fitted distribution (black line) and its different components. The signal is shown by the blue shaded area and the background by the red hatched area.

C   Correlation matrices for the *CP*-averaged observables from the maximum likelihood fit

Correlation matrices between the *CP*-averaged observables in the different q^2 bins are provided in tables 10–19 for the likelihood fit.

	$F_{\rm L}$	S_3	S_4	S_5	$A_{\rm FB}$	S_7	S_8	S_9
$F_{\rm L}$	1.00	0.06	0.00	0.03	0.04	-0.02	0.07	0.08
S_3		1.00	0.01	0.10	-0.00	-0.07	-0.01	-0.03
S_4			1.00	0.08	0.11	-0.00	0.07	0.02
S_5				1.00	0.05	-0.01	0.00	0.04
$A_{\rm FB}$					1.00	0.03	-0.07	0.02
S_7						1.00	0.01	0.11
S_8							1.00	0.02
S_9								1.00

Table 10. Correlation matrix for the *CP*-averaged observables from the maximum likelihood fit in the bin $0.10 < q^2 < 0.98 \, {\rm GeV}^2/c^4$.

	$F_{\rm L}$	S_3	S_4	S_5	$A_{\rm FB}$	S_7	S_8	S_9
$F_{\rm L}$	1.00	0.09	0.07	0.07	0.09	-0.05	-0.04	0.08
S_3		1.00	-0.04	0.04	0.01	0.13	0.09	0.12
S_4			1.00	-0.22	-0.01	-0.00	-0.05	0.03
S_5				1.00	-0.14	-0.11	-0.03	-0.21
$A_{\rm FB}$					1.00	-0.03	-0.10	-0.11
S_7						1.00	-0.11	0.23
S_8							1.00	-0.04
S_9								1.00

Table 11. Correlation matrix for the *CP*-averaged observables from the maximum likelihood fit in the bin $1.1 < q^2 < 2.5 \, {\rm GeV}^2/c^4$.

	$F_{\rm L}$	S_3	S_4	S_5	$A_{\rm FB}$	S_7	S_8	S_9
$F_{\rm L}$	1.00	-0.13	-0.14	0.01	-0.03	0.10	-0.03	-0.01
S_3		1.00	-0.06	0.09	0.07	-0.02	0.01	-0.07
S_4			1.00	-0.19	-0.09	-0.05	0.12	0.07
S_5				1.00	-0.01	0.05	-0.02	0.10
$A_{\rm FB}$					1.00	-0.01	-0.10	0.10
S_7						1.00	0.07	-0.05
S_8							1.00	-0.01
S_9								1.00

Table 12. Correlation matrix for the *CP*-averaged observables from the maximum likelihood fit in the bin $2.5 < q^2 < 4.0 \, {\rm GeV}^2/c^4$.

	F_L	S_3	S_4	S_5	A_{FB}	S_7	S_8	S_9
F_L	1.00	−0.03	0.09	0.10	−0.05	−0.10	0.04	0.00
S_3		1.00	−0.04	−0.03	0.09	−0.10	−0.00	−0.12
S_4			1.00	0.10	−0.10	−0.02	−0.04	0.04
S_5				1.00	−0.06	−0.03	−0.01	−0.04
A_{FB}					1.00	0.03	0.07	−0.03
S_7						1.00	0.06	−0.15
S_8							1.00	0.03
S_9								1.00

Table 13. Correlation matrix for the *CP*-averaged observables from the maximum likelihood fit in the bin $4.0 < q^2 < 6.0 \, \text{GeV}^2/c^4$.

	F_L	S_3	S_4	S_5	A_{FB}	S_7	S_8	S_9
F_L	1.00	0.03	0.06	0.03	−0.31	−0.08	−0.01	−0.06
S_3		1.00	−0.16	−0.23	0.01	0.02	0.02	−0.07
S_4			1.00	−0.13	−0.12	−0.01	−0.11	0.01
S_5				1.00	−0.16	−0.14	−0.01	−0.04
A_{FB}					1.00	−0.01	0.04	0.02
S_7						1.00	0.10	−0.05
S_8							1.00	−0.10
S_9								1.00

Table 14. Correlation matrix for the *CP*-averaged observables from the maximum likelihood fit in the bin $6.0 < q^2 < 8.0 \, \text{GeV}^2/c^4$.

	F_L	S_3	S_4	S_5	A_{FB}	S_7	S_8	S_9
F_L	1.00	0.25	0.02	−0.02	−0.62	0.03	0.05	0.02
S_3		1.00	0.05	−0.35	−0.24	−0.04	0.06	−0.02
S_4			1.00	−0.02	0.06	−0.05	−0.12	−0.08
S_5				1.00	0.01	−0.04	−0.09	−0.24
A_{FB}					1.00	−0.01	−0.06	0.07
S_7						1.00	0.27	−0.19
S_8							1.00	−0.09
S_9								1.00

Table 15. Correlation matrix for the *CP*-averaged observables from the maximum likelihood fit in the bin $11.0 < q^2 < 12.5 \, \text{GeV}^2/c^4$.

	F_L	S_3	S_4	S_5	A_{FB}	S_7	S_8	S_9
F_L	1.00	0.26	-0.10	0.09	-0.50	-0.02	-0.06	0.14
S_3		1.00	-0.08	-0.03	-0.00	-0.04	-0.05	0.10
S_4			1.00	0.26	-0.16	-0.05	0.19	0.05
S_5				1.00	-0.20	0.12	-0.01	0.05
A_{FB}					1.00	0.05	-0.02	-0.08
S_7						1.00	0.25	-0.23
S_8							1.00	-0.11
S_9								1.00

Table 16. Correlation matrix for the *CP*-averaged observables from the maximum likelihood fit in the bin $15.0 < q^2 < 17.0 \, \text{GeV}^2/c^4$.

	F_L	S_3	S_4	S_5	A_{FB}	S_7	S_8	S_9
F_L	1.00	0.07	0.06	0.04	-0.35	0.07	0.07	0.08
S_3		1.00	-0.15	-0.39	-0.05	-0.06	-0.04	-0.07
S_4			1.00	0.10	-0.17	0.03	0.18	-0.04
S_5				1.00	-0.11	0.04	0.01	-0.00
A_{FB}					1.00	-0.02	-0.09	-0.03
S_7						1.00	0.34	-0.15
S_8							1.00	-0.11
S_9								1.00

Table 17. Correlation matrix for the *CP*-averaged observables from the maximum likelihood fit in the bin $17.0 < q^2 < 19.0 \, \text{GeV}^2/c^4$.

	F_L	S_3	S_4	S_5	A_{FB}	S_7	S_8	S_9
F_L	1.00	-0.04	0.05	0.03	0.05	-0.04	-0.01	0.08
S_3		1.00	-0.05	-0.00	0.05	0.01	0.01	-0.01
S_4			1.00	-0.05	-0.11	-0.02	-0.01	0.05
S_5				1.00	-0.07	-0.01	-0.02	-0.04
A_{FB}					1.00	0.02	-0.02	-0.04
S_7						1.00	0.04	-0.01
S_8							1.00	-0.03
S_9								1.00

Table 18. Correlation matrix for the *CP*-averaged observables from the maximum likelihood fit in the bin $1.1 < q^2 < 6.0 \, \text{GeV}^2/c^4$.

	F_L	S_3	S_4	S_5	A_{FB}	S_7	S_8	S_9
F_L	1.00	0.17	-0.03	-0.02	-0.39	0.01	-0.00	0.11
S_3		1.00	-0.15	-0.19	0.05	-0.02	-0.04	-0.02
S_4			1.00	0.06	-0.12	0.03	0.14	0.01
S_5				1.00	-0.12	0.12	0.04	0.02
A_{FB}					1.00	0.00	-0.02	-0.01
S_7						1.00	0.24	-0.19
S_8							1.00	-0.13
S_9								1.00

Table 19. Correlation matrix for the *CP*-averaged observables from the maximum likelihood fit in the bin $15.0 < q^2 < 19.0 \, \text{GeV}^2/c^4$.

D Correlation matrices for the *CP*-asymmetric observables from the maximum likelihood fit

Correlation matrices between $F_{\rm L}$ and the *CP*-asymmetric observables in the different q^2 bins are provided in tables 20–29 for the likelihood fit.

	$F_{\rm L}$	A_3	A_4	A_5	A_{6s}	A_7	A_8	A_9
$F_{\rm L}$	1.00	-0.00	0.02	0.01	-0.07	-0.01	-0.01	-0.03
A_3		1.00	-0.04	-0.07	0.00	-0.03	0.02	-0.05
A_4			1.00	0.05	-0.08	0.02	0.09	-0.03
A_5				1.00	-0.04	0.08	0.03	0.02
A_{6s}					1.00	-0.04	-0.07	0.01
A_7						1.00	0.00	-0.14
A_8							1.00	-0.01
A_9								1.00

Table 20. Correlation matrix for the *CP*-asymmetric observables from the maximum likelihood fit in the bin $0.10 < q^2 < 0.98 \, {\rm GeV}^2/c^4$.

	$F_{\rm L}$	A_3	A_4	A_5	A_{6s}	A_7	A_8	A_9
$F_{\rm L}$	1.00	0.07	-0.14	-0.06	-0.04	0.06	-0.04	-0.10
A_3		1.00	-0.05	-0.11	0.01	-0.04	0.05	-0.05
A_4			1.00	0.09	-0.26	0.03	-0.15	0.10
A_5				1.00	0.03	0.03	0.06	0.01
A_{6s}					1.00	0.10	0.11	0.01
A_7						1.00	0.19	0.12
A_8							1.00	0.03
A_9								1.00

Table 21. Correlation matrix for the *CP*-asymmetric observables from the maximum likelihood fit in the bin $1.1 < q^2 < 2.5 \, {\rm GeV}^2/c^4$.

	$F_{\rm L}$	A_3	A_4	A_5	A_{6s}	A_7	A_8	A_9
$F_{\rm L}$	1.00	0.13	-0.04	0.07	0.10	-0.08	0.08	0.11
A_3		1.00	0.19	-0.00	-0.07	-0.03	0.09	0.11
A_4			1.00	0.21	-0.12	0.02	0.13	0.09
A_5				1.00	0.11	0.08	0.01	0.06
A_{6s}					1.00	-0.05	-0.28	-0.05
A_7						1.00	0.31	-0.03
A_8							1.00	0.10
A_9								1.00

Table 22. Correlation matrix for the *CP*-asymmetric observables from the maximum likelihood fit in the bin $2.5 < q^2 < 4.0 \, {\rm GeV}^2/c^4$.

	$F_{\rm L}$	A_3	A_4	A_5	A_{6s}	A_7	A_8	A_9
$F_{\rm L}$	1.00	0.03	0.02	0.03	0.01	0.05	0.08	0.01
A_3		1.00	0.08	0.19	0.10	-0.16	0.06	-0.08
A_4			1.00	0.06	-0.01	-0.01	-0.01	-0.03
A_5				1.00	0.08	0.00	0.01	-0.12
A_{6s}					1.00	-0.12	0.06	-0.05
A_7						1.00	0.05	-0.01
A_8							1.00	0.13
A_9								1.00

Table 23. Correlation matrix for the *CP*-asymmetric observables from the maximum likelihood fit in the bin $4.0 < q^2 < 6.0\,\mathrm{GeV}^2/c^4$.

	$F_{\rm L}$	A_3	A_4	A_5	A_{6s}	A_7	A_8	A_9
$F_{\rm L}$	1.00	-0.07	-0.06	0.03	-0.03	-0.01	0.02	-0.15
A_3		1.00	0.08	0.12	-0.07	-0.01	0.01	-0.06
A_4			1.00	-0.07	0.08	0.01	-0.00	0.05
A_5				1.00	0.13	-0.03	0.01	0.01
A_{6s}					1.00	0.02	0.05	-0.06
A_7						1.00	-0.11	0.12
A_8							1.00	0.06
A_9								1.00

Table 24. Correlation matrix for the *CP*-asymmetric observables from the maximum likelihood fit in the bin $6.0 < q^2 < 8.0\,\mathrm{GeV}^2/c^4$.

	$F_{\rm L}$	A_3	A_4	A_5	A_{6s}	A_7	A_8	A_9
$F_{\rm L}$	1.00	-0.09	-0.01	0.00	-0.01	-0.02	0.01	0.06
A_3		1.00	0.05	0.19	0.02	-0.16	0.08	0.11
A_4			1.00	-0.26	0.20	-0.10	0.02	-0.01
A_5				1.00	0.11	-0.03	-0.06	0.04
A_{6s}					1.00	-0.06	0.11	-0.02
A_7						1.00	-0.22	0.19
A_8							1.00	0.04
A_9								1.00

Table 25. Correlation matrix for the *CP*-asymmetric observables from the maximum likelihood fit in the bin $11.0 < q^2 < 12.5\,\mathrm{GeV}^2/c^4$.

	F_L	A_3	A_4	A_5	A_{6s}	A_7	A_8	A_9
F_L	1.00	0.04	0.02	0.02	0.06	-0.07	0.04	-0.07
A_3		1.00	0.05	0.16	0.02	-0.00	-0.02	0.04
A_4			1.00	-0.25	0.16	-0.07	0.10	-0.01
A_5				1.00	0.12	0.09	-0.07	-0.07
A_{6s}					1.00	-0.01	0.04	0.03
A_7						1.00	-0.17	0.11
A_8							1.00	0.08
A_9								1.00

Table 26. Correlation matrix for the *CP*-asymmetric observables from the maximum likelihood fit in the bin $15.0 < q^2 < 17.0\,\mathrm{GeV}^2/c^4$.

	F_L	A_3	A_4	A_5	A_{6s}	A_7	A_8	A_9
F_L	1.00	-0.00	0.03	-0.00	0.09	-0.04	0.07	-0.03
A_3		1.00	0.14	0.18	-0.01	-0.07	-0.05	-0.06
A_4			1.00	-0.09	0.10	-0.11	0.04	-0.09
A_5				1.00	0.11	0.04	-0.11	-0.04
A_{6s}					1.00	-0.01	-0.08	-0.08
A_7						1.00	-0.03	0.14
A_8							1.00	0.01
A_9								1.00

Table 27. Correlation matrix for the *CP*-asymmetric observables from the maximum likelihood fit in the bin $17.0 < q^2 < 19.0\,\mathrm{GeV}^2/c^4$.

	F_L	A_3	A_4	A_5	A_{6s}	A_7	A_8	A_9
F_L	1.00	0.04	0.00	-0.00	-0.01	0.01	0.04	-0.01
A_3		1.00	0.05	0.04	0.04	-0.08	0.05	0.01
A_4			1.00	0.12	-0.09	-0.02	0.03	0.03
A_5				1.00	0.05	0.05	-0.01	0.01
A_{6s}					1.00	-0.02	0.05	-0.03
A_7						1.00	0.18	0.00
A_8							1.00	0.06
A_9								1.00

Table 28. Correlation matrix for the *CP*-asymmetric observables from the maximum likelihood fit in the bin $1.1 < q^2 < 6.0\,\mathrm{GeV}^2/c^4$.

	F_L	A_3	A_4	A_5	A_{6s}	A_7	A_8	A_9
F_L	1.00	0.02	0.01	-0.01	0.06	-0.04	0.04	-0.04
A_3		1.00	0.07	0.17	0.03	-0.02	-0.02	0.02
A_4			1.00	-0.19	0.13	-0.06	0.06	-0.03
A_5				1.00	0.11	0.06	-0.07	-0.05
A_{6s}					1.00	-0.00	-0.01	-0.01
A_7						1.00	-0.11	0.13
A_8							1.00	0.05
A_9								1.00

Table 29. Correlation matrix for the *CP*-asymmetric observables from the maximum likelihood fit in the bin $15.0 < q^2 < 19.0\,\mathrm{GeV}^2/c^4$.

E Correlation matrices for the optimised angular observables from the maximum likelihood fit

Correlation matrices between $F_{\rm L}$ and the optimised $P_i^{(\prime)}$ basis of observables in the different q^2 bins are provided in tables 30–39 for the likelihood fit.

	$F_{\rm L}$	P_1	P_2	P_3	P_4'	P_5'	P_6'	P_8'
$F_{\rm L}$	1.00	0.02	0.03	0.00	-0.07	-0.12	-0.03	0.01
P_1		1.00	-0.00	0.04	0.01	0.09	-0.07	-0.02
P_2			1.00	-0.02	0.11	0.04	0.03	-0.08
P_3				1.00	-0.02	-0.04	-0.11	-0.01
P_4'					1.00	0.09	0.00	0.07
P_5'						1.00	-0.00	-0.00
P_6'							1.00	0.01
P_8'								1.00

Table 30. Correlation matrix for the optimised angular observables from the maximum likelihood fit in the bin $0.10 < q^2 < 0.98\,{\rm GeV}^2/c^4$.

	$F_{\rm L}$	P_1	P_2	P_3	P_4'	P_5'	P_6'	P_8'
$F_{\rm L}$	1.00	-0.11	-0.48	0.23	0.03	0.15	-0.17	-0.09
P_1		1.00	0.06	-0.13	-0.05	0.01	0.15	0.11
P_2			1.00	-0.02	-0.03	-0.19	0.06	-0.04
P_3				1.00	-0.01	0.24	-0.26	0.01
P_4'					1.00	-0.22	-0.00	-0.05
P_5'						1.00	-0.13	-0.04
P_6'							1.00	-0.10
P_8'								1.00

Table 31. Correlation matrix for the optimised angular observables from the maximum likelihood fit in the bin $1.1 < q^2 < 2.5\,{\rm GeV}^2/c^4$.

	$F_{\rm L}$	P_1	P_2	P_3	P_4'	P_5'	P_6'	P_8'
$F_{\rm L}$	1.00	0.23	-0.79	0.61	-0.60	-0.05	0.29	0.06
P_1		1.00	-0.14	0.19	-0.20	0.08	0.06	0.02
P_2			1.00	-0.53	0.43	0.04	-0.23	-0.11
P_3				1.00	-0.41	-0.11	0.21	0.04
P_4'					1.00	-0.12	-0.21	0.06
P_5'						1.00	0.03	-0.03
P_6'							1.00	0.08
P_8'								1.00

Table 32. Correlation matrix for the optimised angular observables from the maximum likelihood fit in the bin $2.5 < q^2 < 4.0\,{\rm GeV}^2/c^4$.

	F_{L}	P_1	P_2	P_3	P_4'	P_5'	P_6'	P_8'
F_{L}	1.00	0.04	0.02	0.06	0.02	0.06	-0.10	0.09
P_1		1.00	0.09	0.12	-0.04	-0.03	-0.11	0.00
P_2			1.00	0.03	-0.09	-0.05	0.02	0.07
P_3				1.00	-0.04	0.04	0.14	-0.02
P_4'					1.00	0.10	-0.02	-0.04
P_5'						1.00	-0.03	-0.01
P_6'							1.00	0.06
P_8'								1.00

Table 33. Correlation matrix for the optimised angular observables from the maximum likelihood fit in the bin $4.0 < q^2 < 6.0 \, \mathrm{GeV}^2/c^4$.

	F_{L}	P_1	P_2	P_3	P_4'	P_5'	P_6'	P_8'
F_{L}	1.00	-0.05	0.11	0.11	-0.01	-0.03	-0.09	-0.03
P_1		1.00	0.02	0.06	-0.16	-0.23	0.03	0.02
P_2			1.00	0.01	-0.11	-0.16	-0.05	0.04
P_3				1.00	-0.01	0.03	0.05	0.10
P_4'					1.00	-0.13	-0.01	-0.11
P_5'						1.00	-0.13	-0.01
P_6'							1.00	0.10
P_8'								1.00

Table 34. Correlation matrix for the optimised angular observables from the maximum likelihood fit in the bin $6.0 < q^2 < 8.0 \, \mathrm{GeV}^2/c^4$.

	F_{L}	P_1	P_2	P_3	P_4'	P_5'	P_6'	P_8'
F_{L}	1.00	-0.12	0.13	-0.02	0.03	-0.02	0.03	0.05
P_1		1.00	-0.13	0.03	0.04	-0.35	-0.05	0.05
P_2			1.00	-0.12	0.10	-0.01	0.01	-0.04
P_3				1.00	0.08	0.24	0.19	0.09
P_4'					1.00	-0.02	-0.05	-0.12
P_5'						1.00	-0.04	-0.09
P_6'							1.00	0.27
P_8'								1.00

Table 35. Correlation matrix for the optimised angular observables from the maximum likelihood fit in the bin $11.0 < q^2 < 12.5 \, \mathrm{GeV}^2/c^4$.

	F_L	P_1	P_2	P_3	P_4'	P_5'	P_6'	P_8'
F_L	1.00	0.06	0.19	−0.12	0.07	0.25	−0.05	−0.07
P_1		1.00	0.16	−0.07	−0.06	−0.04	−0.04	−0.04
P_2			1.00	−0.01	−0.22	−0.12	0.04	−0.07
P_3				1.00	−0.07	−0.07	0.23	0.11
P_4'					1.00	0.28	−0.06	0.18
P_5'						1.00	0.10	−0.02
P_6'							1.00	0.25
P_8'								1.00

Table 36. Correlation matrix for the optimised angular observables from the maximum likelihood fit in the bin $15.0 < q^2 < 17.0 \, \text{GeV}^2/c^4$.

	F_L	P_1	P_2	P_3	P_4'	P_5'	P_6'	P_8'
F_L	1.00	−0.14	0.14	0.03	0.20	0.21	0.05	0.07
P_1		1.00	−0.05	0.07	−0.18	−0.41	−0.07	−0.06
P_2			1.00	0.00	−0.13	−0.06	0.01	−0.05
P_3				1.00	0.05	0.01	0.16	0.12
P_4'					1.00	0.14	0.03	0.19
P_5'						1.00	0.05	0.02
P_6'							1.00	0.34
P_8'								1.00

Table 37. Correlation matrix for the optimised angular observables from the maximum likelihood fit in the bin $17.0 < q^2 < 19.0 \, \text{GeV}^2/c^4$.

	F_L	P_1	P_2	P_3	P_4'	P_5'	P_6'	P_8'
F_L	1.00	−0.01	−0.20	0.07	−0.03	0.01	−0.08	0.00
P_1		1.00	0.05	0.00	−0.05	−0.00	0.01	0.01
P_2			1.00	0.03	−0.10	−0.07	0.04	−0.02
P_3				1.00	−0.05	0.04	0.00	0.03
P_4'					1.00	−0.05	−0.02	−0.01
P_5'						1.00	−0.01	−0.02
P_6'							1.00	0.04
P_8'								1.00

Table 38. Correlation matrix for the optimised angular observables from the maximum likelihood fit in the bin $1.1 < q^2 < 6.0 \, \text{GeV}^2/c^4$.

	F_L	P_1	P_2	P_3	P_4'	P_5'	P_6'	P_8'
F_L	1.00	−0.03	0.14	−0.05	0.11	0.15	−0.01	−0.01
P_1		1.00	0.13	0.04	−0.14	−0.19	−0.02	−0.04
P_2			1.00	−0.05	−0.13	−0.11	0.01	−0.03
P_3				1.00	−0.02	−0.03	0.19	0.13
P_4'					1.00	0.08	0.03	0.14
P_5'						1.00	0.11	0.04
P_6'							1.00	0.24
P_8'								1.00

Table 39. Correlation matrix for the optimised angular observables from the maximum likelihood fit in the bin $15.0 < q^2 < 19.0 \, \text{GeV}^2/c^4$.

F Correlation matrices for the *CP*-averaged observables from the method of moments

Correlation matrices between the *CP*-averaged observables in the different q^2 bins are in tables 40–54 for the moment analysis. The correlations are determined by a bootstrapping technique.

	F_L	S_3	S_4	S_5	A_{FB}	S_7	S_8	S_9
F_L	1.00	0.02	0.00	−0.05	0.23	0.02	−0.01	0.05
S_3		1.00	0.04	0.09	−0.01	0.01	−0.04	0.05
S_4			1.00	−0.24	−0.05	−0.07	0.06	0.03
S_5				1.00	0.12	0.00	−0.09	−0.02
A_{FB}					1.00	0.09	−0.07	−0.04
S_7						1.00	−0.09	0.10
S_8							1.00	0.03
S_9								1.00

Table 40. Correlation matrix for the *CP*-averaged observables obtained for the method of moments in the bin $0.10 < q^2 < 0.98\,\mathrm{GeV}^2/c^4$.

	F_L	S_3	S_4	S_5	A_{FB}	S_7	S_8	S_9
F_L	1.00	−0.02	0.06	0.16	−0.05	−0.03	−0.04	0.09
S_3		1.00	−0.01	0.03	0.08	0.10	−0.03	0.08
S_4			1.00	0.00	−0.03	−0.13	0.00	−0.06
S_5				1.00	−0.07	−0.05	−0.11	−0.06
A_{FB}					1.00	0.04	−0.06	−0.10
S_7						1.00	−0.05	0.01
S_8							1.00	−0.01
S_9								1.00

Table 41. Correlation matrix for the *CP*-averaged observables obtained for the method of moments in the bin $1.1 < q^2 < 2.0\,\mathrm{GeV}^2/c^4$.

	F_L	S_3	S_4	S_5	A_{FB}	S_7	S_8	S_9
F_L	1.00	−0.12	−0.14	−0.04	0.11	−0.18	0.04	0.01
S_3		1.00	−0.09	0.06	0.04	0.08	−0.04	−0.01
S_4			1.00	−0.08	0.00	0.03	−0.05	−0.06
S_5				1.00	−0.10	−0.08	0.04	−0.08
A_{FB}					1.00	−0.01	−0.10	0.04
S_7						1.00	−0.12	0.01
S_8							1.00	−0.07
S_9								1.00

Table 42. Correlation matrix for the *CP*-averaged observables obtained for the method of moments in the bin $2.0 < q^2 < 3.0\,\mathrm{GeV}^2/c^4$.

	F_{L}	S_3	S_4	S_5	A_{FB}	S_7	S_8	S_9
F_{L}	1.00	0.10	-0.01	-0.03	0.01	0.01	-0.16	0.05
S_3		1.00	-0.01	-0.04	0.03	-0.08	-0.04	-0.11
S_4			1.00	0.18	0.05	0.01	-0.05	-0.02
S_5				1.00	0.00	-0.01	0.02	-0.03
A_{FB}					1.00	0.04	-0.03	-0.01
S_7						1.00	0.18	-0.08
S_8							1.00	-0.03
S_9								1.00

Table 43. Correlation matrix for the *CP*-averaged observables obtained for the method of moments in the bin $3.0 < q^2 < 4.0 \,\mathrm{GeV}^2/c^4$.

	F_{L}	S_3	S_4	S_5	A_{FB}	S_7	S_8	S_9
F_{L}	1.00	-0.01	0.03	-0.12	-0.02	-0.07	0.04	0.10
S_3		1.00	-0.10	-0.11	0.03	0.08	-0.12	0.07
S_4			1.00	0.15	-0.03	-0.07	0.21	0.04
S_5				1.00	-0.03	0.10	-0.02	-0.09
A_{FB}					1.00	0.11	-0.15	0.00
S_7						1.00	0.07	-0.07
S_8							1.00	0.0
S_9								1.00

Table 44. Correlation matrix for the *CP*-averaged observables obtained for the method of moments in the bin $4.0 < q^2 < 5.0 \,\mathrm{GeV}^2/c^4$.

	F_{L}	S_3	S_4	S_5	A_{FB}	S_7	S_8	S_9
F_{L}	1.00	-0.03	-0.06	-0.04	-0.01	-0.03	-0.09	-0.02
S_3		1.00	-0.01	-0.06	-0.11	-0.05	0.02	0.11
S_4			1.00	0.10	-0.03	0.08	0.02	0.01
S_5				1.00	-0.08	-0.03	0.06	0.07
A_{FB}					1.00	0.01	0.00	0.00
S_7						1.00	0.07	-0.09
S_8							1.00	-0.13
S_9								1.00

Table 45. Correlation matrix for the *CP*-averaged observables obtained for the method of moments in the bin $5.0 < q^2 < 6.0 \,\mathrm{GeV}^2/c^4$.

	F_{L}	S_3	S_4	S_5	A_{FB}	S_7	S_8	S_9
F_{L}	1.00	0.00	-0.24	-0.14	-0.04	0.08	0.07	-0.03
S_3		1.00	-0.09	-0.17	-0.08	0.02	-0.04	-0.02
S_4			1.00	0.13	-0.12	-0.03	-0.01	-0.04
S_5				1.00	-0.07	-0.01	-0.01	-0.04
A_{FB}					1.00	0.02	-0.01	-0.05
S_7						1.00	0.21	-0.11
S_8							1.00	-0.06
S_9								1.00

Table 46. Correlation matrix for the *CP*-averaged observables obtained for the method of moments in the bin $6.0 < q^2 < 7.0 \,\mathrm{GeV}^2/c^4$.

	F_L	S_3	S_4	S_5	A_{FB}	S_7	S_8	S_9
F_L	1.00	0.07	-0.13	-0.22	-0.08	-0.07	-0.01	0.09
S_3		1.00	-0.12	-0.15	0.07	0.05	0.02	-0.01
S_4			1.00	0.15	-0.09	-0.05	0.06	0.00
S_5				1.00	-0.15	0.13	0.00	0.03
A_{FB}					1.00	-0.02	-0.16	0.04
S_7						1.00	0.07	-0.11
S_8							1.00	-0.07
S_9								1.00

Table 47. Correlation matrix for the *CP*-averaged observables obtained for the method of moments in the bin $7.0 < q^2 < 8.0\,\mathrm{GeV}^2/c^4$.

	F_L	S_3	S_4	S_5	A_{FB}	S_7	S_8	S_9
F_L	1.00	0.15	0.16	0.03	-0.34	-0.05	-0.12	-0.01
S_3		1.00	-0.06	-0.21	-0.06	0.04	0.00	-0.02
S_4			1.00	0.19	-0.19	-0.11	-0.15	-0.04
S_5				1.00	-0.11	-0.13	-0.10	-0.09
A_{FB}					1.00	0.03	-0.03	-0.04
S_7						1.00	0.24	-0.03
S_8							1.00	-0.10
S_9								1.00

Table 48. Correlation matrix for the *CP*-averaged observables obtained for the method of moments in the bin $11.00 < q^2 < 11.75\,\mathrm{GeV}^2/c^4$.

	F_L	S_3	S_4	S_5	A_{FB}	S_7	S_8	S_9
F_L	1.00	0.04	-0.05	-0.01	-0.17	-0.08	0.05	0.00
S_3		1.00	-0.13	-0.14	0.00	0.02	0.00	0.05
S_4			1.00	0.16	-0.22	0.10	0.18	-0.02
S_5				1.00	-0.17	0.16	0.08	-0.10
A_{FB}					1.00	-0.08	-0.12	0.07
S_7						1.00	0.16	-0.16
S_8							1.00	-0.08
S_9								1.00

Table 49. Correlation matrix for the *CP*-averaged observables obtained for the method of moments in the bin $11.75 < q^2 < 12.50\,\mathrm{GeV}^2/c^4$.

	F_L	S_3	S_4	S_5	A_{FB}	S_7	S_8	S_9
F_L	1.00	0.05	-0.01	-0.09	-0.34	0.01	0.03	-0.01
S_3		1.00	-0.15	-0.29	0.06	-0.03	0.02	-0.09
S_4			1.00	0.33	-0.06	-0.02	-0.17	-0.01
S_5				1.00	-0.10	-0.13	-0.02	-0.05
A_{FB}					1.00	-0.01	-0.03	-0.04
S_7						1.00	0.12	-0.10
S_8							1.00	-0.12
S_9								1.00

Table 50. Correlation matrix for the *CP*-averaged observables obtained for the method of moments in the bin $15.0 < q^2 < 16.0\,\mathrm{GeV}^2/c^4$.

	F_L	S_3	S_4	S_5	A_{FB}	S_7	S_8	S_9
F_L	1.00	0.16	−0.02	0.01	−0.33	0.16	0.03	−0.01
S_3		1.00	−0.12	−0.13	0.04	0.05	−0.01	−0.03
S_4			1.00	0.21	−0.20	0.08	−0.02	0.06
S_5				1.00	−0.14	0.02	0.07	0.20
A_{FB}					1.00	−0.05	0.01	−0.02
S_7						1.00	0.15	−0.13
S_8							1.00	−0.08
S_9								1.00

Table 51. Correlation matrix for the *CP*-averaged observables obtained for the method of moments in the bin $16.0 < q^2 < 17.0 \, \text{GeV}^2/c^4$.

	F_L	S_3	S_4	S_5	A_{FB}	S_7	S_8	S_9
F_L	1.00	0.06	−0.08	0.05	−0.21	−0.05	0.06	0.00
S_3		1.00	−0.12	−0.19	0.03	0.09	0.01	−0.08
S_4			1.00	0.14	−0.07	0.05	−0.12	0.00
S_5				1.00	−0.06	−0.17	0.07	0.06
A_{FB}					1.00	0.01	0.03	0.03
S_7						1.00	0.11	−0.20
S_8							1.00	−0.05
S_9								1.00

Table 52. Correlation matrix for the *CP*-averaged observables obtained for the method of moments in the bin $17.0 < q^2 < 18.0 \, \text{GeV}^2/c^4$.

	F_L	S_3	S_4	S_5	A_{FB}	S_7	S_8	S_9
F_L	1.00	0.20	−0.21	−0.16	−0.21	0.01	0.10	0.02
S_3		1.00	−0.18	−0.21	−0.03	0.00	0.05	−0.02
S_4			1.00	0.36	−0.18	0.03	0.00	0.00
S_5				1.00	−0.24	−0.01	−0.03	0.02
A_{FB}					1.00	−0.04	0.02	0.05
S_7						1.00	0.19	−0.17
S_8							1.00	−0.01
S_9								1.00

Table 53. Correlation matrix for the *CP*-averaged observables obtained for the method of moments in the bin $18.0 < q^2 < 19.0 \, \text{GeV}^2/c^4$.

	F_L	S_3	S_4	S_5	A_{FB}	S_7	S_8	S_9
F_L	1.00	0.11	−0.07	−0.04	−0.28	0.04	0.04	−0.01
S_3		1.00	−0.15	−0.21	0.04	0.02	0.01	−0.06
S_4			1.00	0.24	−0.11	0.04	−0.07	0.02
S_5				1.00	−0.11	−0.08	0.03	0.07
A_{FB}					1.00	−0.02	0.00	0.00
S_7						1.00	0.14	−0.15
S_8							1.00	−0.07
S_9								1.00

Table 54. Correlation matrix for the *CP*-averaged observables obtained for the method of moments in the bin $15.0 < q^2 < 19.0 \, \text{GeV}^2/c^4$.

Correlation matrices between the *CP* asymmetries in the different q^2 bins are provided in tables 55–69 for the moment analysis. The correlations are determined by a bootstrapping technique.

	A_3	A_4	A_5	A_{6s}	A_7	A_8	A_9
A_3	1.00	0.04	0.09	−0.02	0.01	−0.04	0.05
A_4		1.00	−0.24	−0.07	−0.08	0.07	0.02
A_5			1.00	0.07	0.00	−0.07	−0.01
A_{6s}				1.00	0.08	−0.11	0.00
A_7					1.00	−0.09	0.12
A_8						1.00	0.01
A_9							1.00

Table 55. Correlation matrix for the *CP*-asymmetric observables obtained for the method of moments in the bin $0.10 < q^2 < 0.98\,\mathrm{GeV}^2/c^4$.

	A_3	A_4	A_5	A_{6s}	A_7	A_8	A_9
A_3	1.00	−0.01	0.04	0.06	0.12	−0.05	0.08
A_4		1.00	−0.06	0.04	−0.16	0.04	−0.10
A_5			1.00	−0.05	0.01	−0.11	−0.07
A_{6s}				1.00	−0.06	−0.07	−0.09
A_7					1.00	−0.12	0.10
A_8						1.00	−0.04
A_9							1.00

Table 56. Correlation matrix for the *CP*-asymmetric observables obtained for the method of moments in the bin $1.1 < q^2 < 2.0\,\mathrm{GeV}^2/c^4$.

	A_3	A_4	A_5	A_{6s}	A_7	A_8	A_9
A_3	1.00	−0.10	0.06	0.03	0.07	−0.04	−0.02
A_4		1.00	−0.07	0.07	0.06	−0.06	−0.05
A_5			1.00	−0.10	−0.07	0.04	−0.07
A_{6s}				1.00	−0.03	−0.11	0.04
A_7					1.00	−0.15	0.02
A_8						1.00	−0.07
A_9							1.00

Table 57. Correlation matrix for the *CP*-asymmetric observables obtained for the method of moments in the bin $2.0 < q^2 < 3.0\,\mathrm{GeV}^2/c^4$.

	A_3	A_4	A_5	A_{6s}	A_7	A_8	A_9
A_3	1.00	0.00	-0.04	0.03	-0.12	-0.05	-0.06
A_4		1.00	0.18	0.06	0.01	-0.05	-0.01
A_5			1.00	0.01	-0.01	0.01	-0.01
A_{6s}				1.00	0.03	-0.05	0.00
A_7					1.00	0.18	-0.05
A_8						1.00	-0.03
A_9							1.00

Table 58. Correlation matrix for the *CP*-asymmetric observables obtained for the method of moments in the bin $3.0 < q^2 < 4.0 \, \text{GeV}^2/c^4$.

	A_3	A_4	A_5	A_{6s}	A_7	A_8	A_9
A_3	1.00	-0.12	-0.11	0.02	0.06	-0.12	0.06
A_4		1.00	0.17	-0.03	-0.06	0.19	0.03
A_5			1.00	-0.04	0.14	-0.06	-0.09
A_{6s}				1.00	0.10	-0.14	0.00
A_7					1.00	0.04	-0.08
A_8						1.00	0.02
A_9							1.00

Table 59. Correlation matrix for the *CP*-asymmetric observables obtained for the method of moments in the bin $4.0 < q^2 < 5.0 \, \text{GeV}^2/c^4$.

	A_3	A_4	A_5	A_{6s}	A_7	A_8	A_9
A_3	1.00	-0.03	-0.07	-0.09	-0.04	0.03	0.11
A_4		1.00	0.10	-0.03	0.08	0.07	0.03
A_5			1.00	-0.08	-0.04	0.07	0.07
A_{6s}				1.00	0.01	-0.01	-0.01
A_7					1.00	0.07	-0.09
A_8						1.00	-0.12
A_9							1.00

Table 60. Correlation matrix for the *CP*-asymmetric observables obtained for the method of moments in the bin $5.0 < q^2 < 6.0 \, \text{GeV}^2/c^4$.

	A_3	A_4	A_5	A_{6s}	A_7	A_8	A_9
A_3	1.00	-0.08	-0.15	-0.09	0.02	-0.05	-0.02
A_4		1.00	0.21	-0.15	-0.03	-0.04	-0.04
A_5			1.00	-0.10	-0.02	-0.03	-0.05
A_{6s}				1.00	0.03	0.00	-0.05
A_7					1.00	0.22	-0.11
A_8						1.00	-0.05
A_9							1.00

Table 61. Correlation matrix for the *CP*-asymmetric observables obtained for the method of moments in the bin $6.0 < q^2 < 7.0 \, \text{GeV}^2/c^4$.

	A_3	A_4	A_5	A_{6s}	A_7	A_8	A_9
A_3	1.00	−0.07	−0.11	0.04	0.06	0.04	−0.01
A_4		1.00	0.18	−0.07	−0.02	0.05	0.01
A_5			1.00	−0.11	0.14	−0.02	0.02
A_{6s}				1.00	−0.03	−0.14	0.07
A_7					1.00	0.07	−0.11
A_8						1.00	−0.08
A_9							1.00

Table 62. Correlation matrix for the *CP*-asymmetric observables obtained for the method of moments in the bin $7.0 < q^2 < 8.0\,\mathrm{GeV}^2/c^4$.

	A_3	A_4	A_5	A_{6s}	A_7	A_8	A_9
A_3	1.00	−0.08	−0.20	−0.10	0.06	0.03	−0.02
A_4		1.00	0.16	−0.14	−0.10	−0.15	−0.04
A_5			1.00	−0.09	−0.11	−0.09	−0.10
A_{6s}				1.00	−0.02	−0.07	−0.05
A_7					1.00	0.25	−0.02
A_8						1.00	−0.09
A_9							1.00

Table 63. Correlation matrix for the *CP*-asymmetric observables obtained for the method of moments in the bin $11.00 < q^2 < 11.75\,\mathrm{GeV}^2/c^4$.

	A_3	A_4	A_5	A_{6s}	A_7	A_8	A_9
A_3	1.00	−0.12	−0.16	0.01	0.01	0.03	0.06
A_4		1.00	0.17	−0.21	0.08	0.15	−0.05
A_5			1.00	−0.17	0.14	0.12	−0.09
A_{6s}				1.00	−0.07	−0.17	0.05
A_7					1.00	0.19	−0.15
A_8						1.00	−0.08
A_9							1.00

Table 64. Correlation matrix for the *CP*-asymmetric observables obtained for the method of moments in the bin $11.75 < q^2 < 12.50\,\mathrm{GeV}^2/c^4$.

	A_3	A_4	A_5	A_{6s}	A_7	A_8	A_9
A_3	1.00	−0.14	−0.26	0.05	−0.02	0.02	−0.10
A_4		1.00	0.36	−0.12	−0.02	−0.17	0.00
A_5			1.00	−0.16	−0.12	−0.02	−0.04
A_{6s}				1.00	−0.02	−0.03	−0.05
A_7					1.00	0.13	−0.09
A_8						1.00	−0.12
A_9							1.00

Table 65. Correlation matrix for the *CP*-asymmetric observables obtained for the method of moments in the bin $15.0 < q^2 < 16.0\,\mathrm{GeV}^2/c^4$.

	A_3	A_4	A_5	A_{6s}	A_7	A_8	A_9
A_3	1.00	−0.08	−0.09	0.00	0.01	−0.03	−0.04
A_4		1.00	0.21	−0.22	0.05	−0.02	0.06
A_5			1.00	−0.14	−0.01	0.05	0.19
A_{6s}				1.00	0.02	0.02	−0.01
A_7					1.00	0.15	−0.13
A_8						1.00	−0.08
A_9							1.00

Table 66. Correlation matrix for the *CP*-asymmetric observables obtained for the method of moments in the bin $16.0 < q^2 < 17.0 \, \mathrm{GeV}^2/c^4$.

	A_3	A_4	A_5	A_{6s}	A_7	A_8	A_9
A_3	1.00	−0.10	−0.16	−0.01	0.00	0.00	−0.06
A_4		1.00	0.18	−0.10	0.07	−0.14	0.03
A_5			1.00	−0.10	−0.16	0.05	0.09
A_{6s}				1.00	0.00	0.05	0.01
A_7					1.00	0.09	−0.20
A_8						1.00	−0.06
A_9							1.00

Table 67. Correlation matrix for the *CP*-asymmetric observables obtained for the method of moments in the bin $17.0 < q^2 < 18.0 \, \mathrm{GeV}^2/c^4$.

	A_3	A_4	A_5	A_{6s}	A_7	A_8	A_9
A_3	1.00	−0.18	−0.20	−0.06	−0.01	0.04	−0.03
A_4		1.00	0.28	−0.10	−0.02	0.01	0.07
A_5			1.00	−0.15	−0.05	0.00	0.04
A_{6s}				1.00	−0.01	−0.01	0.03
A_7					1.00	0.21	−0.19
A_8						1.00	−0.03
A_9							1.00

Table 68. Correlation matrix for the *CP*-asymmetric observables obtained for the method of moments in the bin $18.0 < q^2 < 19.0 \, \mathrm{GeV}^2/c^4$.

	A_3	A_4	A_5	A_{6s}	A_7	A_8	A_9
A_3	1.00	−0.12	−0.18	0.00	0.01	0.01	−0.05
A_4		1.00	0.26	−0.14	0.02	−0.08	0.03
A_5			1.00	−0.13	−0.09	0.02	0.07
A_{6s}				1.00	0.0	0.01	−0.01
A_7					1.00	0.14	−0.15
A_8						1.00	−0.07
A_9							1.00

Table 69. Correlation matrix for the *CP*-asymmetric observables obtained for the method of moments in the bin $15.0 < q^2 < 19.0 \, \mathrm{GeV}^2/c^4$.

H Correlation matrices for the optimised observables from the method of moments

Correlation matrices between the optimised asymmetries in the different q^2 bins are provided in tables 70–84 for the moment analysis. The correlations are determined by a bootstrapping technique.

	$F_{\rm L}$	P_1	P_2	P_3	P_4'	P_5'	P_6'	P_8'
$F_{\rm L}$	1.00	0.00	0.12	0.09	-0.04	-0.23	-0.04	-0.08
P_1		1.00	-0.02	-0.05	0.04	0.08	0.01	-0.04
P_2			1.00	0.06	-0.05	0.11	0.08	-0.08
P_3				1.00	-0.04	-0.01	-0.10	-0.03
P_4'					1.00	-0.22	-0.07	0.07
P_5'						1.00	0.01	-0.07
P_6'							1.00	-0.08
P_8'								1.00

Table 70. Correlation matrix for the optimised angular observables obtained for the method of moments in the bin $0.10 < q^2 < 0.98\,{\rm GeV}^2/c^4$.

	$F_{\rm L}$	P_1	P_2	P_3	P_4'	P_5'	P_6'	P_8'
$F_{\rm L}$	1.00	0.02	-0.09	0.03	0.21	0.44	-0.35	-0.17
P_1		1.00	-0.17	0.03	0.01	0.08	0.04	-0.04
P_2			1.00	-0.31	-0.17	-0.40	0.31	0.11
P_3				1.00	0.10	0.18	-0.10	-0.04
P_4'					1.00	0.16	-0.24	-0.07
P_5'						1.00	-0.32	-0.21
P_6'							1.00	0.09
P_8'								1.00

Table 71. Correlation matrix for the optimised angular observables obtained for the method of moments in the bin $1.1 < q^2 < 2.0\,{\rm GeV}^2/c^4$.

	$F_{\rm L}$	P_1	P_2	P_3	P_4'	P_5'	P_6'	P_8'
$F_{\rm L}$	1.00	-0.09	-0.39	0.00	-0.45	0.20	-0.40	-0.12
P_1		1.00	0.11	0.01	-0.03	0.02	0.11	-0.01
P_2			1.00	-0.03	0.35	-0.24	0.31	0.04
P_3				1.00	0.04	0.07	-0.01	0.06
P_4'					1.00	-0.23	0.30	0.08
P_5'						1.00	-0.23	-0.03
P_6'							1.00	0.00
P_8'								1.00

Table 72. Correlation matrix for the optimised angular observables obtained for the method of moments in the bin $2.0 < q^2 < 3.0\,{\rm GeV}^2/c^4$.

	F_{L}	P_1	P_2	P_3	P_4'	P_5'	P_6'	P_8'
F_{L}	1.00	−0.23	0.08	−0.33	−0.08	−0.23	0.30	0.07
P_1		1.00	−0.11	0.38	−0.01	−0.05	−0.04	−0.03
P_2			1.00	−0.28	0.06	0.07	−0.05	−0.05
P_3				1.00	−0.03	−0.11	0.18	0.04
P_4'					1.00	0.18	−0.03	−0.06
P_5'						1.00	−0.14	−0.03
P_6'							1.00	0.21
P_8'								1.00

Table 73. Correlation matrix for the optimised angular observables obtained for the method of moments in the bin $3.0 < q^2 < 4.0 \, \mathrm{GeV}^2/c^4$.

	F_{L}	P_1	P_2	P_3	P_4'	P_5'	P_6'	P_8'
F_{L}	1.00	−0.34	−0.08	0.24	−0.27	−0.55	−0.24	0.25
P_1		1.00	0.31	−0.64	−0.14	−0.24	−0.03	0.00
P_2			1.00	−0.37	−0.13	−0.23	−0.01	−0.01
P_3				1.00	0.13	0.38	0.17	−0.13
P_4'					1.00	0.36	0.07	0.03
P_5'						1.00	0.28	−0.25
P_6'							1.00	−0.05
P_8'								1.00

Table 74. Correlation matrix for the optimised angular observables obtained for the method of moments in the bin $4.0 < q^2 < 5.0 \, \mathrm{GeV}^2/c^4$.

	F_{L}	P_1	P_2	P_3	P_4'	P_5'	P_6'	P_8'
F_{L}	1.00	−0.28	0.14	0.19	−0.25	−0.14	0.01	−0.13
P_1		1.00	−0.18	−0.21	0.08	0.00	−0.04	0.06
P_2			1.00	0.13	−0.14	−0.11	0.01	−0.04
P_3				1.00	−0.11	−0.11	0.08	0.07
P_4'					1.00	0.17	0.06	0.06
P_5'						1.00	−0.04	0.07
P_6'							1.00	0.07
P_8'								1.00

Table 75. Correlation matrix for the optimised angular observables obtained for the method of moments in the bin $5.0 < q^2 < 6.0 \, \mathrm{GeV}^2/c^4$.

	F_{L}	P_1	P_2	P_3	P_4'	P_5'	P_6'	P_8'
F_{L}	1.00	−0.21	0.20	−0.15	−0.41	−0.33	0.09	0.12
P_1		1.00	−0.13	0.06	0.02	−0.07	0.00	−0.07
P_2			1.00	0.00	−0.22	−0.16	0.05	0.02
P_3				1.00	0.12	0.10	0.09	0.04
P_4'					1.00	0.25	−0.04	−0.05
P_5'						1.00	−0.03	−0.04
P_6'							1.00	0.21
P_8'								1.00

Table 76. Correlation matrix for the optimised angular observables obtained for the method of moments in the bin $6.0 < q^2 < 7.0 \, \mathrm{GeV}^2/c^4$.

	F_L	P_1	P_2	P_3	P'_4	P'_5	P'_6	P'_8
F_L	1.00	−0.08	0.58	−0.18	−0.26	−0.41	−0.13	−0.16
P_1		1.00	−0.01	0.03	−0.08	−0.09	0.06	0.03
P_2			1.00	−0.19	−0.28	−0.45	−0.12	−0.26
P_3				1.00	0.05	0.06	0.12	0.11
P'_4					1.00	0.26	−0.01	0.13
P'_5						1.00	0.17	0.11
P'_6							1.00	0.10
P'_8								1.00

Table 77. Correlation matrix for the optimised angular observables obtained for the method of moments in the bin $7.0 < q^2 < 8.0\,\text{GeV}^2/c^4$.

	F_L	P_1	P_2	P_3	P'_4	P'_5	P'_6	P'_8
F_L	1.00	−0.32	0.60	0.17	0.15	0.02	−0.06	−0.13
P_1		1.00	−0.24	−0.05	−0.12	−0.19	0.06	0.06
P_2			1.00	0.16	−0.03	−0.09	−0.03	−0.14
P_3				1.00	0.05	0.09	0.01	0.07
P'_4					1.00	0.19	−0.11	−0.14
P'_5						1.00	−0.12	−0.10
P'_6							1.00	0.24
P'_8								1.00

Table 78. Correlation matrix for the optimised angular observables obtained for the method of moments in the bin $11.00 < q^2 < 11.75\,\text{GeV}^2/c^4$.

	F_L	P_1	P_2	P_3	P'_4	P'_5	P'_6	P'_8
F_L	1.00	−0.41	0.55	−0.10	−0.46	−0.47	−0.37	−0.10
P_1		1.00	−0.48	0.05	0.15	0.16	0.20	0.04
P_2			1.00	−0.19	−0.55	−0.57	−0.40	−0.13
P_3				1.00	0.11	0.18	0.20	0.09
P'_4					1.00	0.52	0.40	0.23
P'_5						1.00	0.45	0.16
P'_6							1.00	0.22
P'_8								1.00

Table 79. Correlation matrix for the optimised angular observables obtained for the method of moments in the bin $11.75 < q^2 < 12.50\,\text{GeV}^2/c^4$.

	F_L	P_1	P_2	P_3	P'_4	P'_5	P'_6	P'_8
F_L	1.00	−0.03	0.41	0.09	0.12	0.06	0.00	0.05
P_1		1.00	0.07	0.09	−0.15	−0.28	−0.03	0.01
P_2			1.00	0.08	−0.02	−0.11	−0.01	−0.01
P_3				1.00	0.02	0.06	0.10	0.12
P'_4					1.00	0.34	−0.02	−0.16
P'_5						1.00	−0.13	−0.02
P'_6							1.00	0.12
P'_8								1.00

Table 80. Correlation matrix for the optimised angular observables obtained for the method of moments in the bin $15.0 < q^2 < 16.0\,\text{GeV}^2/c^4$.

	F_{L}	P_1	P_2	P_3	P_4'	P_5'	P_6'	P_8'
F_{L}	1.00	−0.09	0.33	0.03	0.17	0.23	0.06	−0.01
P_1		1.00	0.07	0.03	−0.12	−0.14	0.01	−0.02
P_2			1.00	0.04	−0.15	−0.06	0.02	0.02
P_3				1.00	−0.06	−0.18	0.13	0.08
P_4'					1.00	0.25	0.09	−0.02
P_5'						1.00	0.02	0.06
P_6'							1.00	0.14
P_8'								1.00

Table 81. Correlation matrix for the optimised angular observables obtained for the method of moments in the bin $16.0 < q^2 < 17.0 \, \mathrm{GeV}^2/c^4$.

	F_{L}	P_1	P_2	P_3	P_4'	P_5'	P_6'	P_8'
F_{L}	1.00	−0.07	0.28	0.11	0.04	0.21	−0.06	0.06
P_1		1.00	0.02	0.07	−0.12	−0.20	0.10	0.00
P_2			1.00	0.00	−0.07	0.01	−0.01	0.06
P_3				1.00	0.00	−0.03	0.19	0.05
P_4'					1.00	0.15	0.04	−0.12
P_5'						1.00	−0.17	0.08
P_6'							1.00	0.11
P_8'								1.00

Table 82. Correlation matrix for the optimised angular observables obtained for the method of moments in the bin $17.0 < q^2 < 18.0 \, \mathrm{GeV}^2/c^4$.

	F_{L}	P_1	P_2	P_3	P_4'	P_5'	P_6'	P_8'
F_{L}	1.00	0.03	0.39	0.10	−0.06	−0.01	0.00	0.06
P_1		1.00	0.02	0.03	−0.14	−0.18	0.00	0.03
P_2			1.00	0.00	−0.27	−0.29	−0.03	0.07
P_3				1.00	−0.01	−0.03	0.17	0.02
P_4'					1.00	0.38	0.03	0.01
P_5'						1.00	−0.01	−0.03
P_6'							1.00	0.19
P_8'								1.00

Table 83. Correlation matrix for the optimised angular observables obtained for the method of moments in the bin $18.0 < q^2 < 19.0 \, \mathrm{GeV}^2/c^4$.

	F_{L}	P_1	P_2	P_3	P_4'	P_5'	P_6'	P_8'
F_{L}	1.00	−0.05	0.33	0.08	0.08	0.13	0.01	0.03
P_1		1.00	0.05	0.05	−0.14	−0.21	0.02	0.01
P_2			1.00	0.03	−0.10	−0.07	−0.01	0.02
P_3				1.00	−0.02	−0.06	0.15	0.07
P_4'					1.00	0.24	0.04	−0.07
P_5'						1.00	−0.07	0.03
P_6'							1.00	0.14
P_8'								1.00

Table 84. Correlation matrix for the optimised angular observables obtained for the method of moments in the bin $15.0 < q^2 < 19.0 \, \mathrm{GeV}^2/c^4$.

References

[1] LHCb collaboration, *Differential branching fraction and angular analysis of the decay $B^0 \to K^{*0}\mu^+\mu^-$*, *JHEP* **08** (2013) 131 [arXiv:1304.6325] [inSPIRE].

[2] BaBar collaboration, B. Aubert et al., *Measurements of branching fractions, rate asymmetries and angular distributions in the rare decays $B \to K\ell^+\ell^-$ and $B \to K^*\ell^+\ell^-$*, *Phys. Rev.* **D 73** (2006) 092001 [hep-ex/0604007] [inSPIRE].

[3] BaBar collaboration, J.P. Lees et al., *Measurement of angular asymmetries in the decays $B \to K^*\ell^+\ell^-$*, arXiv:1508.07960 [inSPIRE].

[4] Belle collaboration, J.T. Wei et al., *Measurement of the differential branching fraction and forward-backword asymmetry for $B \to K^{(*)}\ell^+\ell^-$*, *Phys. Rev. Lett.* **103** (2009) 171801 [arXiv:0904.0770] [inSPIRE].

[5] CDF collaboration, T. Aaltonen et al., *Measurements of the angular distributions in the decays $B \to K^{(*)}\mu^+\mu^-$ at CDF*, *Phys. Rev. Lett.* **108** (2012) 081807 [arXiv:1108.0695] [inSPIRE].

[6] CMS collaboration, *Angular analysis and branching fraction measurement of the decay $B^0 \to K^{*0}\mu^+\mu^-$*, *Phys. Lett.* **B 727** (2013) 77 [arXiv:1308.3409] [inSPIRE].

[7] CMS collaboration, *Angular analysis of the decay $B^0 \to K^{*0}\mu^+\mu^-$ from pp collisions at $\sqrt{s} = 8\,TeV$*, *Phys. Lett.* **B 753** (2016) 424 [arXiv:1507.08126] [inSPIRE].

[8] LHCb collaboration, *Measurement of form-factor-independent observables in the decay $B^0 \to K^{*0}\mu^+\mu^-$*, *Phys. Rev. Lett.* **111** (2013) 191801 [arXiv:1308.1707] [inSPIRE].

[9] S. Descotes-Genon, J. Matias and J. Virto, *Understanding the $B \to K^*\mu^+\mu^-$ anomaly*, *Phys. Rev.* **D 88** (2013) 074002 [arXiv:1307.5683] [inSPIRE].

[10] W. Altmannshofer and D.M. Straub, *New physics in $B \to K^*\mu\mu$?*, *Eur. Phys. J.* **C 73** (2013) 2646 [arXiv:1308.1501] [inSPIRE].

[11] F. Beaujean, C. Bobeth and D. van Dyk, *Comprehensive bayesian analysis of rare (semi)leptonic and radiative B decays*, *Eur. Phys. J.* **C 74** (2014) 2897 [*Erratum ibid.* **C 74** (2014) 3179] [arXiv:1310.2478] [inSPIRE].

[12] T. Hurth and F. Mahmoudi, *On the LHCb anomaly in $B \to K^*\ell^+\ell^-$*, *JHEP* **04** (2014) 097 [arXiv:1312.5267] [inSPIRE].

[13] S. Jäger and J. Martin Camalich, *On $B \to V\ell\ell$ at small dilepton invariant mass, power corrections and new physics*, *JHEP* **05** (2013) 043 [arXiv:1212.2263] [inSPIRE].

[14] S. Descotes-Genon, L. Hofer, J. Matias and J. Virto, *On the impact of power corrections in the prediction of $B \to K^*\mu^+\mu^-$ observables*, *JHEP* **12** (2014) 125 [arXiv:1407.8526] [inSPIRE].

[15] J. Lyon and R. Zwicky, *Resonances gone topsy turvy — The charm of QCD or new physics in $b \to s\ell^+\ell^-$?*, arXiv:1406.0566 [inSPIRE].

[16] W. Altmannshofer, S. Gori, M. Pospelov and I. Yavin, *Quark flavor transitions in $L_\mu - L_\tau$ models*, *Phys. Rev.* **D 89** (2014) 095033 [arXiv:1403.1269] [inSPIRE].

[17] A. Crivellin, G. D'Ambrosio and J. Heeck, *Explaining $h \to \mu^{\pm}\tau^{\mp}$, $B \to K^*\mu^+\mu^-$ and $B \to K\mu^+\mu^-/B \to Ke^+e^-$ in a two-Higgs-doublet model with gauged $L_\mu - L_\tau$*, *Phys. Rev. Lett.* **114** (2015) 151801 [arXiv:1501.00993] [INSPIRE].

[18] R. Gauld, F. Goertz and U. Haisch, *An explicit Z'-boson explanation of the $B \to K^*\mu^+\mu^-$ anomaly*, *JHEP* **01** (2014) 069 [arXiv:1310.1082] [INSPIRE].

[19] W. Altmannshofer and D.M. Straub, *New physics in $b \to s$ transitions after LHC run 1*, *Eur. Phys. J.* **C 75** (2015) 382 [arXiv:1411.3161] [INSPIRE].

[20] F. Mahmoudi, S. Neshatpour and J. Virto, *$B \to K^*\mu^+\mu^-$ optimised observables in the MSSM*, *Eur. Phys. J.* **C 74** (2014) 2927 [arXiv:1401.2145] [INSPIRE].

[21] A. Datta, M. Duraisamy and D. Ghosh, *Explaining the $B \to K^*\mu^+\mu^-$ data with scalar interactions*, *Phys. Rev.* **D 89** (2014) 071501 [arXiv:1310.1937] [INSPIRE].

[22] W. Altmannshofer, P. Ball, A. Bharucha, A.J. Buras, D.M. Straub and M. Wick, *Symmetries and asymmetries of $B \to K^*\mu^+\mu^-$ decays in the Standard Model and beyond*, *JHEP* **01** (2009) 019 [arXiv:0811.1214] [INSPIRE].

[23] F. Krüger and J. Matias, *Probing new physics via the transverse amplitudes of $B^0 \to K^{*0}(\to K^-\pi^+)\ell^+\ell^-$ at large recoil*, *Phys. Rev.* **D 71** (2005) 094009 [hep-ph/0502060] [INSPIRE].

[24] S. Descotes-Genon, J. Matias, M. Ramon and J. Virto, *Implications from clean observables for the binned analysis of $B \to K^*\mu^+\mu^-$ at large recoil*, *JHEP* **01** (2013) 048 [arXiv:1207.2753] [INSPIRE].

[25] F. Beaujean, M. Chrzaszcz, N. Serra and D. van Dyk, *Extracting angular observables without a likelihood and applications to rare decays*, *Phys. Rev.* **D 91** (2015) 114012 [arXiv:1503.04100] [INSPIRE].

[26] A. Ali, P. Ball, L.T. Handoko and G. Hiller, *A comparative study of the decays $B \to (K, K^*)\ell^+\ell^-$ in standard model and supersymmetric theories*, *Phys. Rev.* **D 61** (2000) 074024 [hep-ph/9910221] [INSPIRE].

[27] G. Kumar and N. Mahajan, *$B \to K^*l^+l^-$: zeroes of angular observables as test of standard model*, arXiv:1412.2955 [INSPIRE].

[28] LHCb collaboration, *The LHCb detector at the LHC*, 2008 *JINST* **3** S08005 [INSPIRE].

[29] LHCb collaboration, *LHCb detector performance*, *Int. J. Mod. Phys.* **A 30** (2015) 1530022 [arXiv:1412.6352] [INSPIRE].

[30] R. Aaij et al., *The LHCb trigger and its performance in 2011*, 2013 *JINST* **8** P04022 [arXiv:1211.3055] [INSPIRE].

[31] T. Sjöstrand, S. Mrenna and P.Z. Skands, *PYTHIA 6.4 physics and manual*, *JHEP* **05** (2006) 026 [hep-ph/0603175] [INSPIRE].

[32] T. Sjöstrand, S. Mrenna and P.Z. Skands, *A brief introduction to PYTHIA 8.1*, *Comput. Phys. Commun.* **178** (2008) 852 [arXiv:0710.3820] [INSPIRE].

[33] I. Belyaev et al., *Handling of the generation of primary events in Gauss, the LHCb simulation framework*, *J. Phys. Conf. Ser.* **331** (2011) 032047 [INSPIRE].

[34] D.J. Lange, *The EvtGen particle decay simulation package*, *Nucl. Instrum. Meth.* **A 462** (2001) 152 [INSPIRE].

[35] P. Golonka and Z. Was, *PHOTOS Monte Carlo: a precision tool for QED corrections in Z and W decays*, *Eur. Phys. J.* **C 45** (2006) 97 [hep-ph/0506026] [INSPIRE].

[36] Geant4 collaboration, J. Allison et al., *GEANT4 developments and applications*, *IEEE Trans. Nucl. Sci.* **53** (2006) 270.

[37] GEANT4 collaboration, S. Agostinelli et al., *GEANT4: a simulation toolkit*, *Nucl. Instrum. Meth.* **A 506** (2003) 250 [INSPIRE].

[38] M. Clemencic et al., *The LHCb simulation application, Gauss: design, evolution and experience*, *J. Phys. Conf. Ser.* **331** (2011) 032023 [INSPIRE].

[39] L. Breiman, J.H. Friedman, R.A. Olshen and C.J. Stone, *Classification and regression trees*, Wadsworth international group, Belmont, California U.S.A. (1984).

[40] R.E. Schapire and Y. Freund, *A decision-theoretic generalization of on-line learning and an application to boosting*, *J.. Comp. Syst. Sc.* **55** (1997) 119.

[41] LHCb collaboration, *Search for the rare decays $B_s^0 \to \mu^+\mu^-$ and $B^0 \to \mu^+\mu^-$*, *Phys. Lett.* **B 699** (2011) 330 [arXiv:1103.2465] [INSPIRE].

[42] A. Blum, A. Kalai and J. Langford, *Beating the hold-out: bounds for k-fold and progressive cross-validation*, in the proceedings of the *Twelfth annual conference on Computational Learning Theory (COLT '99)*, July 6–9, Santa Cruz, U.S.A. (1999).

[43] BaBar collaboration, B. Aubert et al., *Measurement of decay amplitudes of $B \to J/\psi K^*, \psi(2S)K^*$ and $\chi_{c1}K^*$ with an angular analysis*, *Phys. Rev.* **D 76** (2007) 031102 [arXiv:0704.0522] [INSPIRE].

[44] Belle collaboration, K. Chilikin et al., *Observation of a new charged charmoniumlike state in $\bar{B}^0 \to J/\psi K^- \pi^+$ decays*, *Phys. Rev.* **D 90** (2014) 112009 [arXiv:1408.6457] [INSPIRE].

[45] LHCb collaboration, *Measurement of the polarization amplitudes in $B^0 \to J/\psi K^*(892)^0$ decays*, *Phys. Rev.* **D 88** (2013) 052002 [arXiv:1307.2782] [INSPIRE].

[46] LHCb collaboration, *Measurement of the $B_s^0 \to J/\psi \bar{K}^{*0}$ branching fraction and angular amplitudes*, *Phys. Rev.* **D 86** (2012) 071102 [arXiv:1208.0738] [INSPIRE].

[47] D. Aston et al., *A study of $K^-\pi^+$ scattering in the reaction $K^-p \to K^-\pi^+ n$ at 11 GeV/c*, *Nucl. Phys.* **B 296** (1988) 493.

[48] G.J. Feldman and R.D. Cousins, *A Unified approach to the classical statistical analysis of small signals*, *Phys. Rev.* **D 57** (1998) 3873 [physics/9711021] [INSPIRE].

[49] B. Sen, M. Walker and M. Woodroofe, *On the unified method with nuisance parameters*, *Stat. Sinica* **19** (2009) 301.

[50] J. Gratrex, M. Hopfer and R. Zwicky, *Generalised helicity formalism, higher moments and the $B \to K_{J_K}(\to K\pi)\bar{\ell}_1\ell_2$ angular distributions*, arXiv:1506.03970 [INSPIRE].

[51] B. Efron, *Bootstrap methods: another look at the jackknife*, *Ann. Statist.* **7** (1979) 1.

[52] F. Beaujean, C. Bobeth and S. Jahn, *Constraints on tensor and scalar couplings from $B \to K\bar{\mu}\mu$ and $B_s \to \bar{\mu}\mu$*, *Eur. Phys. J.* **C 75** (2015) 456 [arXiv:1508.01526] [INSPIRE].

[53] U. Egede, T. Hurth, J. Matias, M. Ramon and W. Reece, *New physics reach of the decay mode $\bar{B} \to \bar{K}^{*0}\ell^+\ell^-$*, *JHEP* **10** (2010) 056 [arXiv:1005.0571] [INSPIRE].

[54] U. Egede, M. Patel and K.A. Petridis, *Method for an unbinned measurement of the q^2 dependent decay amplitudes of $\overline{B}^0 \to K^{*0}\mu^+\mu^-$ decays*, *JHEP* **06** (2015) 084 [arXiv:1504.00574] [INSPIRE].

[55] C.-D. Lu and W. Wang, *Analysis of $B \to K_J^*(\to K\pi)\mu^+\mu^-$ in the higher kaon resonance region*, *Phys. Rev.* **D 85** (2012) 034014 [arXiv:1111.1513] [INSPIRE].

[56] LHCb collaboration, *Measurement of the $\bar{B}^0 - B^0$ and $\bar{B}_s^0 - B_s^0$ production asymmetries in pp collisions at $\sqrt{s} = 7$ TeV*, *Phys. Lett.* **B 739** (2014) 218 [arXiv:1408.0275] [INSPIRE].

[57] LHCb collaboration, *Measurement of the semileptonic CP asymmetry in $B^0 - \overline{B}^0$ mixing*, *Phys. Rev. Lett.* **114** (2015) 041601 [arXiv:1409.8586] [INSPIRE].

[58] LHCb collaboration, *Measurement of CP asymmetry in $D^0 \to K^- K^+$ and $D^0 \to \pi^- \pi^+$ decays*, *JHEP* **07** (2014) 041 [arXiv:1405.2797] [INSPIRE].

[59] C. Bobeth, G. Hiller and D. van Dyk, *The benefits of $\bar{B} \to \bar{K}^* l^+ l^-$ decays at low recoil*, *JHEP* **07** (2010) 098 [arXiv:1006.5013] [INSPIRE].

[60] S. Jäger and J. Martin Camalich, *Reassessing the discovery potential of the $B \to K^* \ell^+ \ell^-$ decays in the large-recoil region: SM challenges and BSM opportunities*, *Phys. Rev.* **D 93** (2016) 014028 [arXiv:1412.3183] [INSPIRE].

[61] D. Das and R. Sinha, *New physics effects and hadronic form factor uncertainties in $B \to K^* \ell^+ \ell^-$*, *Phys. Rev.* **D 86** (2012) 056006 [arXiv:1205.1438] [INSPIRE].

[62] R.R. Horgan, Z. Liu, S. Meinel and M. Wingate, *Calculation of $B^0 \to K^{*0} \mu^+ \mu^-$ and $B_s^0 \to \phi \mu^+ \mu^-$ observables using form factors from lattice QCD*, *Phys. Rev. Lett.* **112** (2014) 212003 [arXiv:1310.3887] [INSPIRE].

[63] C. Hambrock, G. Hiller, S. Schacht and R. Zwicky, *$B \to K^\star$ form factors from flavor data to QCD and back*, *Phys. Rev.* **D 89** (2014) 074014 [arXiv:1308.4379] [INSPIRE].

[64] T. Hurth, F. Mahmoudi and S. Neshatpour, *Global fits to $b \to s\ell\ell$ data and signs for lepton non-universality*, *JHEP* **12** (2014) 053 [arXiv:1410.4545] [INSPIRE].

[65] P. Ball and R. Zwicky, *$B_{d,s} \to \rho, \omega, K^*, \phi$ decay form-factors from light-cone sum rules revisited*, *Phys. Rev.* **D 71** (2005) 014029 [hep-ph/0412079] [INSPIRE].

[66] A. Bharucha, D.M. Straub and R. Zwicky, *$B \to V \ell^+ \ell^-$ in the standard model from light-cone sum rules*, arXiv:1503.05534 [INSPIRE].

[67] R.R. Horgan, Z. Liu, S. Meinel and M. Wingate, *Lattice QCD calculation of form factors describing the rare decays $B \to K^* \ell^+ \ell^-$ and $B_s \to \phi \ell^+ \ell^-$*, *Phys. Rev.* **D 89** (2014) 094501 [arXiv:1310.3722] [INSPIRE].

[68] R.R. Horgan, Z. Liu, S. Meinel and M. Wingate, *Rare B decays using lattice QCD form factors*, PoS(LATTICE2014)372 [arXiv:1501.00367] [INSPIRE].

[69] A. Khodjamirian, T. Mannel, A.A. Pivovarov and Y.M. Wang, *Charm-loop effect in $B \to K^{(*)} \ell^+ \ell^-$ and $B \to K^* \gamma$*, *JHEP* **09** (2010) 089 [arXiv:1006.4945] [INSPIRE].

[70] S. Descotes-Genon, T. Hurth, J. Matias and J. Virto, *Optimizing the basis of $B \to K^* \ell\ell$ observables in the full kinematic range*, *JHEP* **05** (2013) 137 [arXiv:1303.5794] [INSPIRE].

[71] C. Bobeth, G. Hiller, D. van Dyk and C. Wacker, *The Decay $B \to K \ell^+ \ell^-$ at Low Hadronic Recoil and Model-Independent $\Delta B = 1$ Constraints*, *JHEP* **01** (2012) 107 [arXiv:1111.2558] [INSPIRE].

[72] M. Beneke, T. Feldmann and D. Seidel, *Exclusive radiative and electroweak $b \to d$ and $b \to s$ penguin decays at NLO*, *Eur. Phys. J.* **C 41** (2005) 173 [hep-ph/0412400] [INSPIRE].

[73] A. Ali, G. Kramer and G.-h. Zhu, *$B \to K^+ \ell^+ \ell^-$ decay in soft-collinear effective theory*, *Eur. Phys. J.* **C 47** (2006) 625 [hep-ph/0601034] [INSPIRE].

[74] LHCb, CMS collaboration, *Observation of the rare $B_s^0 \to \mu^+ \mu^-$ decay from the combined analysis of CMS and LHCb data*, *Nature* **522** (2015) 68 [arXiv:1411.4413] [INSPIRE].

The LHCb collaboration

R. Aaij[39], C. Abellán Beteta[41], B. Adeva[38], M. Adinolfi[47], A. Affolder[53], Z. Ajaltouni[5], S. Akar[6], J. Albrecht[10], F. Alessio[39], M. Alexander[52], S. Ali[42], G. Alkhazov[31], P. Alvarez Cartelle[54], A.A. Alves Jr.[58], S. Amato[2], S. Amerio[23], Y. Amhis[7], L. An[3,40], L. Anderlini[18], G. Andreassi[40], M. Andreotti[17,g], J.E. Andrews[59], R.B. Appleby[55], O. Aquines Gutierrez[11], F. Archilli[39], P. d'Argent[12], A. Artamonov[36], M. Artuso[60], E. Aslanides[6], G. Auriemma[26,n], M. Baalouch[5], S. Bachmann[12], J.J. Back[49], A. Badalov[37], C. Baesso[61], W. Baldini[17,39], R.J. Barlow[55], C. Barschel[39], S. Barsuk[7], W. Barter[39], V. Batozskaya[29], V. Battista[40], A. Bay[40], L. Beaucourt[4], J. Beddow[52], F. Bedeschi[24], I. Bediaga[1], L.J. Bel[42], V. Bellee[40], N. Belloli[21,k], I. Belyaev[32], E. Ben-Haim[8], G. Bencivenni[19], S. Benson[39], J. Benton[47], A. Berezhnoy[33], R. Bernet[41], A. Bertolin[23], M.-O. Bettler[39], M. van Beuzekom[42], S. Bifani[46], P. Billoir[8], T. Bird[55], A. Birnkraut[10], A. Bizzeti[18,i], T. Blake[49], F. Blanc[40], J. Blouw[11], S. Blusk[60], V. Bocci[26], A. Bondar[35], N. Bondar[31,39], W. Bonivento[16], S. Borghi[55], M. Borisyak[66], M. Borsato[38], T.J.V. Bowcock[53], E. Bowen[41], C. Bozzi[17,39], S. Braun[12], M. Britsch[12], T. Britton[60], J. Brodzicka[55], N.H. Brook[47], E. Buchanan[47], C. Burr[55], A. Bursche[41], J. Buytaert[39], S. Cadeddu[16], R. Calabrese[17,g], M. Calvi[21,k], M. Calvo Gomez[37,p], P. Campana[19], D. Campora Perez[39], L. Capriotti[55], A. Carbone[15,e], G. Carboni[25,l], R. Cardinale[20,j], A. Cardini[16], P. Carniti[21,k], L. Carson[51], K. Carvalho Akiba[2], G. Casse[53], L. Cassina[21,k], L. Castillo Garcia[40], M. Cattaneo[39], Ch. Cauet[10], G. Cavallero[20], R. Cenci[24,t], M. Charles[8], Ph. Charpentier[39], M. Chefdeville[4], S. Chen[55], S.-F. Cheung[56], N. Chiapolini[41], M. Chrzaszcz[41,27], X. Cid Vidal[39], G. Ciezarek[42], P.E.L. Clarke[51], M. Clemencic[39], H.V. Cliff[48], J. Closier[39], V. Coco[39], J. Cogan[6], E. Cogneras[5], V. Cogoni[16,f], L. Cojocariu[30], G. Collazuol[23,r], P. Collins[39], A. Comerma-Montells[12], A. Contu[39], A. Cook[47], M. Coombes[47], S. Coquereau[8], G. Corti[39], M. Corvo[17,g], B. Couturier[39], G.A. Cowan[51], D.C. Craik[51], A. Crocombe[49], M. Cruz Torres[61], S. Cunliffe[54], R. Currie[54], C. D'Ambrosio[39], E. Dall'Occo[42], J. Dalseno[47], P.N.Y. David[42], A. Davis[58], O. De Aguiar Francisco[2], K. De Bruyn[6], S. De Capua[55], M. De Cian[12], J.M. De Miranda[1], L. De Paula[2], P. De Simone[19], C.-T. Dean[52], D. Decamp[4], M. Deckenhoff[10], L. Del Buono[8], N. Déléage[4], M. Demmer[10], D. Derkach[66], O. Deschamps[5], F. Dettori[39], B. Dey[22], A. Di Canto[39], F. Di Ruscio[25], H. Dijkstra[39], S. Donleavy[53], F. Dordei[39], M. Dorigo[40], A. Dosil Suárez[38], A. Dovbnya[44], K. Dreimanis[53], L. Dufour[42], G. Dujany[55], K. Dungs[39], P. Durante[39], R. Dzhelyadin[36], A. Dziurda[27], A. Dzyuba[31], S. Easo[50,39], U. Egede[54], V. Egorychev[32], S. Eidelman[35], S. Eisenhardt[51], U. Eitschberger[10], R. Ekelhof[10], L. Eklund[52], I. El Rifai[5], Ch. Elsasser[41], S. Ely[60], S. Esen[12], H.M. Evans[48], T. Evans[56], M. Fabianska[27], A. Falabella[15], C. Färber[39], N. Farley[46], S. Farry[53], R. Fay[53], D. Ferguson[51], V. Fernandez Albor[38], F. Ferrari[15], F. Ferreira Rodrigues[1], M. Ferro-Luzzi[39], S. Filippov[34], M. Fiore[17,39,g], M. Fiorini[17,g], M. Firlej[28], C. Fitzpatrick[40], T. Fiutowski[28], F. Fleuret[7,b], K. Fohl[39], P. Fol[54], M. Fontana[16], F. Fontanelli[20,j], D. C. Forshaw[60], R. Forty[39], M. Frank[39], C. Frei[39], M. Frosini[18], J. Fu[22], E. Furfaro[25,l], A. Gallas Torreira[38], D. Galli[15,e], S. Gallorini[23], S. Gambetta[51], M. Gandelman[2], P. Gandini[56], Y. Gao[3], J. García Pardiñas[38], J. Garra Tico[48], L. Garrido[37], D. Gascon[37], C. Gaspar[39], R. Gauld[56], L. Gavardi[10], G. Gazzoni[5], D. Gerick[12], E. Gersabeck[12], M. Gersabeck[55], T. Gershon[49], Ph. Ghez[4], S. Gianì[40], V. Gibson[48], O.G. Girard[40], L. Giubega[30], V.V. Gligorov[39], C. Göbel[61], D. Golubkov[32], A. Golutvin[54,39], A. Gomes[1,a], C. Gotti[21,k], M. Grabalosa Gándara[5], R. Graciani Diaz[37], L.A. Granado Cardoso[39], E. Graugés[37], E. Graverini[41], G. Graziani[18], A. Grecu[30], E. Greening[56], P. Griffith[46], L. Grillo[12], O. Grünberg[64], B. Gui[60], E. Gushchin[34], Yu. Guz[36,39], T. Gys[39], T. Hadavizadeh[56], C. Hadjivasiliou[60], G. Haefeli[40], C. Haen[39], S.C. Haines[48], S. Hall[54], B. Hamilton[59], X. Han[12], S. Hansmann-Menzemer[12], N. Harnew[56], S.T. Harnew[47], J. Harrison[55], J. He[39], T. Head[40],

V. Heijne[42], A. Heister[9], K. Hennessy[53], P. Henrard[5], L. Henry[8], J.A. Hernando Morata[38],
E. van Herwijnen[39], M. Heß[64], A. Hicheur[2], D. Hill[56], M. Hoballah[5], C. Hombach[55],
W. Hulsbergen[42], T. Humair[54], M. Hushchyn[66], N. Hussain[56], D. Hutchcroft[53], D. Hynds[52],
M. Idzik[28], P. Ilten[57], R. Jacobsson[39], A. Jaeger[12], J. Jalocha[56], E. Jans[42], A. Jawahery[59],
M. John[56], D. Johnson[39], C.R. Jones[48], C. Joram[39], B. Jost[39], N. Jurik[60], S. Kandybei[44],
W. Kanso[6], M. Karacson[39], T.M. Karbach[39,†], S. Karodia[52], M. Kecke[12], M. Kelsey[60],
I.R. Kenyon[46], M. Kenzie[39], T. Ketel[43], E. Khairullin[66], B. Khanji[21,39,k], C. Khurewathanakul[40],
T. Kirn[9], S. Klaver[55], K. Klimaszewski[29], O. Kochebina[7], M. Kolpin[12], I. Komarov[40],
R.F. Koopman[43], P. Koppenburg[42,39], M. Kozeiha[5], L. Kravchuk[34], K. Kreplin[12], M. Kreps[49],
P. Krokovny[35], F. Kruse[10], W. Krzemien[29], W. Kucewicz[27,o], M. Kucharczyk[27],
V. Kudryavtsev[35], A. K. Kuonen[40], K. Kurek[29], T. Kvaratskheliya[32], D. Lacarrere[39],
G. Lafferty[55,39], A. Lai[16], D. Lambert[51], G. Lanfranchi[19], C. Langenbruch[49], B. Langhans[39],
T. Latham[49], C. Lazzeroni[46], R. Le Gac[6], J. van Leerdam[42], J.-P. Lees[4], R. Lefèvre[5],
A. Leflat[33,39], J. Lefrançois[7], E. Lemos Cid[38], O. Leroy[6], T. Lesiak[27], B. Leverington[12], Y. Li[7],
T. Likhomanenko[66,65], M. Liles[53], R. Lindner[39], C. Linn[39], F. Lionetto[41], B. Liu[16], X. Liu[3],
D. Loh[49], I. Longstaff[52], J.H. Lopes[2], D. Lucchesi[23,r], M. Lucio Martinez[38], H. Luo[51],
A. Lupato[23], E. Luppi[17,g], O. Lupton[56], A. Lusiani[24], F. Machefert[7], F. Maciuc[30], O. Maev[31],
K. Maguire[55], S. Malde[56], A. Malinin[65], G. Manca[7], G. Mancinelli[6], P. Manning[60], A. Mapelli[39],
J. Maratas[5], J.F. Marchand[4], U. Marconi[15], C. Marin Benito[37], P. Marino[24,39,t], J. Marks[12],
G. Martellotti[26], M. Martin[6], M. Martinelli[40], D. Martinez Santos[38], F. Martinez Vidal[67],
D. Martins Tostes[2], L.M. Massacrier[7], A. Massafferri[1], R. Matev[39], A. Mathad[49], Z. Mathe[39],
C. Matteuzzi[21], A. Mauri[41], B. Maurin[40], A. Mazurov[46], M. McCann[54], J. McCarthy[46],
A. McNab[55], R. McNulty[13], B. Meadows[58], F. Meier[10], M. Meissner[12], D. Melnychuk[29],
M. Merk[42], E Michielin[23], D.A. Milanes[63], M.-N. Minard[4], D.S. Mitzel[12], J. Molina Rodriguez[61],
I.A. Monroy[63], S. Monteil[5], M. Morandin[23], P. Morawski[28], A. Mordà[6], M.J. Morello[24,t],
J. Moron[28], A.B. Morris[51], R. Mountain[60], F. Muheim[51], D. Müller[55], J. Müller[10], K. Müller[41],
V. Müller[10], M. Mussini[15], B. Muster[40], P. Naik[47], T. Nakada[40], R. Nandakumar[50], A. Nandi[56],
I. Nasteva[2], M. Needham[51], N. Neri[22], S. Neubert[12], N. Neufeld[39], M. Neuner[12], A.D. Nguyen[40],
T.D. Nguyen[40], C. Nguyen-Mau[40,q], V. Niess[5], R. Niet[10], N. Nikitin[33], T. Nikodem[12],
A. Novoselov[36], D.P. O'Hanlon[49], A. Oblakowska-Mucha[28], V. Obraztsov[36], S. Ogilvy[52],
O. Okhrimenko[45], R. Oldeman[16,f], C.J.G. Onderwater[68], B. Osorio Rodrigues[1],
J.M. Otalora Goicochea[2], A. Otto[39], P. Owen[54], A. Oyanguren[67], A. Palano[14,d], F. Palombo[22,u],
M. Palutan[19], J. Panman[39], A. Papanestis[50], M. Pappagallo[52], L.L. Pappalardo[17,g],
C. Pappenheimer[58], W. Parker[59], C. Parkes[55], G. Passaleva[18], G.D. Patel[53], M. Patel[54],
C. Patrignani[20,j], A. Pearce[55,50], A. Pellegrino[42], G. Penso[26,m], M. Pepe Altarelli[39],
S. Perazzini[15,e], P. Perret[5], L. Pescatore[46], K. Petridis[47], A. Petrolini[20,j], M. Petruzzo[22],
E. Picatoste Olloqui[37], B. Pietrzyk[4], M. Pikies[27], D. Pinci[26], A. Pistone[20], A. Piucci[12],
S. Playfer[51], M. Plo Casasus[38], T. Poikela[39], F. Polci[8], A. Poluektov[49,35], I. Polyakov[32],
E. Polycarpo[2], A. Popov[36], D. Popov[11,39], B. Popovici[30], C. Potterat[2], E. Price[47], J.D. Price[53],
J. Prisciandaro[38], A. Pritchard[53], C. Prouve[47], V. Pugatch[45], A. Puig Navarro[40], G. Punzi[24,s],
W. Qian[4], R. Quagliani[7,47], B. Rachwal[27], J.H. Rademacker[47], M. Rama[24], M. Ramos Pernas[38],
M.S. Rangel[2], I. Raniuk[44], N. Rauschmayr[39], G. Raven[43], F. Redi[54], S. Reichert[55],
A.C. dos Reis[1], V. Renaudin[7], S. Ricciardi[50], S. Richards[47], M. Rihl[39], K. Rinnert[53,39],
V. Rives Molina[37], P. Robbe[7,39], A.B. Rodrigues[1], E. Rodrigues[55], J.A. Rodriguez Lopez[63],
P. Rodriguez Perez[55], S. Roiser[39], V. Romanovsky[36], A. Romero Vidal[38], J. W. Ronayne[13],
M. Rotondo[23], T. Ruf[39], P. Ruiz Valls[67], J.J. Saborido Silva[38], N. Sagidova[31], B. Saitta[16,f],
V. Salustino Guimaraes[2], C. Sanchez Mayordomo[67], B. Sanmartin Sedes[38], R. Santacesaria[26],
C. Santamarina Rios[38], M. Santimaria[19], E. Santovetti[25,l], A. Sarti[19,m], C. Satriano[26,n],

A. Satta[25], D.M. Saunders[47], D. Savrina[32,33], S. Schael[9], M. Schiller[39], H. Schindler[39],
M. Schlupp[10], M. Schmelling[11], T. Schmelzer[10], B. Schmidt[39], O. Schneider[40], A. Schopper[39],
M. Schubiger[40], M.-H. Schune[7], R. Schwemmer[39], B. Sciascia[19], A. Sciubba[26,m], A. Semennikov[32],
A. Sergi[46], N. Serra[41], J. Serrano[6], L. Sestini[23], P. Seyfert[21], M. Shapkin[36], I. Shapoval[17,44,g],
Y. Shcheglov[31], T. Shears[53], L. Shekhtman[35], V. Shevchenko[65], A. Shires[10], B.G. Siddi[17],
R. Silva Coutinho[41], L. Silva de Oliveira[2], G. Simi[23,s], M. Sirendi[48], N. Skidmore[47],
T. Skwarnicki[60], E. Smith[56,50], E. Smith[54], I.T. Smith[51], J. Smith[48], M. Smith[55], H. Snoek[42],
M.D. Sokoloff[58,39], F.J.P. Soler[52], F. Soomro[40], D. Souza[47], B. Souza De Paula[2], B. Spaan[10],
P. Spradlin[52], S. Sridharan[39], F. Stagni[39], M. Stahl[12], S. Stahl[39], S. Stefkova[54], O. Steinkamp[41],
O. Stenyakin[36], S. Stevenson[56], S. Stoica[30], S. Stone[60], B. Storaci[41], S. Stracka[24,t],
M. Straticiuc[30], U. Straumann[41], L. Sun[58], W. Sutcliffe[54], K. Swientek[28], S. Swientek[10],
V. Syropoulos[43], M. Szczekowski[29], T. Szumlak[28], S. T'Jampens[4], A. Tayduganov[6],
T. Tekampe[10], G. Tellarini[17,g], F. Teubert[39], C. Thomas[56], E. Thomas[39], J. van Tilburg[42],
V. Tisserand[4], M. Tobin[40], J. Todd[58], S. Tolk[43], L. Tomassetti[17,g], D. Tonelli[39],
S. Topp-Joergensen[56], N. Torr[56], E. Tournefier[4], S. Tourneur[40], K. Trabelsi[40], M. Traill[52],
M.T. Tran[40], M. Tresch[41], A. Trisovic[39], A. Tsaregorodtsev[6], P. Tsopelas[42], N. Tuning[42,39],
A. Ukleja[29], A. Ustyuzhanin[66,65], U. Uwer[12], C. Vacca[16,39,f], V. Vagnoni[15], G. Valenti[15],
A. Vallier[7], R. Vazquez Gomez[19], P. Vazquez Regueiro[38], C. Vázquez Sierra[38], S. Vecchi[17],
M. van Veghel[43], J.J. Velthuis[47], M. Veltri[18,h], G. Veneziano[40], M. Vesterinen[12], B. Viaud[7],
D. Vieira[2], M. Vieites Diaz[38], X. Vilasis-Cardona[37,p], V. Volkov[33], A. Vollhardt[41], D. Voong[47],
A. Vorobyev[31], V. Vorobyev[35], C. Voß[64], J.A. de Vries[42], R. Waldi[64], C. Wallace[49], R. Wallace[13],
J. Walsh[24], J. Wang[60], D.R. Ward[48], N.K. Watson[46], D. Websdale[54], A. Weiden[41],
M. Whitehead[39], J. Wicht[49], G. Wilkinson[56,39], M. Wilkinson[60], M. Williams[39], M.P. Williams[46],
M. Williams[57], T. Williams[46], F.F. Wilson[50], J. Wimberley[59], J. Wishahi[10], W. Wislicki[29],
M. Witek[27], G. Wormser[7], S.A. Wotton[48], K. Wraight[52], S. Wright[48], K. Wyllie[39], Y. Xie[62],
Z. Xu[40], Z. Yang[3], J. Yu[62], X. Yuan[35], O. Yushchenko[36], M. Zangoli[15], M. Zavertyaev[11,c],
L. Zhang[3], Y. Zhang[3], A. Zhelezov[12], A. Zhokhov[32], L. Zhong[3], V. Zhukov[9], S. Zucchelli[15]

1 *Centro Brasileiro de Pesquisas Físicas (CBPF), Rio de Janeiro, Brazil*
2 *Universidade Federal do Rio de Janeiro (UFRJ), Rio de Janeiro, Brazil*
3 *Center for High Energy Physics, Tsinghua University, Beijing, China*
4 *LAPP, Université Savoie Mont-Blanc, CNRS/IN2P3, Annecy-Le-Vieux, France*
5 *Clermont Université, Université Blaise Pascal, CNRS/IN2P3, LPC, Clermont-Ferrand, France*
6 *CPPM, Aix-Marseille Université, CNRS/IN2P3, Marseille, France*
7 *LAL, Université Paris-Sud, CNRS/IN2P3, Orsay, France*
8 *LPNHE, Université Pierre et Marie Curie, Université Paris Diderot, CNRS/IN2P3, Paris, France*
9 *I. Physikalisches Institut, RWTH Aachen University, Aachen, Germany*
10 *Fakultät Physik, Technische Universität Dortmund, Dortmund, Germany*
11 *Max-Planck-Institut für Kernphysik (MPIK), Heidelberg, Germany*
12 *Physikalisches Institut, Ruprecht-Karls-Universität Heidelberg, Heidelberg, Germany*
13 *School of Physics, University College Dublin, Dublin, Ireland*
14 *Sezione INFN di Bari, Bari, Italy*
15 *Sezione INFN di Bologna, Bologna, Italy*
16 *Sezione INFN di Cagliari, Cagliari, Italy*
17 *Sezione INFN di Ferrara, Ferrara, Italy*
18 *Sezione INFN di Firenze, Firenze, Italy*
19 *Laboratori Nazionali dell'INFN di Frascati, Frascati, Italy*
20 *Sezione INFN di Genova, Genova, Italy*
21 *Sezione INFN di Milano Bicocca, Milano, Italy*
22 *Sezione INFN di Milano, Milano, Italy*

[23] *Sezione INFN di Padova, Padova, Italy*

[24] *Sezione INFN di Pisa, Pisa, Italy*

[25] *Sezione INFN di Roma Tor Vergata, Roma, Italy*

[26] *Sezione INFN di Roma La Sapienza, Roma, Italy*

[27] *Henryk Niewodniczanski Institute of Nuclear Physics Polish Academy of Sciences, Kraków, Poland*

[28] *AGH - University of Science and Technology, Faculty of Physics and Applied Computer Science, Kraków, Poland*

[29] *National Center for Nuclear Research (NCBJ), Warsaw, Poland*

[30] *Horia Hulubei National Institute of Physics and Nuclear Engineering, Bucharest-Magurele, Romania*

[31] *Petersburg Nuclear Physics Institute (PNPI), Gatchina, Russia*

[32] *Institute of Theoretical and Experimental Physics (ITEP), Moscow, Russia*

[33] *Institute of Nuclear Physics, Moscow State University (SINP MSU), Moscow, Russia*

[34] *Institute for Nuclear Research of the Russian Academy of Sciences (INR RAN), Moscow, Russia*

[35] *Budker Institute of Nuclear Physics (SB RAS) and Novosibirsk State University, Novosibirsk, Russia*

[36] *Institute for High Energy Physics (IHEP), Protvino, Russia*

[37] *Universitat de Barcelona, Barcelona, Spain*

[38] *Universidad de Santiago de Compostela, Santiago de Compostela, Spain*

[39] *European Organization for Nuclear Research (CERN), Geneva, Switzerland*

[40] *Ecole Polytechnique Fédérale de Lausanne (EPFL), Lausanne, Switzerland*

[41] *Physik-Institut, Universität Zürich, Zürich, Switzerland*

[42] *Nikhef National Institute for Subatomic Physics, Amsterdam, The Netherlands*

[43] *Nikhef National Institute for Subatomic Physics and VU University Amsterdam, Amsterdam, The Netherlands*

[44] *NSC Kharkiv Institute of Physics and Technology (NSC KIPT), Kharkiv, Ukraine*

[45] *Institute for Nuclear Research of the National Academy of Sciences (KINR), Kyiv, Ukraine*

[46] *University of Birmingham, Birmingham, United Kingdom*

[47] *H.H. Wills Physics Laboratory, University of Bristol, Bristol, United Kingdom*

[48] *Cavendish Laboratory, University of Cambridge, Cambridge, United Kingdom*

[49] *Department of Physics, University of Warwick, Coventry, United Kingdom*

[50] *STFC Rutherford Appleton Laboratory, Didcot, United Kingdom*

[51] *School of Physics and Astronomy, University of Edinburgh, Edinburgh, United Kingdom*

[52] *School of Physics and Astronomy, University of Glasgow, Glasgow, United Kingdom*

[53] *Oliver Lodge Laboratory, University of Liverpool, Liverpool, United Kingdom*

[54] *Imperial College London, London, United Kingdom*

[55] *School of Physics and Astronomy, University of Manchester, Manchester, United Kingdom*

[56] *Department of Physics, University of Oxford, Oxford, United Kingdom*

[57] *Massachusetts Institute of Technology, Cambridge, MA, United States*

[58] *University of Cincinnati, Cincinnati, OH, United States*

[59] *University of Maryland, College Park, MD, United States*

[60] *Syracuse University, Syracuse, NY, United States*

[61] *Pontifícia Universidade Católica do Rio de Janeiro (PUC-Rio), Rio de Janeiro, Brazil, associated to [2]*

[62] *Institute of Particle Physics, Central China Normal University, Wuhan, Hubei, China, associated to [3]*

[63] *Departamento de Fisica , Universidad Nacional de Colombia, Bogota, Colombia, associated to [8]*

[64] *Institut für Physik, Universität Rostock, Rostock, Germany, associated to [12]*

[65] *National Research Centre Kurchatov Institute, Moscow, Russia, associated to [32]*

[66] *Yandex School of Data Analysis, Moscow, Russia, associated to [32]*

[67] *Instituto de Fisica Corpuscular (IFIC), Universitat de Valencia-CSIC, Valencia, Spain, associated to [37]*

[68] *Van Swinderen Institute, University of Groningen, Groningen, The Netherlands, associated to [42]*

[a] Universidade Federal do Triângulo Mineiro (UFTM), Uberaba-MG, Brazil
[b] Laboratoire Leprince-Ringuet, Palaiseau, France
[c] P.N. Lebedev Physical Institute, Russian Academy of Science (LPI RAS), Moscow, Russia
[d] Università di Bari, Bari, Italy
[e] Università di Bologna, Bologna, Italy
[f] Università di Cagliari, Cagliari, Italy
[g] Università di Ferrara, Ferrara, Italy
[h] Università di Urbino, Urbino, Italy
[i] Università di Modena e Reggio Emilia, Modena, Italy
[j] Università di Genova, Genova, Italy
[k] Università di Milano Bicocca, Milano, Italy
[l] Università di Roma Tor Vergata, Roma, Italy
[m] Università di Roma La Sapienza, Roma, Italy
[n] Università della Basilicata, Potenza, Italy
[o] AGH - University of Science and Technology, Faculty of Computer Science, Electronics and Telecommunications, Kraków, Poland
[p] LIFAELS, La Salle, Universitat Ramon Llull, Barcelona, Spain
[q] Hanoi University of Science, Hanoi, Viet Nam
[r] Università di Padova, Padova, Italy
[s] Università di Pisa, Pisa, Italy
[t] Scuola Normale Superiore, Pisa, Italy
[u] Università degli Studi di Milano, Milano, Italy

[†] Deceased